Experimental Study of Turbulent Flows Over Sharp-crested Spillways with a Circular Downstream Curvature Profile for Downstream Fish Migration

by

Ali Shirinzad

A Thesis submitted to the Faculty of Graduate Studies of

The University of Manitoba

In Partial Fulfilment of the Requirements of the Degree of

MASTER OF SCIENCE

Department of Mechanical Engineering

University of Manitoba

Winnipeg, Manitoba, Canada

Abstract

This thesis presents experimental investigations of the effects of water depth and upstream face inclination on the turbulence characteristics upstream and over spillways. Spillways are hydraulic structures that regulate the reservoir water level and the flow rate passing through the turbines. Recent studies have focused on using surface spill water as migratory pathways to provide a safe bypass for downstream migrants. Developing an effective passage system through spillways requires both biological knowledge of fish behavior and hydraulic knowledge of spillway flows to provide hydrodynamic conditions that fish may exploit. The goal of this study is to understand the effect of upstream face inclination and water depth on the hydrodynamic characteristics and find the most suitable conditions for the downstream passage of fish.

Particle image velocimetry (PIV) technique was used to conduct nine sets of experiments for a sharp-crested spillway of height $h = 0.15$ m with a circular downstream curvature profile. The examined upstream face inclinations included the 90° standard, 45° modified, and 30° modified angles. For each upstream face inclination, three water depths over the crest (D_c), including $D_c/h =$ 0.7, 0.4, and 0.2, were investigated to obtain various configurations of the test parameters. The Reynolds numbers based on the spillway height and oncoming velocity (Re_h) were $Re_h = 46200$, 24300, and 10350 for $D_c/h = 0.7$, 0.4, and 0.2, respectively.

The results showed a distinct recirculation zone at the heel of the 90° standard spillway at the lowest water depth ($D_c/h = 0.2$) and a secondary recirculation bubble near the crest for all test cases. It was concluded that the upstream recirculation bubble may be suppressed by either increasing the water depth or decreasing the upstream face inclination. Decreasing the upstream face inclination generated a more uniform acceleration and decreased the turbulence levels, which may increase the passage efficiency. Overall, the environment generated by the modified spillways suggested a safer and more appealing hydraulic condition for the downstream migrants. Over the spillway, the flow near the free surface was in rigid-body motion, while the angular momentum varied linearly in the stream-wise direction at a far enough distance from the recirculation zone.

Co-authorship Statement

In this thesis, I designed and performed all the experiments, analyzed and interpreted the data and wrote the manuscript. Mr. Sedem Kumahor provided valuable assistance in the course of data acquisition. My academic advisor, Prof. Mark Francis Tachie, who is the second author for this thesis, provided valuable feedback and helped me in the interpretation of the data and evaluation of the manuscript.

.....	.....
Ali Shirinzad	Dr. Mark Tachie
M.Sc. Student and First Author	Academic Advisor and Second Author

Acknowledgments

First, I would like to express my sincere gratitude to my academic advisor, Dr. Mark Francis Tachie for his immense teachings, valuable guidance, patience, foresight and encouragements, which immensely contributed to my achievements during my M.Sc. program. I am indeed grateful for the opportunities he provided for me to present my research work at international conferences across the world and publish these results in a high-impact journal.

Thank you to Mr. Sedem Kumahor, Dr. Xingjun Fang, Mr. Ali Sagharichi, and all my colleagues within the research group for their valuable inputs, guidance, and support throughout my program. I would also like to acknowledge the essential technological support provided by Mr. Brendan Pachal and the valuable knowledge and safety training from Mr. Paul Krueger.

I would like to express my special gratitude towards Mr. Christos Katopodis from Katopodis Ecohydraulics Ltd. and Dr. Haitham Ghamry from the Department of Fisheries and Oceans Canada for their contributions and invaluable feedback on the biological aspects of the research.

I am also grateful to the Department of Fisheries and Oceans Canada, University of Manitoba Faculty of Graduate Studies and the Department of Mechanical Engineering, and Canada Foundation for Innovation for all forms of financial supports during this program.

Table of Contents

List of Tables

List of Figures

1. Introduction

1.1. Background and Motivation

On a worldwide scale, human activities such as overfishing, pollution, and a proliferation of dams and other hydraulic structures have caused the population of several fish species to decline significantly. The increasing need for electric power has been a crucial part of socioeconomic advancement in many countries, resulting in the construction of numerous dams, weirs, and other hydroelectric facilities on rivers. The migration corridors in regulated rivers lead the migrating fish towards hydroelectric facilities, blocking the migratory pathways, isolating the fish populations, causing high mortality risk to fish migrants, and even eliminating some aquatic species (Zhong and Power, 1996; Katopodis and Aadland, 2006; García et al., 2011). Worldwide, concerns about the upstream migration of fish, that is, migration ascending a river towards high grounds, has always been nearly immediate since if dams were constructed without provision for fish passage, no harvest above the obstructions could occur (Katopodis and Williams, 2012).

At the beginning of the 20th century, issues with the conservation of high-value adult salmon prompted extensive research on upstream migration, with significant advancements made in the development of fishways for the successful passage of several salmonids (Katopodis, 1992; Larinier and Travade, 2002; Williams et al., 2012). Baffle, pool-and-weir, and vertical-slot fishways are examples of upstream passage systems, shown in Figure 1.1. The first systematic baffle fishway was developed by Denil (1909, 1938) in Belgium, whose efforts were characterized by trial and error approaches with careful and extensive empirical observations. Denil fishways have been studied in detail through physical hydraulic modeling, where comprehensive analyses were conducted on discharge, water depth, velocity distributions, and turbulence (Larinier, 1992; Katopodis, 1992; Katopodis et al., 1997). Pool-and-weir fishways consist of a series of pools of regular length that are constructed in the form of steps, divided by overflow weirs. This fish passage type is most suited for strong swimmers, such as adult Atlantic salmon (*Salmo salar*), brown trout (*Salmo trutta*), and Arctic charr (*Salvelinus alpinus*). Fish passage over pool-and-weir fishways is affected by hydraulic

characteristics in pools as well as by changes in the flow regime from plunging to streaming over weirs as discharge rate increases. Hydraulic studies of pool and weir fishways were carried out to investigate how slope, discharge rate, weir height, and spacing affect flow regimes over the weirs, circulation patterns in the pools, and other relevant hydraulic characteristics such as the discharge rate and velocity distributions (Katopodis, 2005; Silva et al., 2011, 2012a). Vertical slot fishways operate similarly to pool-and-weir fish ladders, with the difference that they allow the fish to swim at their preferred depth. Extensive hydraulic studies of different designs with single slots, most of which were summarized by Katopodis (1992), have contributed to adjusting this fishway type to meet the needs of a variety of fish species (Katopodis and Williams, 2012).

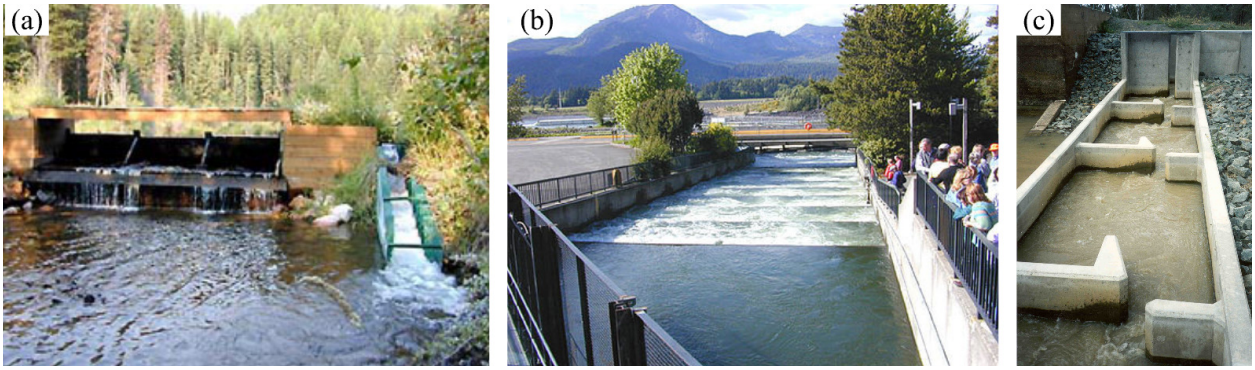

Figure 1.1. Examples of upstream passage systems: (a) Denil fishway, (b) Pool-and-weir fishway (https://thereaderwiki.com/en/Fish_ladder), and (c) vertical slot fishway (https://theconstructor.org/water-resources/types-fish-ladders-fishways/).

Downstream migration, that is, migration descending a river towards seas or lakes, while understood as equally important by fishery community, was initially ignored since fishery on downstream migrants seldom occurred. In addition, in most cases, the downstream migrants were small, and their mortality rate was not high enough to perceptively decrease adult returns. For instance, the population of downstream migrants for most salmonids consists mostly of smolts which suffer lower mortality rates in contrast to adults that are especially vulnerable when passing through hydro-turbines (Katopodis and Williams, 2012). As a result, facilities to secure the downstream migration for post-spawners and their progeny are far less advanced and less efficient compared to their upstream counterparts. The few measures that exist have almost exclusively targeted

anadromous species, and more particularly salmonids, (Ferguson et al., 1998; Scruton et al., 2003; Ferguson et al., 2007; Larinier, 2008). For many other fish species, including iteroparous fish that undertake multiple annual migrations, catadromous fish that spawn in salt water, cyprinids, esocides, and percides, the downstream passage facilities often fail to meet the expectations of fishery agencies. Research on downstream passage technologies is ongoing with a sense of urgency, covering various subjects, including aquaculture, ecology, biochemistry, physiology, swimming capacity and behavior, fish passage, and even dam removal, to restore the connectivity of aquatic habitats and possibly reverse the worldwide decline in the population of fish species (Katopodis and Aadland, 2006; Wilkes et al., 2018).

Most of the existing downstream fish passage facilities fall under one of the following categories: behavioral devices, screening systems, spillways and bypass channels. An example of each of these passage systems is provided in Figure 1.2.

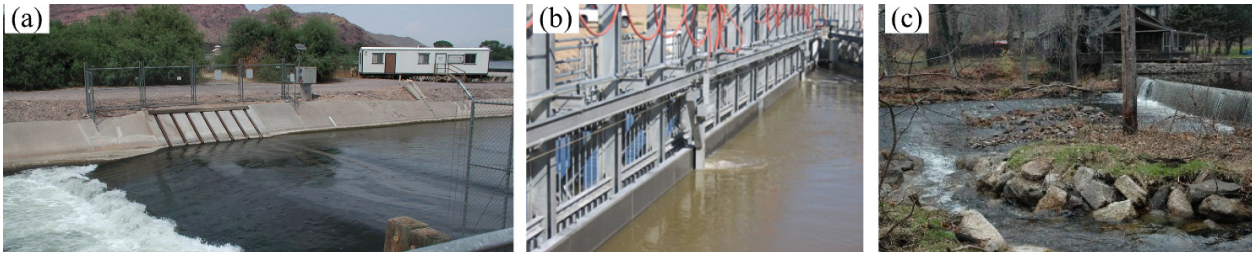

Figure 1.2. Examples of downstream passage facilities: (a) electrical barrier (https://www.usbr.gov/lc/phoenix/biology/azfish/), (b) fish screens (https://en.wikipedia.org/wiki/Fish_screen), and (c) bypass channel (https://sites.google.com/a/onefishengineering.com/2013version/passage-types/other-fish-passage-structures).

Behavioral devices trigger the natural response of fish to specific stimuli to alter the migratory routes. Extensive research has been conducted on behavioral devices based on visual (Brett and MacKinnon, 1953; Fields, 1957; Brett and Alderdice, 1958), auditory (Burner and Moore, 1953; Sonny et al., 2006), hydrodynamic (Bates and Vinsonhaler, 1957; Bates and Jewett Jr, 1961; Ruggles and Ryan, 1964; Vanderwalker, 1970), and electrical (Monan et al., 1967; Pugh et al., 1970) stimuli both in laboratories and on test sites. Behavioral devices are convenient for users and designers alike since they can be afforded at low enough costs, require minimum protection

against clogging, and need minimal maintenance. Although promising results have been achieved for several species, such as salmonids, clupeids, and even eels (Hadderingh et al., 1992), under controlled conditions, the reliability of behavioral devices is highly dependent on the configuration of the site and species. Furthermore, the repeated stimulation of fish to certain triggers may cause a reduction in response and fish habituation (Coutant and Whitney, 2000; Coutant, 2001). Behavioral devices should be used with caution since manufacturers of these devices often tend to promote the use of their products and may overrate their efficiency (Larinier and Travade, 2002).

Fish screens constitute meshes with such small openings that prevent large fish from passing through turbine intakes. The excluded fish are then transported downstream either directly through bypass systems or manually after being captured in fish collection facilities. Fish screens come in various forms, including wire mesh, wedge wire, perforated plate, ogee weir-shaped, and bar racks with various modifications (Amaral, 2003; Tsikata et al., 2009a,b; Katopodis et al., 2011; Calles et al., 2013; Albayrak et al., 2020). The oncoming velocity towards screens must be adjusted to match the swimming capacity of fish and prevent impingement. Screening systems must be regularly inspected for any accumulation of debris that may cause clogging and compromise their efficiency. In recent years, screening systems have become affordable for small dams and irrigation canals, where it is possible to use higher oncoming velocities to reduce the filtration area and decrease the total cost of the system. For large-scale dams, on the other hand, due to relatively large screen areas and water intake footprints, as well as maintenance and cleaning issues, screens are usually dropped in favor of surface bypasses or spillways (Katopodis and Williams, 2012).

Using spillways and other surface bypass systems is an alternative method for providing a safe passage for downstream migrating fish. Spillways are hydraulic structures that release the surplus water into the downstream riverbed when the reservoir is full, typically during flooding seasons, or when kinetic turbines reach their maximum capacity. Spillways are constructed in various forms depending on their application and site configurations. Figure 1.3 showcases the Ogee, chute, and bell-mouth (morning glory) spillways, respectively.

Figure 1.3. Examples of spillways: (a) Ogee, (b) chute , and (c) bell-mouth (morning glory) spillways (https://energyeducation.ca/encyclopedia/Spillway).

Spillways may provide a safe bypass for the downstream migrants provided that they are designed properly. Understanding the flow characteristics associated with spillways is essential for improving both their design and their suitability for downstream passage of diverse fish species. Although much is understood about the mean flow and its influence on downstream fish migrants, studies on other important flow characteristics, such as the spatial accelerations, Reynolds shear stress, and turbulent kinetic energy (TKE), and their relation with fish behavior, swimming capacity, and survival rate are more limited.

A proper framework is required to establish the relationship between hydraulic conditions and the swimming capacity of fish species. Castro-Santos et al. (2009) argued that seven research questions must be answered to thoroughly correlate relevant biological, hydraulic, and physical parameters in the passage performance of fish. One of the proposed questions was '*How does turbulence structure influence swimming performance?*', emphasizing that developing effective passage systems through spillways not only requires biological knowledge of fish behavior but also hydraulic knowledge of a variety of turbulent characteristics to provide suitable hydraulic conditions for the downstream fish migrants.

Lacey et al. (2012) characterized the hydraulic variables into four classes, namely intensity, periodicity, orientation, and scale (IPOS). For instance, TKE, vorticity, and Reynolds stresses are all classified under intensity. Energy spectra and axis orientation of eddies fall into periodicity and orientation, respectively, while eddy length scale, diameter, and Reynolds number are classified

under scale. Cote and Webb (2015) argued that turbulent eddies are the major flow variable that affects the swimming capacity of fish and used turbulent intensity, diameter of eddies, vorticity, momentum of fish, and persistence of eddies to characterize the behavioral response of fish to varying hydraulic conditions. Duguay et al. (2018) presented a metric consisting of a combination of length-scale and eddy strength to evaluate effects on fish stability in recirculatory eddies, which is based on the angular frequency of the eddy and the average tangential velocity of eddy perimeter. Needless to say that the quantification of all of the hydraulic variables under the IPOS classification requires time-resolved whole-field measurement techniques that provide both spatial and temporal data.

1.2. Objectives

The goal of this study is to undertake a comprehensive experimental investigation of turbulent flows over spillways of different geometries and at different rates of discharge using particle image velocimetry (PIV) technique. The main objectives are achieved through the following sub-objectives:

1. Experimentally investigate the effects of upstream face inclination and water depth on the hydraulic conditions upstream and over the crest of spillways and relate the pertinent characteristics to the downstream passage of fish.
2. Provide a repository of benchmark data for development and validation of computational fluid dynamics models.

The rationale for using PIV is to take full advantage of its time-resolved whole-field measurement capability to perform detailed analysis of hydraulic variables relevant to the downstream migration of fish. The results and analysis provided in this thesis will provide useful insight into the hydraulics over spillways and also serve as an essential benchmark for the further development and validation of computational fluid dynamics models.

1.3. Thesis Outline

The remainder of this thesis is organized as follows: A comprehensive literature review is presented in chapter 2. The experimental set-up and measurement procedures are described in Chapter 3. Chapter 4 focuses on the main results and discussion. A summary of the major findings and conclusions are presented in Chapter 5. Finally, supplementary one-dimensional profiles are provided in the appendix.

2. Literature Review

Direct passage through hydro-turbines exposes fish to various forms of stress, such as impacts from turbine blades, abrupt variations in acceleration or pressure, and cavitation, resulting in high mortalities (Čada, 2001; Brown et al., 2014). For salmonids and American shad (*Alosa sapidissima*), mortality rates often range from 5 % to 90 % in Francis turbines (Larinier and Travade, 2002). Eels are especially susceptible to turbine mortality because of their elongated bodies (Montén, 1985) and their thigmotactic behavior, resulting in close contact with hydraulic structures (Richkus and Dixon, 2002; DWA, 2005). The reported mortality rates for turbines are relatively high, ranging from 15 %-30 % in large hydro-turbines to even 50 %-100 % in the smaller turbines used in small-scale hydroelectric dams (Montén, 1985; Hadderingh and Bakker, 1998). For example, adult American eels (*Anguilla rostrata*) encounter two consecutive hydro-power stations on the St. Lawrence River, namely Moses-Saunders and Beauharnois, where turbine mortality rates of 26.4 % and 17.8 % were reported, respectively (Verreault and Dumont, 2003). In the case of the American eel or the New Zealand longfin eel (*Anguilla dieffenbachii*), some experts have recommended a complete shutdown of hydro-turbines during the downstream migration period (Euston et al., 1998; Mitchell, 1995). For the European eel (*Anguilla anguilla*), it is often not feasible to stop the operation of hydro-turbines during the downstream migration periods due to the unpredictable or lengthy characteristics of this activity, which may result in power capacity shortage.

Passage through spillways may directly cause mortalities due to shearing effects, abrasion against spillway surfaces, collisions with concrete baffles and aprons, and abrupt changes in pressure, or indirectly by increasing the susceptibility of disorientated or stunned fish to predation and disease (Larinier and Travade, 2002). Although the reported mortality rates due to direct passage through spillways are typically low (Larinier and Travade, 2002; Schwevers and Adam, 2020), higher values ranging between 8 % to 37 % have occasionally been recorded as well (Bell and DeLacy, 1972; Ruggles, 1980; Ruggles and Murray, 1983). For spillways, safeguarding the downstream migrants is rarely an issue, and they are often regarded as the safest method for fish to pass hydroelectric

dams. Even when spillways are not the primary passage system, they are still relevant to downstream migration since some species, such as the European eel, tend to migrate during flooding seasons when spillways are regularly operated to maintain the stored water in the reservoir at a safe level (Calles et al., 2013).

Surface water release over spillways, albeit with sometimes a high cost of energy foregone, has been shown to be very effective in guiding the downstream migrants away from hydro-turbines and decreasing the forebay residence time (Johnson and Dauble, 2006; Ferguson et al., 2005). Arnekleiv et al. (2007) investigated the autumn and spring descent of brown trout at the Hunderfossen dam, south-east Norway, using radiotelemetry. It was observed that not only neither kelts nor smolts entered the turbine pathway, but the majority of both smolts and kelts migrated downstream shortly after surface water release over the spillways. Kelts used surface water released over the spillways as their primary migratory pathway, further emphasizing the importance of the surface water routes.

Previous studies on spillways have revealed that the hydraulic environment induced by spillways is strongly influenced by a deviation from the spillway design head, such as a change in water depth above the crest, or the specific geometry of the spillway (Savage and Johnson, 2001; United States Army Corps of Engineers (USACE), 1988; United States Bureau of Reclamation, 1987). Consequently, variations in water depth over the crest or modifications to the upstream face inclination may affect both the swimming ability of fish, that is, their ability to maintain posture and control function while safely migrating downstream, and their behavioral responses, which vary among species and individuals (Williams et al., 2012; Verbiest et al., 2012).

In their study on the downstream migration of the brown trout, Arnekleiv et al. (2007) observed that 0 %, 39 %, 62 %, 80 %, and 100 % of the descending kelts passed through the ice spillway during 1 m^3/s, 4 m^3/s, 6 m^3/s, 15 m^3/s, and 25 m^3/s rates of discharge, respectively. The threshold value for the descent of kelts over the ice spillway was estimated to be between 1 m^3/s and 4 m^3/s, which corresponded to a water column between 12 cm and 36 cm. In a similar study by Travade et al. (2010) on the downstream migration of the European eel at a hydropower plant on the Gave de Pau

river in South-West France using radio and passive integrated transponder (PIT) telemetry between 2004 and 2007, it was reported that 44 % and 74 % of the tested eels used the spillways during low and high river discharges, respectively. The corresponding approach velocities at the turbine intakes were 0.20 m/s and 0.44 m/s, whereas the values at the spillway and bypass entrances were 0.50 m/s and 1.00 m/s, respectively. Both the observations of Arnekleiv et al. (2007) and Travade et al. (2010) shows that the depth of the water column over the spillway, which determines the total discharge rate, has a strong effect on the passage efficiency of spillways.

Previously studied geometrical differences mostly include modifications to the upstream face inclination of spillways. Haro et al. (1998) performed laboratory experiments on two surface weir designs in an enclosed flume supplied with river water from a hydropower canal near the Connecticut River at Turners Falls, Massachusetts, to investigate the behavior and passage rate of Atlantic salmon smolts and juvenile American shad. It was observed that 74.3 % and 89.7 % of the Atlantic salmon smolts passed the standard sharp-crested and modified NU-Alden weirs after 180 min, respectively. Under the same test conditions, the successful passage rate reduced to 29.6 % and 40.1 % when the experiments were repeated for the American shad. Haro et al. (1998) remarked that the American shad showed strong avoidance to the imposed hydraulic conditions and low motivation to swim downstream. The lower passage rates for the American shad indicate that different species respond differently to identical hydraulic conditions.

Silva et al. (2015) performed live fish experiments in an open-channel prototype at National Laboratory for Civil Engineering (LENC), Portugal, to study the downstream movement behavior of the European eel and Iberian barbel (*Luciobarbus bocagei*) over spillways with different upstream face inclinations. Three PVC-made spillways with upstream face angles of 90°, 45°, and 30° were tested for two water depths, 0.32 m and 0.42 m, to examine the effects of both water depth and upstream face inclination. It is important to note that the fish experiments were performed for individual fish, and confounding schooling effects were averted. Silva et al. (2015) also performed acoustic Doppler velocimetry (ADV) to measure the approach velocities, and particle

image velocimetry (PIV) to further investigate the mean velocity fields and the mean streamlines. The ADV measurements were conducted upstream of the standard spillway prototype of height 0.25 m used in their live fish experiments, while the PIV measurements were conducted on a 1:5 scale model at the University of Manitoba, Canada. For all test conditions, Froude number similarity was maintained between the model and the prototype. For the European eel, the recorded successful passage per approach for the water depth of 0.42 m were 75 %, 95 %, and 92 % for the 90° standard, 45° modified, and 30° modified spillways, respectively. Meanwhile, the corresponding values for the Iberian barbel were significantly lower at 36 %, 33 %, and 37 %. Although there were species-related differences, Silva et al. (2015) concluded that the modified spillways may improve the downstream migration of fish. The 30° modified spillway was apparently the most effective, particularly for the European eel, due to the lowest passage times and comparatively high rates of successful passage. It is interesting to note that at the water depth of 0.32 m, only 58 % of European eels and 21 % of Iberian barbels passed over the 90° standard spillway, which again implies the importance of water depth and its concomitant effects on the swimming ability and response of fish. In addition, although the ADV measurements were conducted for high Reynolds number, for the PIV measurements, the Reynolds numbers were quite lower, and consequently, upscaling the PIV measurements for relatively high spillway prototypes may not be feasible.

Katopodis and Gervais (2016) provided a comprehensive review on the swimming ability of several fish species to different hydraulic conditions, emphasizing that fish behaviors and migratory pathways are affected by several hydraulic variables that should be considered altogether. Recent studies have revealed that different hydraulic variables, including turbulent kinetic energy (TKE), Reynolds shear stress, vorticity, and acceleration, have different effects on fish movement trajectories, rheotaxis, posture stability, ability to rest or hold station, and propulsion (Tritico and Cotel, 2010; Silva et al., 2012b; Cote and Webb, 2015; Duguay et al., 2018; Amaral et al., 2019; Li et al., 2021).

3. Experimental Set-up and Methodology

3.1. Test section

The experiments were performed in an open recirculating water channel located in the Turbulence and Hydraulic Engineering Laboratory (THEL) at the University of Manitoba. Figure 3.1 demonstrates the main components of the facility, including the flow conditioning unit, test section, variable frequency drive, return pipe, and the turning vane system.

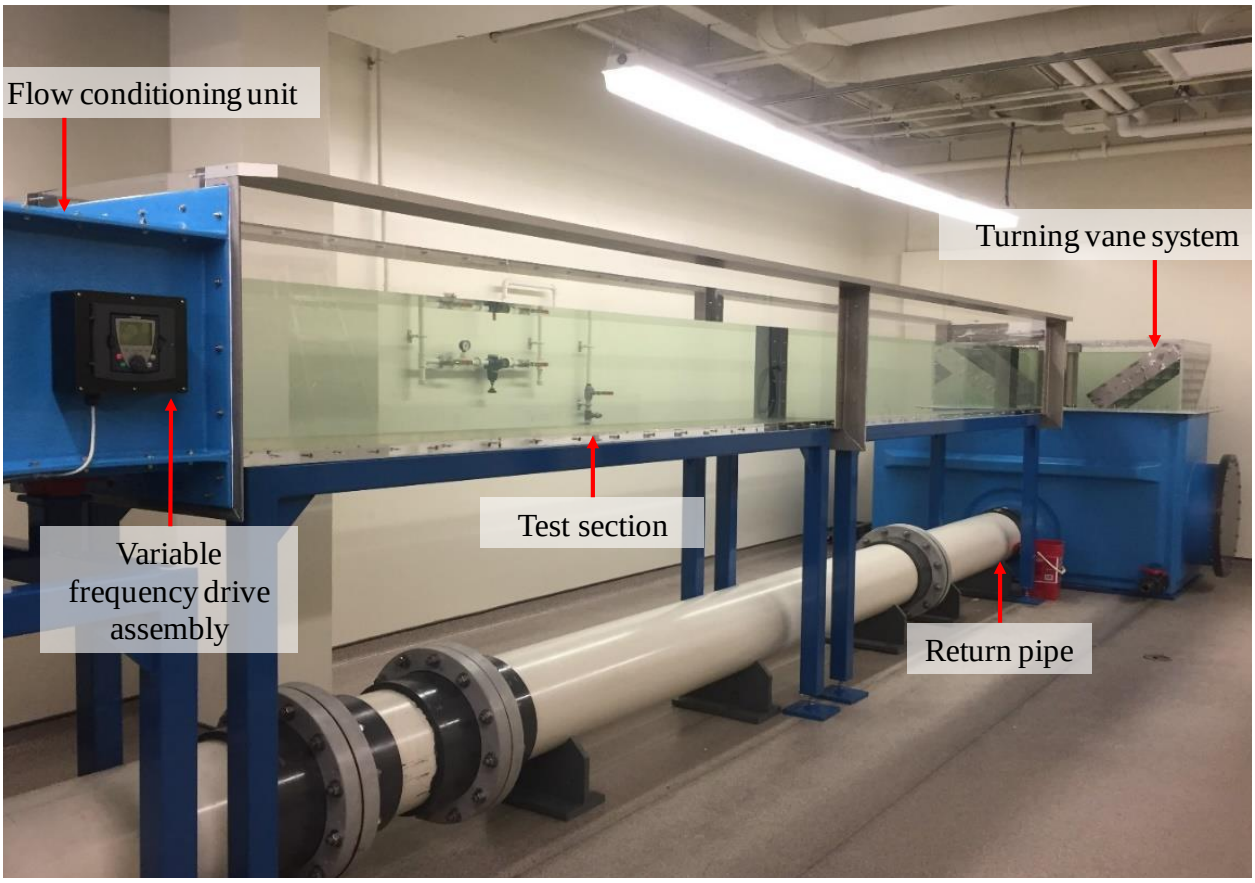

Figure 3.1. A picture of the open recirculating water channel in the Turbulence and Hydraulics Engineering Laboratory.

The stream-wise length, span-wise width, and depth of the channel are 6.00 m, 0.60 m, and 0.45 m, respectively. The bottom and sidewalls of the test section are fabricated from 31.8 mm thick Super transparent Abrasion-Resistant® acrylic plates to promote optical access from all sides of the test section.

The flow in the channel is driven by a 30 kW variable-speed drive motor capable of producing a maximum flow rate of 33 950 L/min. The speed of the pump is regulated using the variable frequency drive to change the oncoming velocity from 0.1 m/s to 2.0 m/s. Upstream of the test section, a series of flow conditioning units consisting of a perforated plate, a hexagonal honeycomb, mesh screens of different sizes, and a 4.88:1 converging section are employed to homogenize the flow and reduce the turbulence prior to the test section. The water exiting the test section enters a turning vane system, which guides the flow to the return pipe under the channel bottom for recirculation of water.

3.2. Test models and test conditions

Figure 3.2 shows the spillway models and the adopted nomenclature in the present study. The upstream water depth and water depth over the crest of the spillways are denoted by D_o and D_c, respectively. The oncoming free-stream velocity is denoted by U_e and the maximum velocity over the spillway crest is denoted by U_c. A Cartesian coordinate system is adopted with the origins of the stream-wise (x) and vertical (y) axes set at the upstream leading edge and foot of the 90° standard spillway, respectively. The spillway model was sharp-crested with a downstream curvature profile that followed a circle with a radius of $r_c = 0.16$ m, starting at $\alpha_c = 20.64°$, as shown in Figure 3.2(b). A polar-cylindrical coordinate system is also adopted with its origin is at the center of the curvature, to characterize the flow over the spillway, as shown in Figure 3.2(b). It is more common to examine certain flow characteristics, such as the mean velocities or higher order moments of statistics, with respect to the distance from the walls, which requires the curvilinear coordinate system $n - s$, as illustrated in Figure 3.2(b). The $n - s$ coordinate system is related to $r - \alpha$ coordinate system through the following relations:

$$n = r - r_c \tag{3.1}$$

$$s = r_c \left(\pi \frac{\alpha - \alpha_c}{180}\right) \tag{3.2}$$

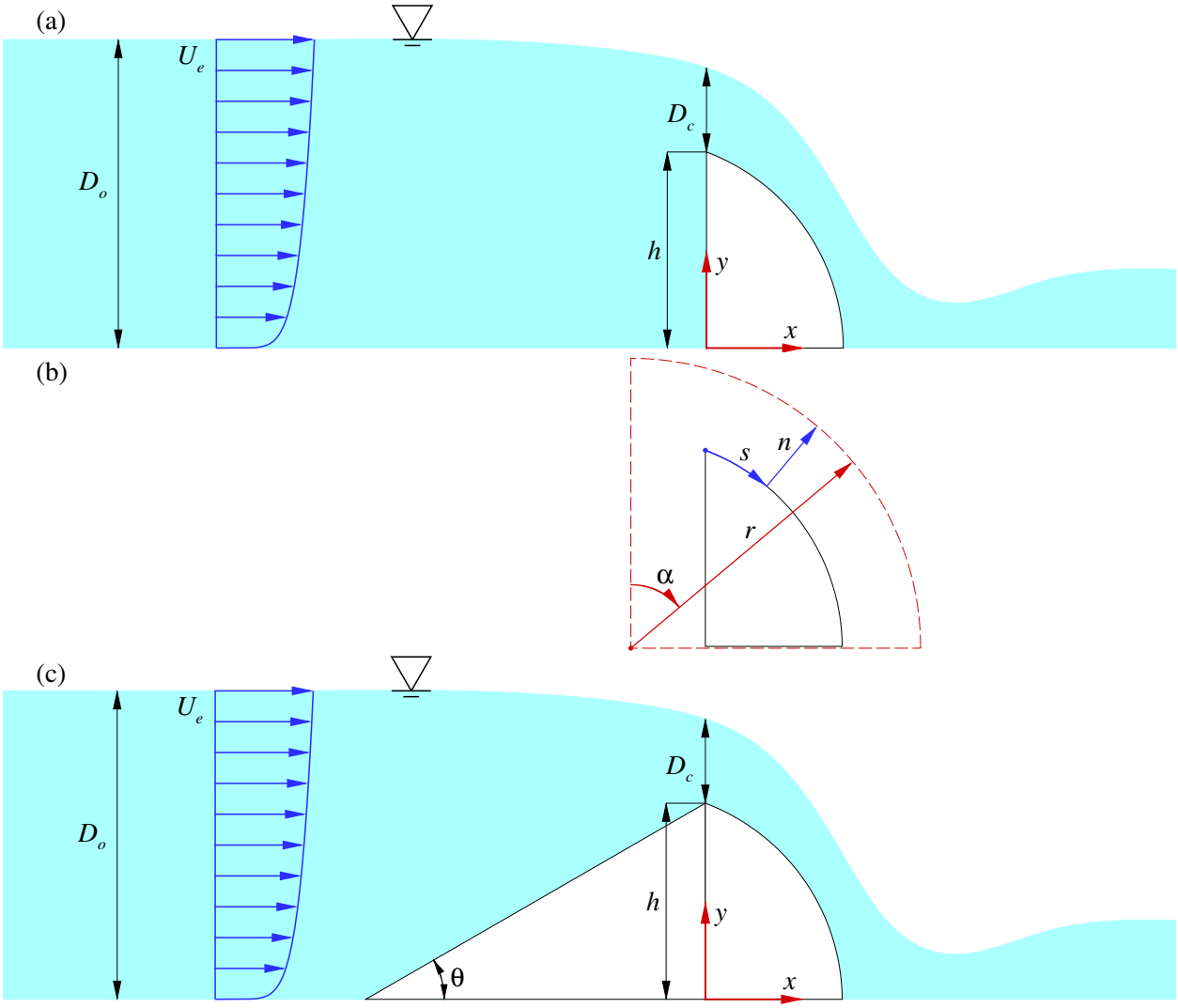

Figure 3.2. Schematic drawings showing (a) the 90° standard spillway and the adopted nomenclature, (b) downstream curvature profile, and (c) the modified spillways and the adopted nomenclature.

The test models consisted of a 90° standard spillway as well as two spillway models with modified upstream face inclination of 45° and 30°. The 90° standard spillway was installed at 2.50 m downstream of the entrance to the test section. The upstream face inclination was modified by installing the 45° and 30° wedges immediately upstream of the 90° standard spillway, as shown in Figure 3.3. The spillway models were fabricated from smooth acrylic plates in the Machine Shop at Price Faculty of Engineering, University of Manitoba. The height and span-wise width of all spillway models were kept constant at $h = 0.15$ m and $L = 0.60$ m, respectively.

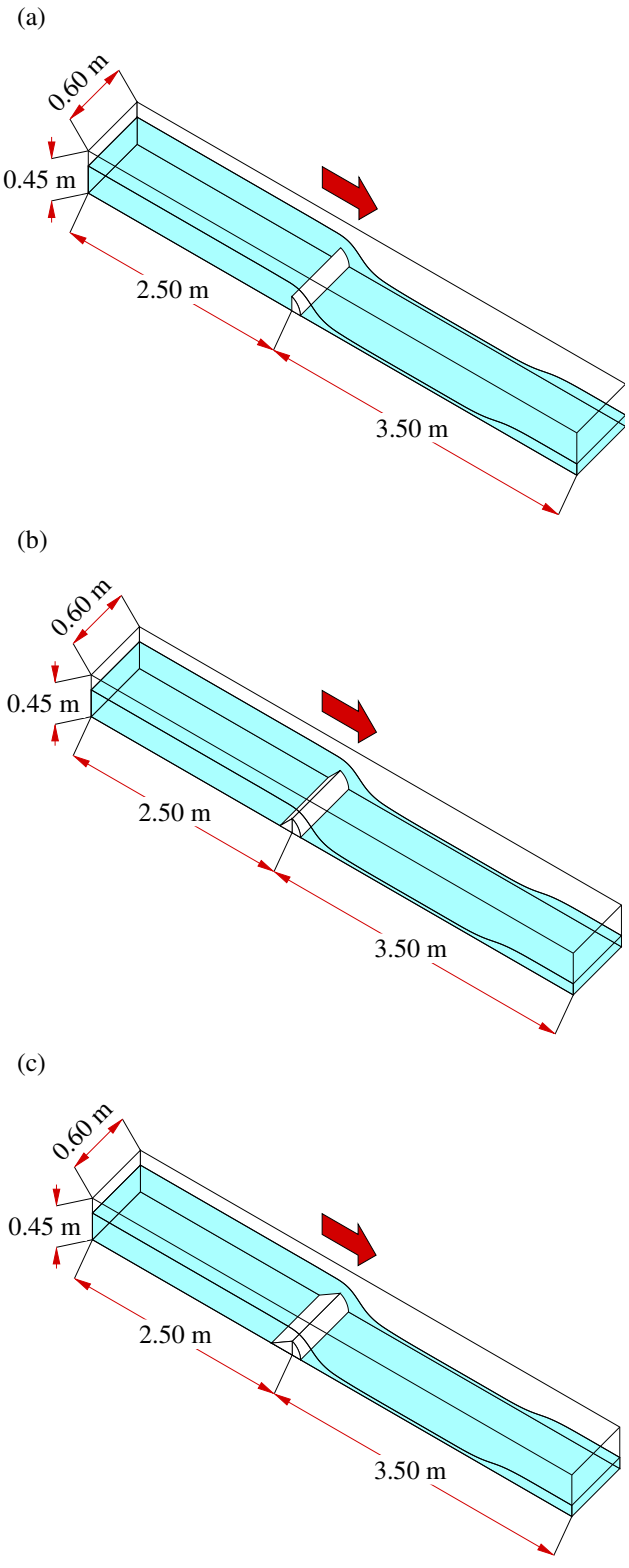

Figure 3.3. Schematic drawing of the test section in birds-eye view: (a) 90° standard, (b) 45° modified, and (c) 30° modified spillways.

The water depth over the crest at the steady-state condition depends on the initial water depth, the net flow rate discharged by the impeller pump, and the upstream face inclination of the spillway. The water depth over the crest was adjusted to the desired values by keeping the oncoming velocity constant while monitoring the water level and draining the surplus water from the channel. Three water depths over the crest, including $D_c/h = 0.7$, 0.4, and 0.2, were investigated for each spillway design to obtain various configurations of test parameters. The room temperature was regulated at 20 °C, and hence, the kinematic viscosity of water used as the working fluid was $\nu = 1.0\times10^{-6}$ m^2/s. Table 3.1 provides a summary of the water depths, Reynolds number based on free-stream velocity and spillway height, $Re = U_e h/\nu$, Froude number based on upstream water depth and spillway height, $Fr_o = U_e/\sqrt{gD_o}$ where $g = 9.81$ m/s^2 is the acceleration due to gravity, and Froude number based on water depth at the crest and maximum velocity at the crest, $Fr_c = U_e/\sqrt{gD_c}$.

Table 3.1. Summary of the test parameters.

θ	D_o/h	D_c/h	U_e (m/s)	U_c (m/s)	$Re = U_e h/\nu$	$Fr_o = U_e/\sqrt{gD_o}$	$Fr_c = U_c/\sqrt{gD_c}$
	1.63	0.70	0.308	1.476	46200	0.199	1.453
90°	1.40	0.45	0.162	1.175	24300	0.113	1.444
	1.20	0.25	0.069	0.755	10350	0.052	1.225
	1.68	0.71	0.308	1.488	46200	0.196	1.456
45°	1.42	0.42	0.162	1.179	24300	0.112	1.500
	1.21	0.20	0.069	0.761	10350	0.052	1.403
	1.68	0.67	0.308	1.457	46200	0.196	1.467
30°	1.46	0.43	0.162	1.239	24300	0.111	1.558
	1.22	0.21	0.069	0.756	10350	0.051	1.360

All of the examined Reynolds numbers are large enough to establish turbulent flow conditions. It is important to note that when the Reynolds number is high enough, the measurements may

be upscaled for a prototype using Froude number similarity (Finnemore and Franzini, 2002). Meanwhile, for all test cases, Fr_o is less than one, whereas Fr_c was greater than one, implying sub-critical and super-critical flow, respectively.

3.3. PIV system and measurement procedure

A planar particle image velocimetry system was used to perform velocity measurements at the mid-span of the channel. The main components of the PIV system are illustrated in Figure 3.4. The flow was seeded with 10 µm silver coated hollow glass spheres of specific gravity 1.4. In the operation of PIV, the fluid velocities are calculated from the motion of the seeding particles, and consequently, the ability of the particles to faithfully follow the fluid motions must be carefully examined.

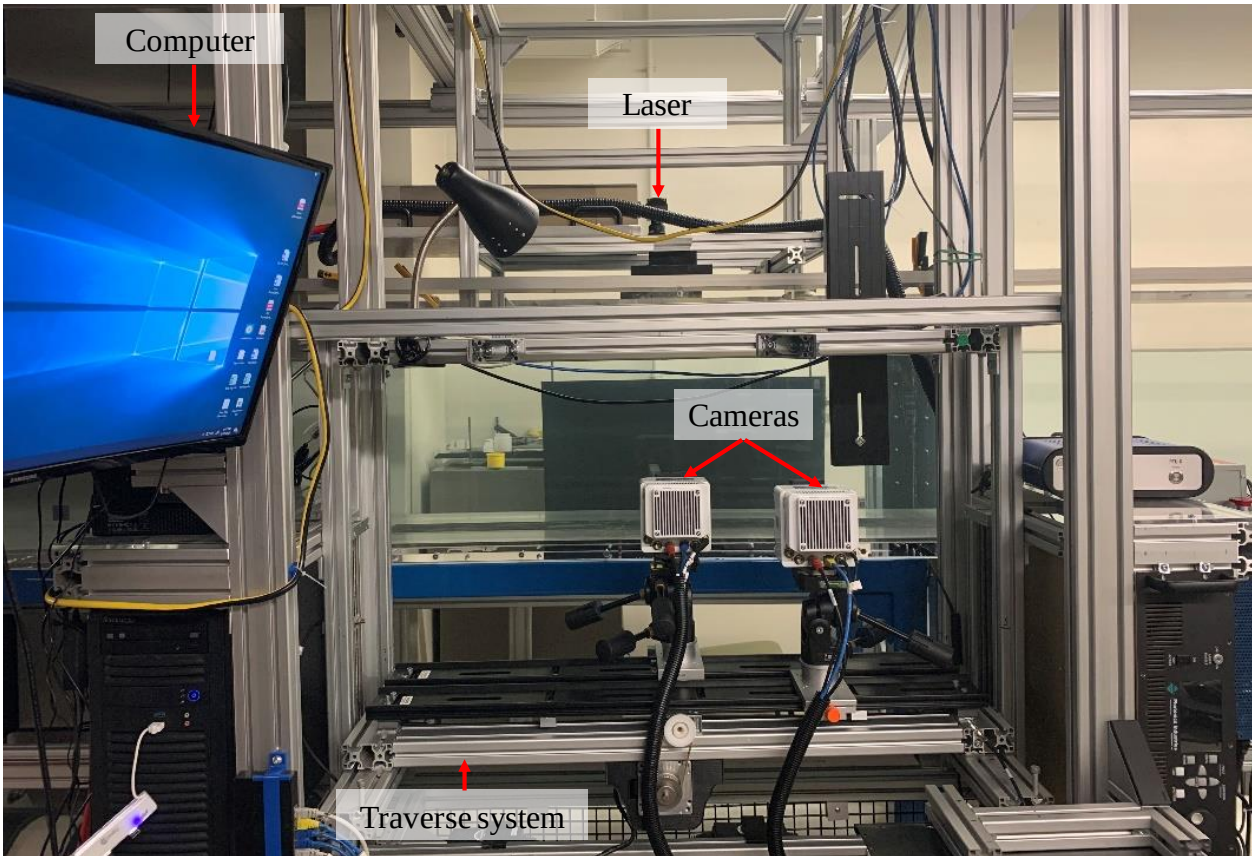

Figure 3.4. Various components of the PIV system.

The slip velocity, u_s, which is the difference between the local velocities of the fluid and seeding

particles, was estimated using the following equation:

$$u_s = \frac{d_p^2(\rho_p - \rho_f)g}{18\rho_f \nu} \tag{3.3}$$

In equation (3.3), d_p is the diameter of the seeding particles, ρ_p and ρ_f represent the densities of the seeding particles and water, respectively. The slip velocity was 2.18×10^{-5} m/s, which is four orders of magnitude lower than the free-stream velocities. Therefore, the particle velocities are assumed to accurately represent the local fluid velocity. To characterize the response of the seeding particles to sudden changes in the flow motions, the relaxation time, $\tau_p = u_s/g$, was estimated to be 2.22×10^{-6} s. The temporal Taylor micro-scale of the highest Reynolds number flow, τ_f, evaluated for the 90° spillway experiment at the location of the maximum of the stream-wise Reynolds stress, was $\tau_f = 0.049$ s. The Stokes number, $S_k = \tau_p/\tau_f$, which is a measure of the particle response time relative to the characteristic time scale of the small eddies is of the order of 4.53×10^{-5}. This value is four orders of magnitude smaller than the threshold value of 0.05 recommended by Samimy and Lele (1991) for which seeding particles are assumed to faithfully follow flow motions.

The seeding particles were illuminated by a diode-pumped dual-cavity high-speed Neodymium-doped yttrium lithium fluoride (Nd:YLF) laser with maximum pulse energy of 30 mJ/pulse for each laser and a wavelength of 527 nm at an operation frequency of 1000 Hz. The laser light sheet thickness was approximately 1.5 mm. Two high-speed 12-bit complementary metal-oxide-semiconductor cameras of resolution 2560 pixels × 1600 pixels positioned side-by-side, were used to simultaneously capture the light scattered by the illuminated seeding particles within the fields of view shown in Figure 3.5. Both cameras were fitted with a Nikon 60 mm lens and were calibrated such that the fields of views overlapped by 10 mm in the stream-wise direction. The sampling frequency was set to 3 Hz, and a total number of 12000 images were captured in double-frame mode, resulting in a total sampling time of 2000 seconds. The high-speed mode was used to acquire 96000 images at a sampling frequency of 800 Hz. These time-resolved datasets are necessary for the analysis of the periodicity and temporal characteristics of the turbulence motions.

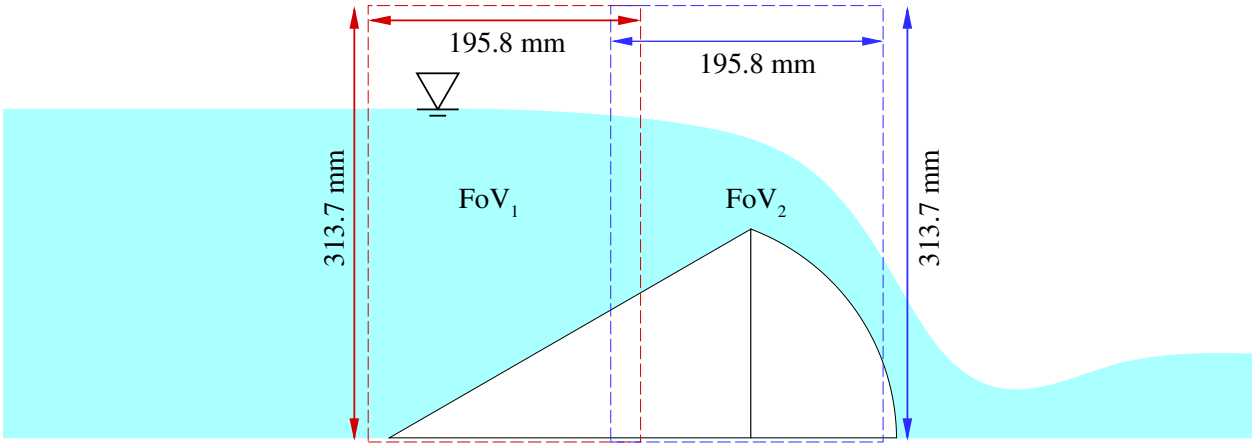

Figure 3.5. A schematic showing the fields of views (FoVs) used in the present study.

The data acquisition and vector processing were controlled using commercial software DaVis® (version 10.0.5) supplied by LaVision. A GPU-accelerated multi-pass cross-correlation algorithm was used to calculate the velocity vectors, using an interrogation area of 64 pixels × 64 pixels with 50 % overlap and four final passes used an IA of 16 pixels × 16 pixels with 75 % overlap as the four final passes. The resulting vector spacing was 0.48 mm ($0.0032h$).

3.4. Measurement uncertainty

Following Sciacchitano and Wieneke (2016) and Bendat and Piersol (2011), the expressions used to quantify the measurement uncertainty for statistically independent samples are summarized in equations (3.4) and (3.5).

$$\xi_{U_i} = \frac{Z_c}{U_i}\sqrt{\frac{\overline{u_i'u_i'}}{N}} \tag{3.4}$$

$$\xi_{\overline{u_i'u_j'}} = \begin{cases} Z_c\sqrt{\frac{1}{N}\left(\frac{\overline{u_i'u_i'u_i'u_i'}}{\overline{u_i'u_i'}\,\overline{u_i'u_i'}} - 1\right)} & i = j \\ Z_c\sqrt{\frac{1+\varphi^2_{u_i'u_j'}}{N-1}} & i \neq j \end{cases} \tag{3.5}$$

In equations (3.4) and (3.5), ξ_{U_i}, $\xi_{\overline{u_i'u_j'}}$, and Z_c represent the uncertainty in the mean velocities, Reynolds stresses, and the confidence coefficient, respectively, while $\varphi_{u_i'u_j'}$ is the cross-correlation

coefficient and is given by the following equation:

$$\varphi_{u_i'u_j'} = \frac{\overline{u_i'u_j'}}{\sqrt{\overline{u_i'u_i'}}\sqrt{\overline{u_j'u_j'}}} \tag{3.6}$$

To quantify the measurement uncertainty within 95 % confidence level, $Z_c = 1.96$ is used and the results are summarized in Table 3.2 for the various turbulence statistics at the location of local maximum of the stream-wise Reynolds stress, $(x_0/h, y_0/h)$, near the crest.

Table 3.2. Summary of the uncertainty quantification values for 12000 double-frame samples at the specified points in each experiment.

θ	D_c/h	x_0/h	y_0/h	ξ_U	ξ_V	$\xi_{\overline{u'u'}}$	$\xi_{\overline{v'v'}}$	$\xi_{\overline{u'v'}}$
	0.7	0.1699	1.0124	0.8274	2.0978	2.9787	2.8652	1.8291
90°	0.4	0.0803	1.0116	0.8163	2.8717	1.8210	2.6985	1.8118
	0.2	0.0738	0.9974	1.3986	2.7270	2.1328	2.8049	1.9086
	0.7	0.1609	1.0232	1.6877	1.2523	2.2392	2.8069	1.7911
45°	0.4	0.1219	0.9992	0.6156	1.2007	2.1542	2.6125	1.8766
	0.2	0.0963	0.9921	0.8844	1.2342	2.0950	2.8061	1.8484
	0.7	0.1591	1.0111	2.0764	1.1712	2.4159	2.9858	1.7893
30°	0.4	0.1094	0.9969	0.6295	1.0694	2.1350	2.6422	1.8863
	0.2	0.1057	0.9755	1.0956	1.0392	2.2707	2.7389	1.8065

Finally, we remark that the acquired data immediately near the free surface may not reflect the actual flow conditions since, as was observed in the experiments, the particles in this region do not scatter the light properly. Nevertheless, this region is not removed from the contours, and consequently, readers may see unreasonable flow characteristics in this region.

4. Results and Discussion

Throughout this section, comprehensive analyses are performed to investigate the effects of the upstream face inclination and water depths on both mean and turbulence statistics. Data post-processing, analysis, and visualization were accomplished using commercial software Matlab®, Tecplot 360 EX®, and Origin®. All plots are normalized using the oncoming velocity, U_e, and the height of the spillway model, h.

4.1. Mean velocities and streamlines

4.1.1. Mean velocities

Figure 4.1 shows the contours of the normalized mean stream-wise velocity, U/U_e. As the flow approaches the spillway, the mean stream-wise velocity increases significantly due to the reduction in flow cross-sectional area. Evidently, as the upstream water depth decreases, the magnitudes of the normalized mean stream-wise velocities over the spillway increase. Negative regions of mean stream-wise velocity are observed near the heel of the 90° standard spillway as can be seen from Figures 4.1(a), 4.1(b), and 4.1(c). Hence, it can be concluded that the approach flow separates from the channel floor due to severe adverse pressure gradient upstream of the 90° standard spillway. For each test case, the onset of the separation is estimated using the isopleth of $U/U_e = 0$ shown on each plot. Flow separation occurs at $x/h = -0.6$, -0.6, and -1.5 for $D_c/h = 0.7$, 0.4, and 0.2, respectively. The maximum backflows were $0.12U_e$, $0.11U_e$, for $D_c/h = 0.7$ and $D_c/h = 0.4$ test cases, while the corresponding value for $D_c/h = 0.2$ test case was $0.46U_e$. Clearly, both the separation point and the maximum backflow are strongly affected by the upstream water depth. The immediate consequence of decreasing the upstream face inclination is the suppression of the separation upstream of the spillway due to the induced favorable pressure gradient.

For the 90° standard spillway, contour levels are concentrated around the crest, indicating abrupt variations in the mean stream-wise velocity, which might trigger escape and avoidance responses. On the other hand, the mean stream-wise velocity varies more gradually for the modified spillways,

providing a more suitable hydraulic environment for the downstream migration of fish.

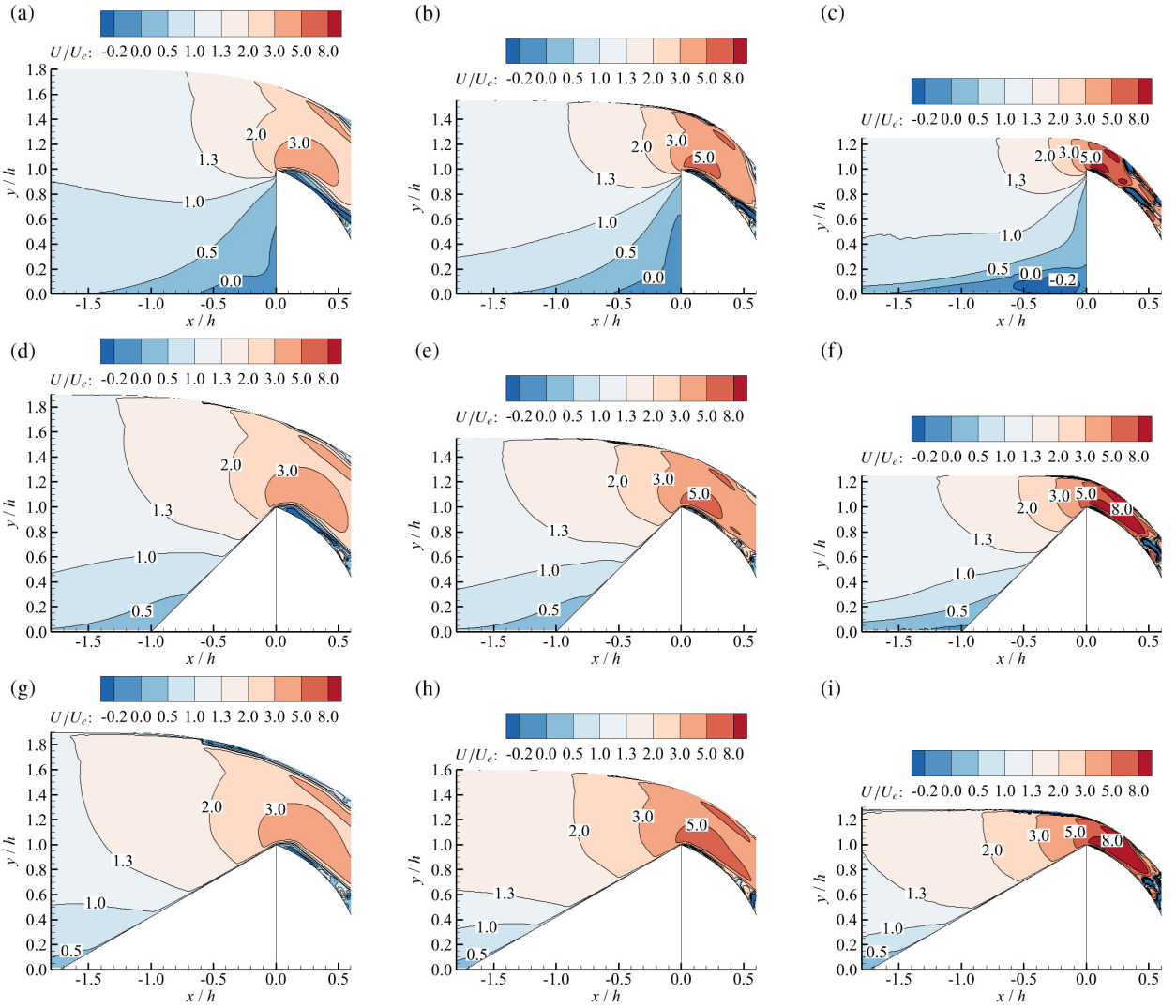

Figure 4.1. Contour plots of the normalized mean stream-wise velocity: (a) $\theta = 90°$, $D_c/h = 0.7$; (b) $\theta = 90°$, $D_c/h = 0.4$; (c) $\theta = 90°$, $D_c/h = 0.2$; (d) $\theta = 45°$, $D_c/h = 0.7$; (e) $\theta = 45°$, $D_c/h = 0.4$; (f) $\theta = 45°$, $D_c/h = 0.2$; (g) $\theta = 30°$, $D_c/h = 0.7$; (h) $\theta = 30°$, $D_c/h = 0.4$; (i) $\theta = 30°$, $D_c/h = 0.2$.

Contours of the normalized mean vertical velocity, V/U_e, are presented in Figure 4.2. For all test cases, regions of highly positive mean vertical velocity are observed around the crest, which is attributed to the upward deflection of the flow by the upstream face of the spillway. When the flow passes over the spillway, it is deflected downwards by gravity, causing the mean vertical velocity to change signs from positive to negative values.

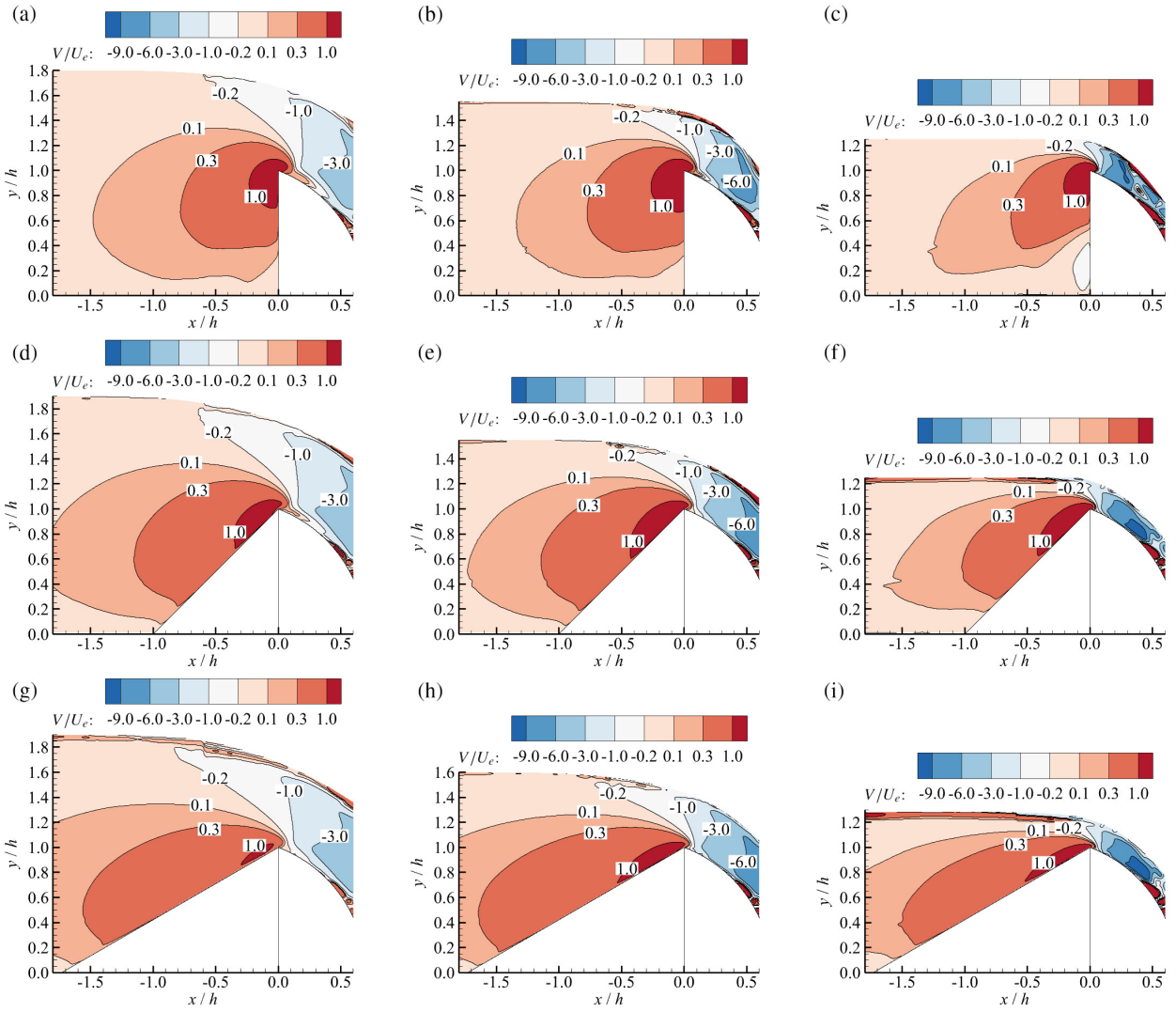

Figure 4.2. Contour plots of the normalized mean vertical velocity: (a) $\theta = 90°$, $D_c/h = 0.7$; (b) $\theta = 90°$, $D_c/h = 0.4$; (c) $\theta = 90°$, $D_c/h = 0.2$; (d) $\theta = 45°$, $D_c/h = 0.7$; (e) $\theta = 45°$, $D_c/h = 0.4$; (f) $\theta = 45°$, $D_c/h = 0.2$; (g) $\theta = 30°$, $D_c/h = 0.7$; (h) $\theta = 30°$, $D_c/h = 0.4$; (i) $\theta = 30°$, $D_c/h = 0.2$.

Evidently, the magnitudes of the normalized mean vertical velocities over the spillway increase as the water depth decreases. The effect of the upstream face inclination, on the other hand, is not straightforward. In the vicinity of the crest, the magnitude of the upward deflection decreases as the upstream face inclination decreases, resulting in lower mean vertical velocities for $\theta = 90°$, $45°$, and $30°$, respectively. Meanwhile, decreasing the upstream face inclination pushes the onset of the deflection farther upstream to $x/h = -\cot(\theta)$. Hence, as the upstream face inclination decreases,

the mean vertical velocity decreases in the vicinity of the spillway crest and increases near the heel of the spillway. The upstream hydraulic conditions of the modified spillways are more appropriate for the downstream migration of fish since, for the 90° standard spillway, the sudden variations in the mean velocities near the spillway can trigger escape and avoidance responses while also increasing the risk of injury and mortality rate.

4.1.2. Velocity magnitude

Contours of the normalized mean velocity magnitude, $\sqrt{U^2 + V^2}/U_e$, are provided in Figure 4.3. The velocity magnitude may be used for evaluating whether passage over the spillway would result in high mortality rates. When a fish falls over a spillway, it reaches a terminal velocity that is related to its length. Under free-fall conditions, this terminal velocity is about 12 m/s after a 25-30 m fall, 15-16 m/s after a 30-40 m fall, and more than 58 m/s after a fall of more than 200 m, for fish length of 10 to 13 cm, 15 to 18 cm, and 60 cm, respectively (Larinier and Travade, 2002). Experiments have revealed that when the impact velocity on the water surface exceeds 16 m/s, significant injuries, such as damage to the gills, eyes, and internal organs, occur regardless of the fish length (Bell and DeLacy, 1972).

Fish may also pass over the spillway while contained in the column of water. A column of water reaches the critical velocity of 16 m/s after a drop of 13 m. For heights greater than this, the risk of injury and mortality increases rapidly in proportion to the falling height. It is noteworthy to mention that passage through spillways under free-fall condition is less dangerous for small fish under 15-18 cm in length since they never reach a terminal velocity more than the critical velocity. For larger fish, on the other hand, the hazards are identical whether they pass under free-fall conditions or whether they are contained in the column of water (Larinier and Travade, 2002).

Using the Froude number similarity, the present test cases may be used to scale the velocity magnitudes according to the spillway height and water depth to assess whether the maximum velocity exceeds the critical velocity.

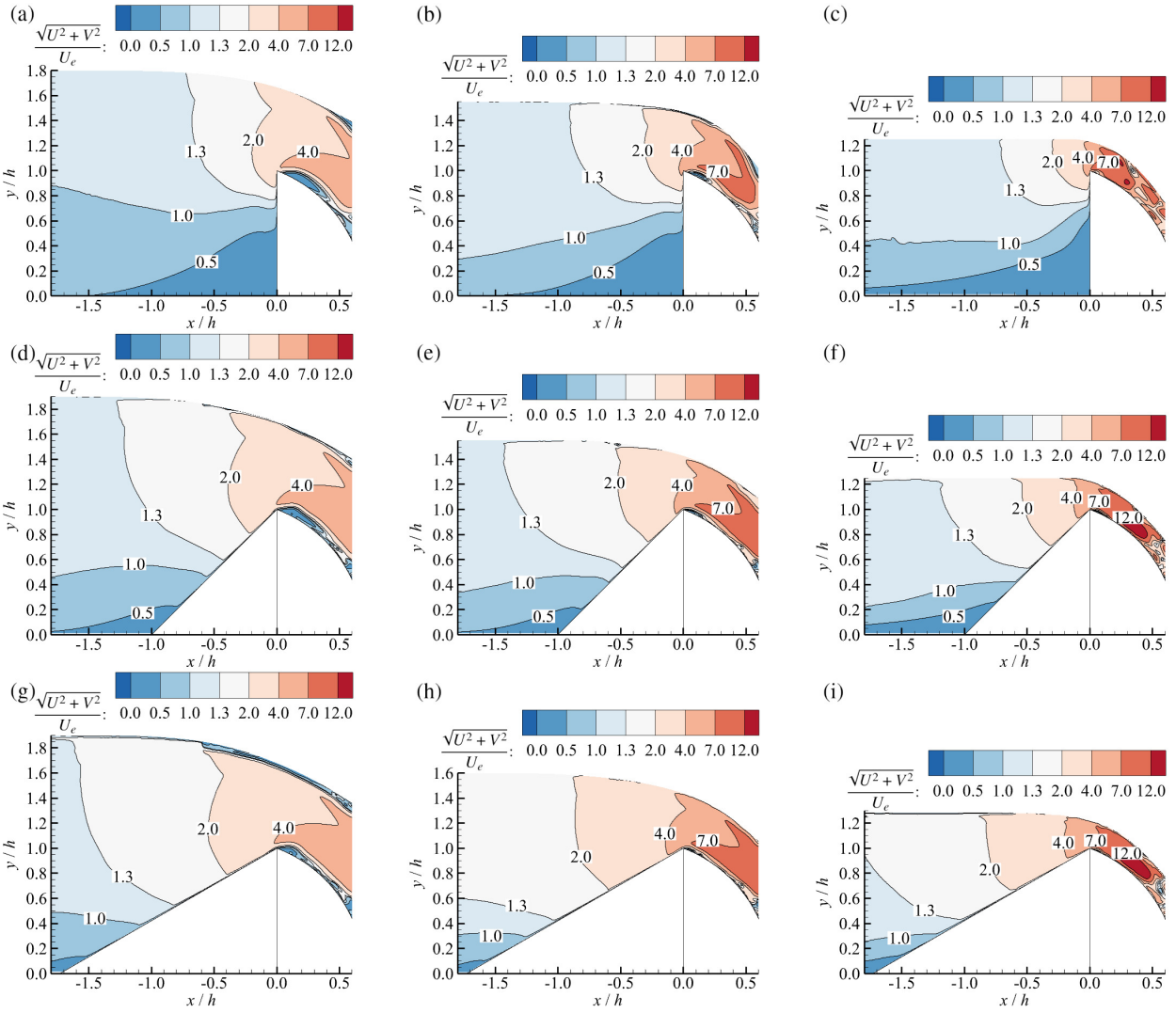

Figure 4.3. Contour plots of the normalized mean velocity magnitude: (a) $\theta = 90°$, $D_c/h = 0.7$; (b) $\theta = 90°$, $D_c/h = 0.4$; (c) $\theta = 90°$, $D_c/h = 0.2$; (d) $\theta = 45°$, $D_c/h = 0.7$; (e) $\theta = 45°$, $D_c/h = 0.4$; (f) $\theta = 45°$, $D_c/h = 0.2$; (g) $\theta = 30°$, $D_c/h = 0.7$; (h) $\theta = 30°$, $D_c/h = 0.4$; (i) $\theta = 30°$, $D_c/h = 0.2$.

For instance, assuming that a 90° standard spillway prototype of height 10.00 m is supposed to work at a water depth of $D_c/h = 0.2$, from Table 3.1 and Figure 4.3(b), the oncoming velocity and the maximum velocity over the spillway are obtained as follows:

$$\frac{{U_{e,p}}^2}{10.00} = \frac{U_e^2}{h} = \frac{0.069^2}{0.15} \Rightarrow U_{e,p} = 0.563\,\text{m/s}$$

$$\sqrt{U^2+V^2}_{max,p} \approx 12.0 \times 0.563 = 6.760\,\text{m/s}$$

Since $\sqrt{U^2 + V^2}_{max,p} < 12\,\mathrm{m/s}$, the hydraulic environment is safe for the passage of fish.

4.1.3. Mean streamlines

The plots of the mean streamlines are illustrated in Figure 4.4. A distinct recirculation bubble is observed near the heel of the 90° standard spillway at the water depth of $D_c/h = 0.2$, whose center is positioned at $(-0.286h, 0.200h)$. For all test cases, a secondary recirculation bubble is seen above the crest, attributed to the separation and reattachment of the flow, whose size decreases as the water depth decreases to the extent that it is negligibly small for $D_c/h = 0.2$ test cases.

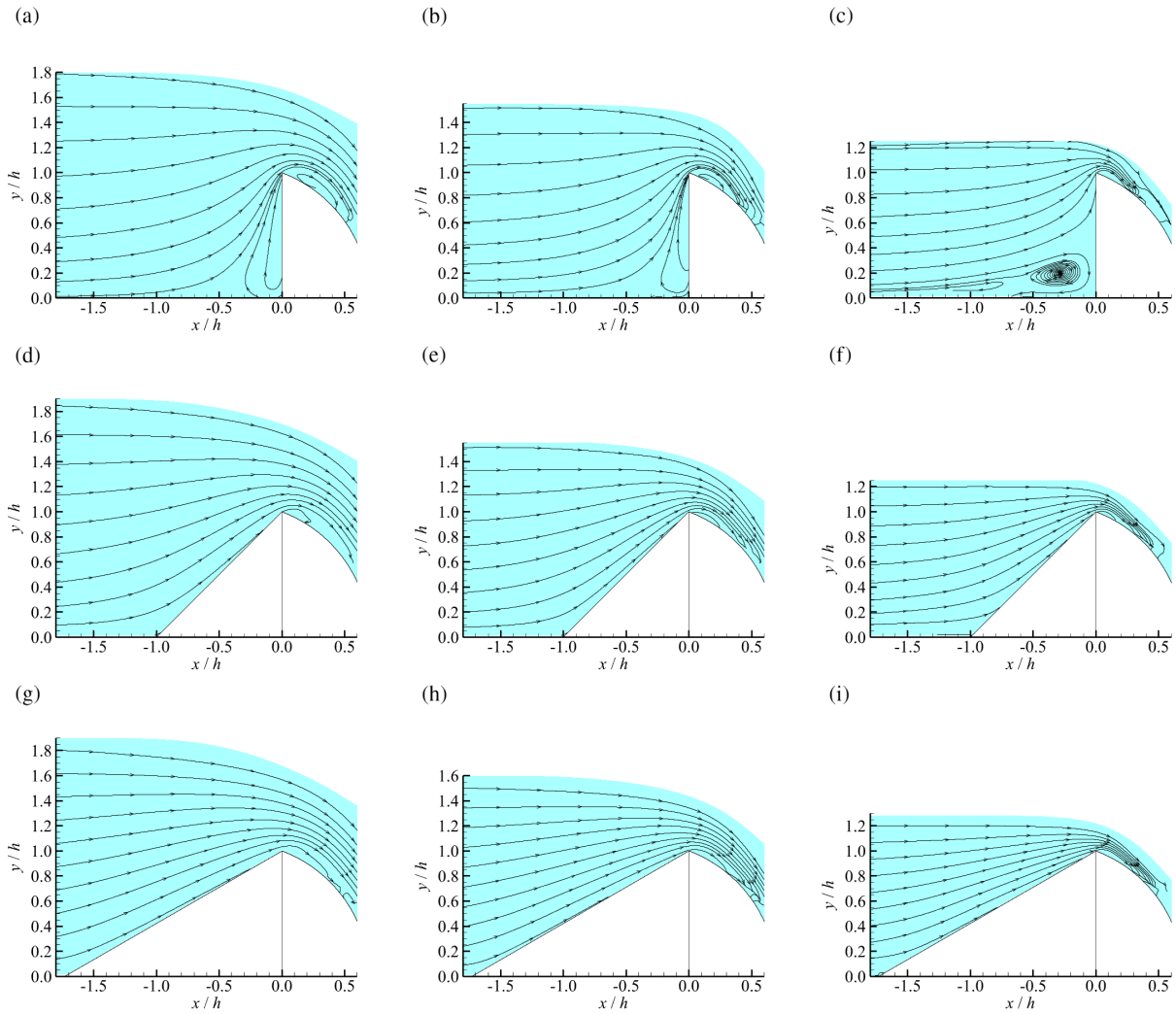

Figure 4.4. Plots of the mean streamlines: (a) $\theta = 90°$, $D_c/h = 0.7$; (b) $\theta = 90°$, $D_c/h = 0.4$; (c) $\theta = 90°$, $D_c/h = 0.2$; (d) $\theta = 45°$, $D_c/h = 0.7$; (e) $\theta = 45°$, $D_c/h = 0.4$; (f) $\theta = 45°$, $D_c/h = 0.2$; (g) $\theta = 30°$, $D_c/h = 0.7$; (h) $\theta = 30°$, $D_c/h = 0.4$; (i) $\theta = 30°$, $D_c/h = 0.2$.

Small fish often have difficulty passing through large recirculation bubbles and may even be trapped for long periods. Hence, recirculation bubbles immediately upstream of spillways should be avoided or at least minimized since they may compromise the downstream passage efficiency (Tarrade et al., 2008). From Figures 4.4(a), 4.4(b), and 4.4(c), it is clear that the upstream recirculation bubble at the heel of the 90° standard spillway may be avoided by increasing the water depth. Alternatively, decreasing the upstream face inclination generates a favorable pressure gradient, completely suppressing the flow separation and the recirculation zone, as evident from Figures 4.4(c), 4.4(f), and 4.4(i).

The streamlines are mostly parallel before reaching the spillway, where they converge over the crest and face pronounced curvature. From Figures 4.4(a), 4.4(b), and 4.4(c) it can be seen that the streamlines approach the upstream face of the 90° standard spillway head on, increasing the risk of impingement and possible mortality. Decreasing the upstream face inclination decreases the normal velocities and consequently the risk of impingement while also providing a tactile surface upstream of the spillway, which improves the downstream migration of thigmotactic species, such as eels (Silva et al., 2015).

4.2. Mean span-wise vorticity and acceleration

4.2.1. Mean span-wise vorticity

Figure 4.5 shows the contours of the normalized mean span-wise vorticity, $\Omega_z = (\partial V/\partial x - \partial U/\partial y) \times h/U_e$. For all test cases, the flow upstream of the spillway is irrotational except in the vicinity of the walls, where small negative values of vorticity are observed. Over the spillway, the sudden change in sign of the mean vertical velocity is responsible for larger values of the span-wise vorticity near the crest of the spillway.

The effects of vortices on fish depend on eddy characteristics, including intensity, periodicity, orientation, and size (Lacey et al., 2012), as well as different species and sizes. The values of the mean span-wise vorticity may be upscaled using Froude number similarity to predict the strength of vortices.

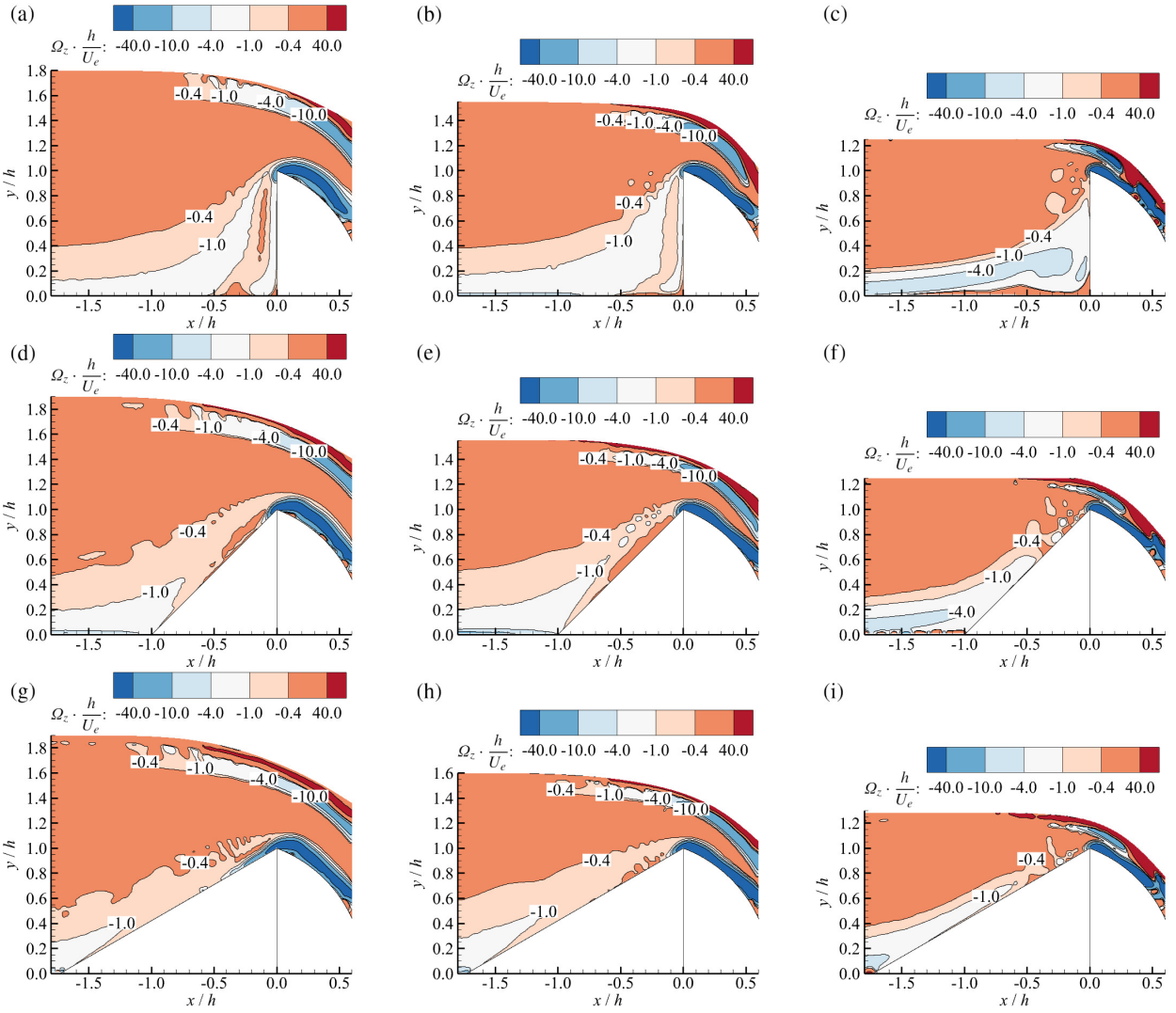

Figure 4.5. Contour plots of the normalized mean span-wise vorticity: (a) $\theta = 90°$, $D_c/h = 0.7$; (b) $\theta = 90°$, $D_c/h = 0.4$; (c) $\theta = 90°$, $D_c/h = 0.2$; (d) $\theta = 45°$, $D_c/h = 0.7$; (e) $\theta = 45°$, $D_c/h = 0.4$; (f) $\theta = 45°$, $D_c/h = 0.2$; (g) $\theta = 30°$, $D_c/h = 0.7$; (h) $\theta = 30°$, $D_c/h = 0.4$; (i) $\theta = 30°$, $D_c/h = 0.2$.

4.2.2. Mean acceleration

Contours of the normalized mean stream-wise acceleration, $\partial U/\partial x \times h/U_e$, are presented in Figure 4.6. For all test cases, negative values are observed near the heel of the spillway, indicating that the approaching flow is decelerated. The magnitude of the mean stream-wise acceleration upstream of the spillway increases as the upstream face inclination decreases due to the induced favorable pressure gradient.

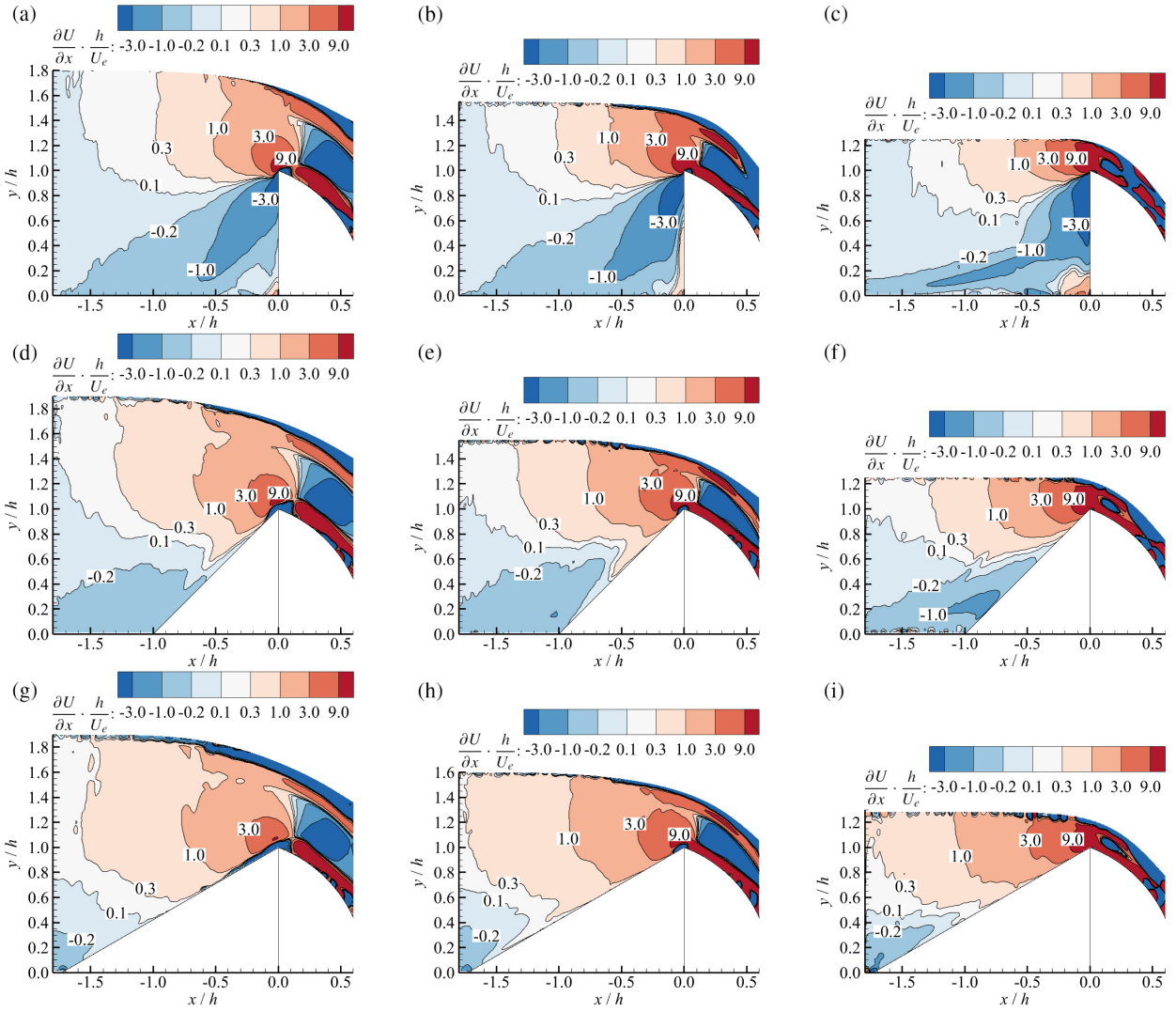

Figure 4.6. Contour plots of the normalized mean stream-wise acceleration: (a) $\theta = 90°$, $D_c/h = 0.7$; (b) $\theta = 90°$, $D_c/h = 0.4$; (c) $\theta = 90°$, $D_c/h = 0.2$; (d) $\theta = 45°$, $D_c/h = 0.7$; (e) $\theta = 45°$, $D_c/h = 0.4$; (f) $\theta = 45°$, $D_c/h = 0.2$; (g) $\theta = 30°$, $D_c/h = 0.7$; (h) $\theta = 30°$, $D_c/h = 0.4$; (i) $\theta = 30°$, $D_c/h = 0.2$.

Figure 4.7 shows the contours of the normalized mean vertical acceleration, $\partial V/\partial x \times h/U_e$. The flow continually undergoes positive acceleration before reaching the crest, where acceleration changes signs to negative values due to the gravitational forces. The mean vertical acceleration varies abruptly, especially around the crest, for the 90° standard spillway. For the 45° and 30° modified spillways, on the other hand, the variations of the mean vertical acceleration are more moderate, particularly along the upstream face of the spillway.

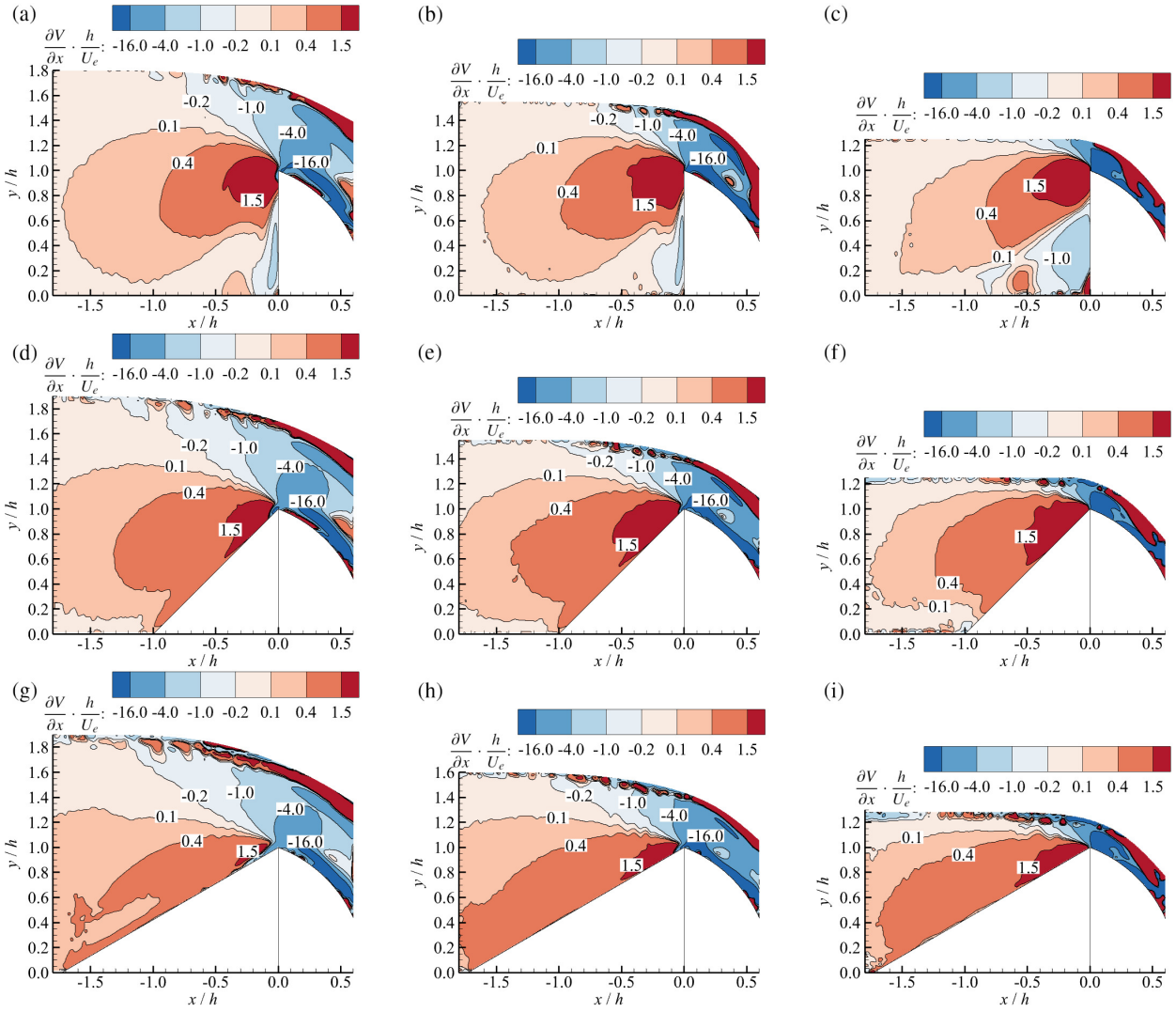

Figure 4.7. Contour plots of the normalized mean vertical acceleration: (a) $\theta = 90°$, $D_c/h = 0.7$; (b) $\theta = 90°$, $D_c/h = 0.4$; (c) $\theta = 90°$, $D_c/h = 0.2$; (d) $\theta = 45°$, $D_c/h = 0.7$; (e) $\theta = 45°$, $D_c/h = 0.4$; (f) $\theta = 45°$, $D_c/h = 0.2$; (g) $\theta = 30°$, $D_c/h = 0.7$; (h) $\theta = 30°$, $D_c/h = 0.4$; (i) $\theta = 30°$, $D_c/h = 0.2$.

Rheophilic species, such as salmonids and cyprinids, avoid rapidly accelerating flows even when encountering facilities at dams that are designed to guide them away from turbines (Williams et al., 2012). The modified spillways may improve the downstream migration of fish since, as evident from Figures 4.6(a)-(c) and 4.7(a)-(c), the contour levels are concentrated around the crest for the 90° standard spillway, whereas the contour levels are more uniformly distributed along the upstream face for the modified spillways, implying a more uniformly accelerating flow.

4.3. Reynolds stresses and turbulent kinetic energy (TKE)

4.3.1. Reynolds stresses

Figure 4.8 shows the contours of the normalized stream-wise Reynolds normal stress, $\overline{u'u'}/U_e^2$. Evidently, over the spillway, the magnitudes of the normalized Reynolds stresses increase as the water depth decreases. Furthermore, the magnitude of the Reynolds stresses upstream of the spillway is significantly reduced for the modified spillways due to the suppression of the flow separation.

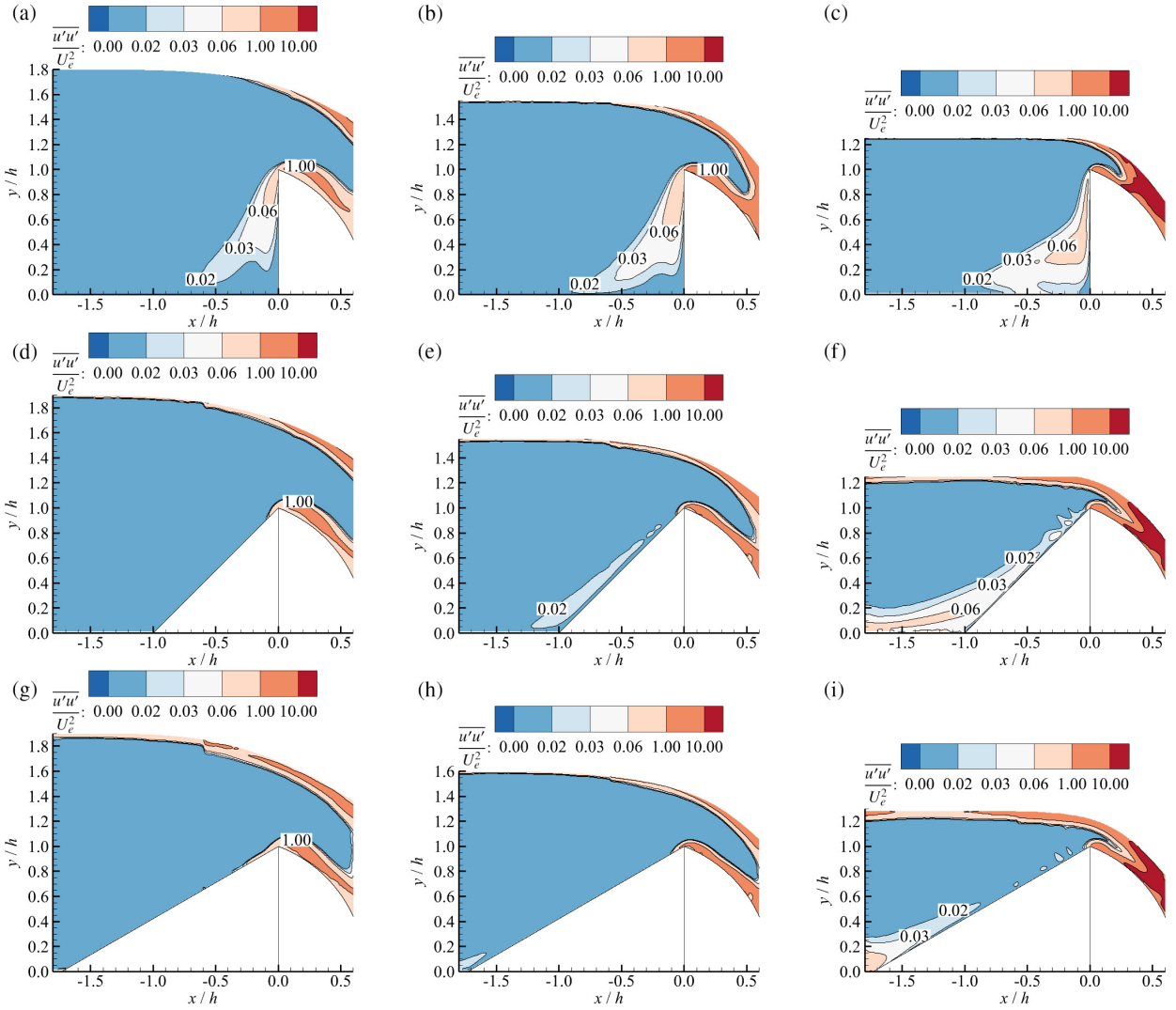

Figure 4.8. Contour plots of the normalized stream-wise Reynolds normal stress: (a) $\theta = 90°$, $D_c/h = 0.7$; (b) $\theta = 90°$, $D_c/h = 0.4$; (c) $\theta = 90°$, $D_c/h = 0.2$; (d) $\theta = 45°$, $D_c/h = 0.7$; (e) $\theta = 45°$, $D_c/h = 0.4$; (f) $\theta = 45°$, $D_c/h = 0.2$; (g) $\theta = 30°$, $D_c/h = 0.7$; (h) $\theta = 30°$, $D_c/h = 0.4$; (i) $\theta = 30°$, $D_c/h = 0.2$.

4. *Results and Discussion*

Contours of the normalized vertical Reynolds normal stress, $\overline{v'v'}/U_e^2$ are presented in Figure 4.9. The distributions of the vertical Reynolds normal stresses are qualitatively similar to those of the stream-wise Reynolds normal stresses. The most noticeable difference is observed upstream of the 90° standard spillway at $D_c/h = 0.2$, where the topology of the contours changes due to the presence of the recirculation bubble.

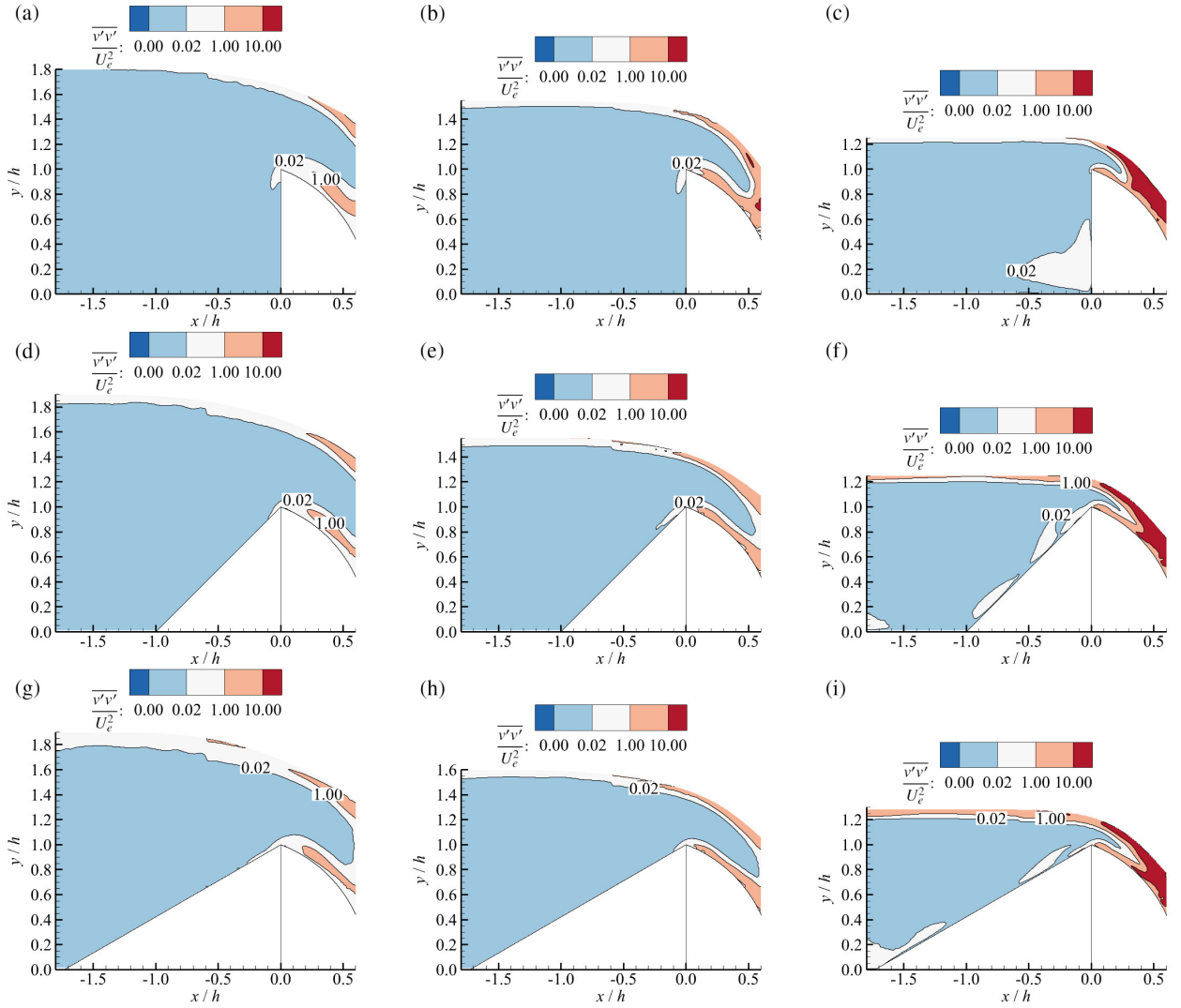

Figure 4.9. Contour plots of the normalized verical Reynolds normal stress: (a) $\theta = 90°$, $D_c/h = 0.7$; (b) $\theta = 90°$, $D_c/h = 0.4$; (c) $\theta = 90°$, $D_c/h = 0.2$; (d) $\theta = 45°$, $D_c/h = 0.7$; (e) $\theta = 45°$, $D_c/h = 0.4$; (f) $\theta = 45°$, $D_c/h = 0.2$; (g) $\theta = 30°$, $D_c/h = 0.7$; (h) $\theta = 30°$, $D_c/h = 0.4$; (i) $\theta = 30°$, $D_c/h = 0.2$.

Figure 4.10 shows the contours of the normalized Reynolds shear stress, $\overline{u'v'}/U_e^2$. High levels of shear stress may cause disorientation and localized injuries, especially if eddies are of scales similar to the size of the fish (Lupandin, 2005). Some fish, such as *Schizopygopsis younghusbandi*, may avoid regions of high shear stress values along the streamlines. Hence, Reynolds shear stress should be considered when designing downstream passage systems for this and possibly other fish species.

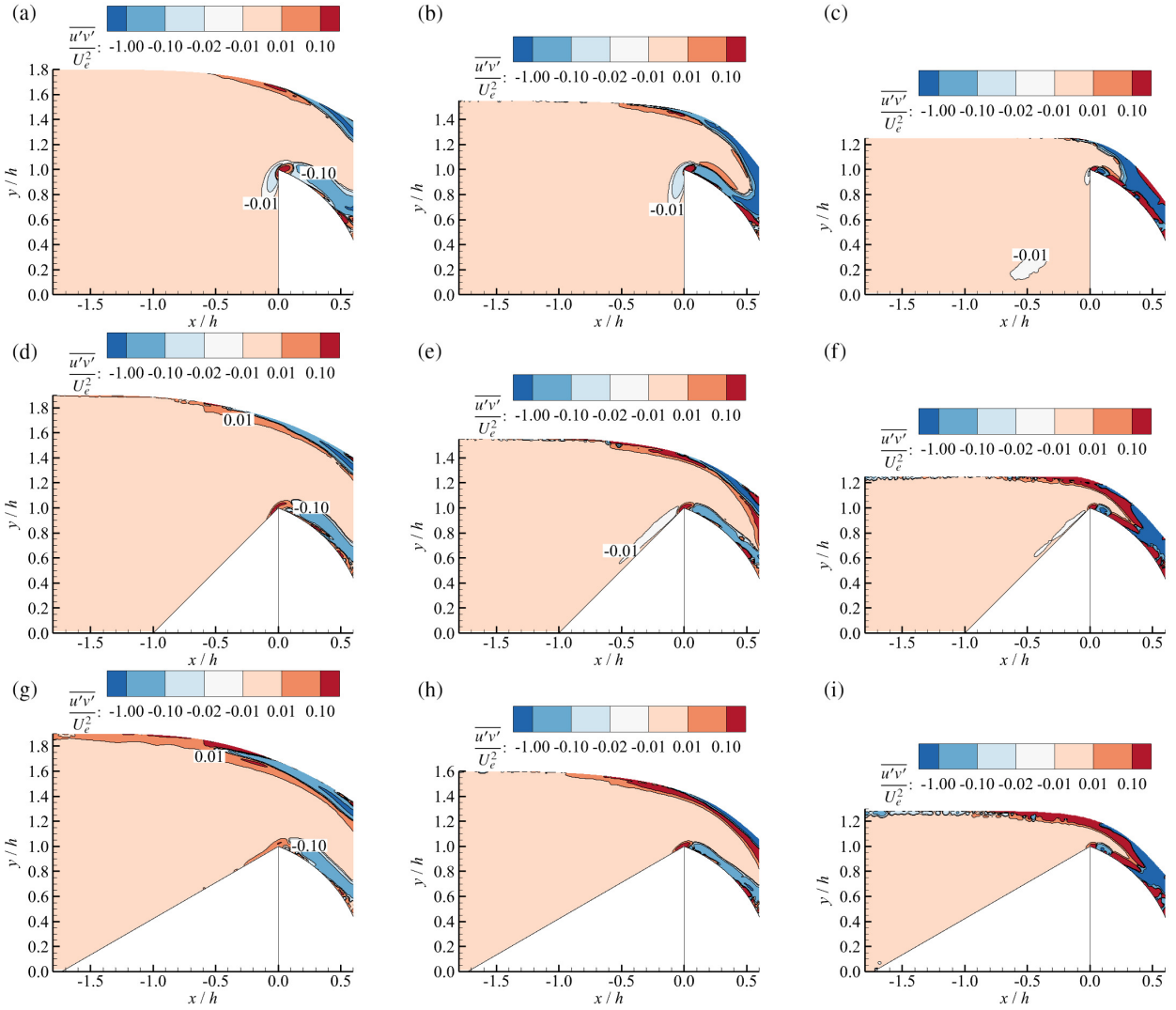

Figure 4.10. Contour plots of the normalized Reynolds shear stress: (a) $\theta = 90°$, $D_c/h = 0.7$; (b) $\theta = 90°$, $D_c/h = 0.4$; (c) $\theta = 90°$, $D_c/h = 0.2$; (d) $\theta = 45°$, $D_c/h = 0.7$; (e) $\theta = 45°$, $D_c/h = 0.4$; (f) $\theta = 45°$, $D_c/h = 0.2$; (g) $\theta = 30°$, $D_c/h = 0.7$; (h) $\theta = 30°$, $D_c/h = 0.4$; (i) $\theta = 30°$, $D_c/h = 0.2$.

4.3.2. Turbulent kinetic energy

Contours of the normalized turbulent kinetic energy, TKE/U_e^2, are provided in Figure 4.11. The turbulent kinetic energy is approximated using the following equation:

$$TKE = 0.75(\overline{u'u'} + \overline{v'v'}) \tag{4.1}$$

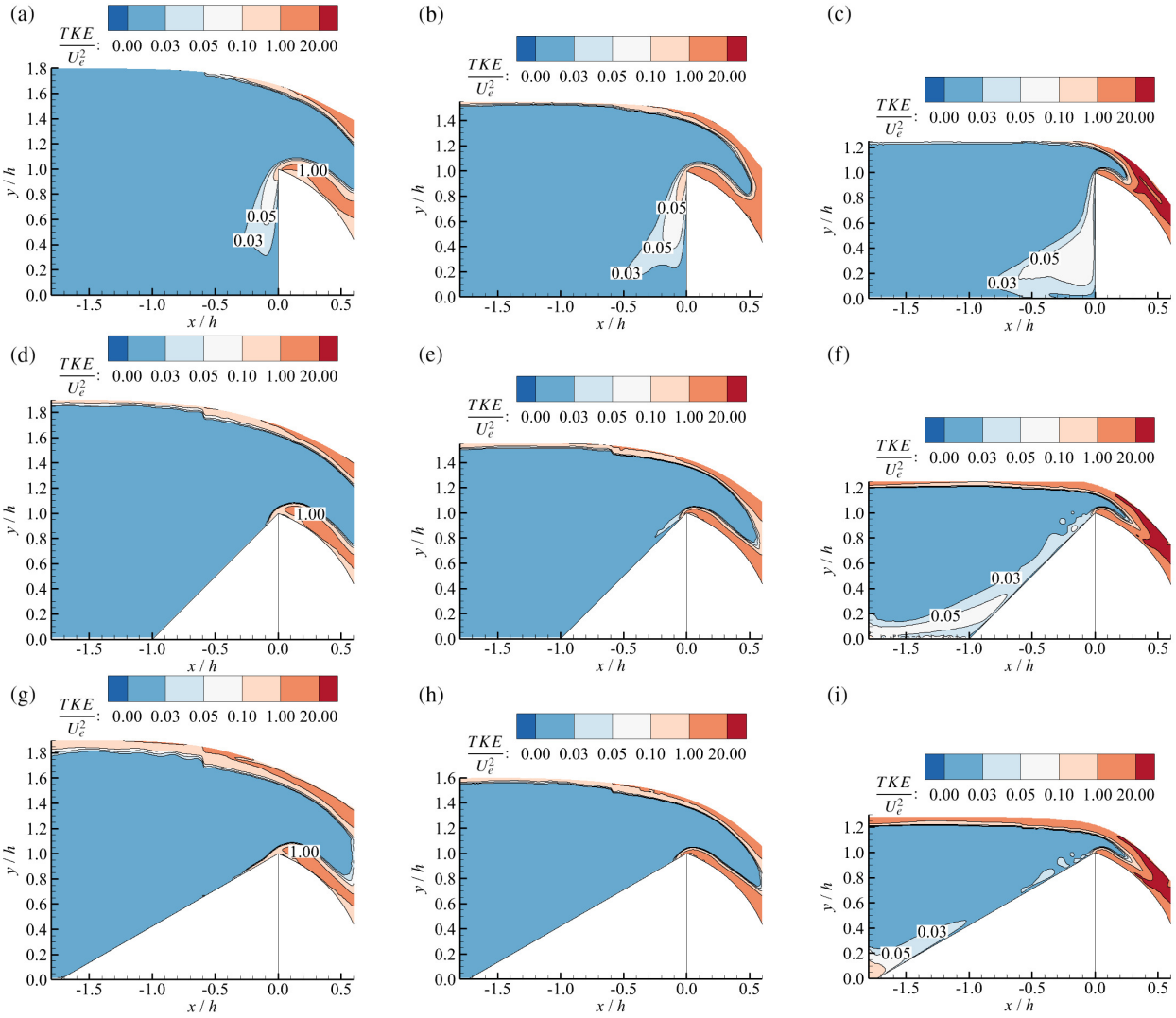

Figure 4.11. Contour plots of the normalized TKE: (a) $\theta = 90°$, $D_c/h = 0.7$; (b) $\theta = 90°$, $D_c/h = 0.4$; (c) $\theta = 90°$, $D_c/h = 0.2$; (d) $\theta = 45°$, $D_c/h = 0.7$; (e) $\theta = 45°$, $D_c/h = 0.4$; (f) $\theta = 45°$, $D_c/h = 0.2$; (g) $\theta = 30°$, $D_c/h = 0.7$; (h) $\theta = 30°$, $D_c/h = 0.4$; (i) $\theta = 30°$, $D_c/h = 0.2$.

In equation (4.1), it is assumed that the span-wise Reynolds normal stress, $\overline{w'w'}$, which could not be directly measured using planar PIV, is $\overline{w'w'} = 0.5(\overline{u'u'} + \overline{v'v'})$. From Figure 4.11, it can be seen that turbulence levels are significantly low upstream of the spillway except in the vicinity of the walls, where higher values are observed. As the flow passes the spillway crest, a region of elevated turbulence levels develops along the spillway surface due to the increase in velocity magnitudes.

Previous studies show that several fish species, such as the Iberian barbel, *Schizopygopsis younghusbandi*, rainbow trout (*Oncorhynchus mykiss*), Atlantic salmon, and the European eel, avoid highly turbulent regions, preferring low TKE values of $0.05\,\mathrm{m}^2/\mathrm{s}^2$, as a strategy to minimize disorientation, stresses, and energy expenditure required for maintaining their position (Santos et al., 2012; Silva et al., 2020; Shahabi et al., 2021). Downstream migrating fish also use low TKE areas to rest before passing through high accelerating flows. Hence, the modified spillways are expected to increase the downstream passage efficiency compared to the 90° standard spillway due to relatively lower turbulent kinetic energy values upstream of the spillway.

4.4. Budget terms of the TKE equation

The TKE equation in Cartesian tensor notation is as follows:

$$\frac{\partial k}{\partial t} + U_j \frac{\partial k}{\partial x_j} = -\overline{u_i' u_j'} \frac{\partial U_i}{\partial x_j} - \nu \overline{\frac{\partial u_i'}{\partial x_j} \frac{\partial u_i'}{\partial x_j}} + \frac{\partial}{\partial x_j} \left(\nu \frac{\partial k}{\partial x_j} - \frac{1}{2} \overline{u_i' u_i' u_j'} - \frac{1}{\rho} \overline{p' u_j'} \right) \tag{4.2}$$

In (4.2), both i and j are summation indices. The various terms in (4.2) are denoted by:

$$L_k + C_k = P_k - \epsilon + D_k^{\nu} + D_k^{t} + D_k^{p} \tag{4.3}$$

$$L_k = \frac{\partial k}{\partial t} \qquad C_k = U_j \frac{\partial k}{\partial x_j} \qquad P_k = -\overline{u_i' u_j'} \frac{\partial U_i}{\partial x_j} \qquad \epsilon = \nu \overline{\frac{\partial u_i'}{\partial x_j} \frac{\partial u_i'}{\partial x_j}}$$

$$D_k^{\nu} = \frac{\partial}{\partial x_j} \left(\nu \frac{\partial k}{\partial x_j} \right) \qquad D_k^{t} = -\frac{\partial}{\partial x_j} \left(\frac{1}{2} \overline{u_i' u_i' u_j'} \right) \qquad D_k^{p} = -\frac{\partial}{\partial x_j} \left(\frac{1}{\rho} \overline{p' u_j'} \right)$$

The terms on the left-hand side of (4.3) are the unsteady term, L_k, and the convection term, C_k. The first term on the right-hand side of (4.3), P_k, is called the production and represent the rate of production of k. The term ϵ on the right-hand side of (4.3) is known as the dissipation. This term represents the rate at which k is converted into thermal energy. The term D_k^{ν} on the right-hand side of (4.3) is called the molecular diffusion and represents the diffusion of k caused by molecular transport. The term D_k^{t} on the right-hand side of (4.3), is the turbulence diffusion. It represents the rate of transport of turbulent kinetic energy through the turbulent fluctuations. Finally, the last term on the right-hand side of (4.3), D_k^{p}, is called pressure diffusion, which is another form of turbulence transport due to the correlation of the fluctuating velocity and pressure.

Throughout this section, the distribution of the budget terms of the TKE equation with the exception of the pressure diffusion term is analyzed assuming the flow is statistically stationary and homogeneous in the span-wise direction. Under these assumptions it then follows that L_k, the mean span-wise velocity, W, and all partial derivatives with respect to z are zero. The results provide physical insight into the mechanism of turbulence transport and dissipation within the flow field while also serving as a guide for the development of computational fluid dynamics models.

4.4.1. Convection term

Contours of the normalized convection term, $C_k h/U_e^3$, are shown in Figure 4.12, where C_k is given by the following equation:

$$C_k = U\frac{\partial k}{\partial x} + V\frac{\partial k}{\partial y} \tag{4.4}$$

Due to the sudden increase in velocities, the magnitude of the convection is significantly higher over the spillway, and elevated regions of positive convection develop along the spillway and the free surface. It can be seen that the magnitudes of the normalized convection increase as the water depth decreases. Meanwhile, upstream of the spillway except near the walls, the convection increases as the upstream face inclination decreases, which is attributed to the increase in the velocity magnitudes.

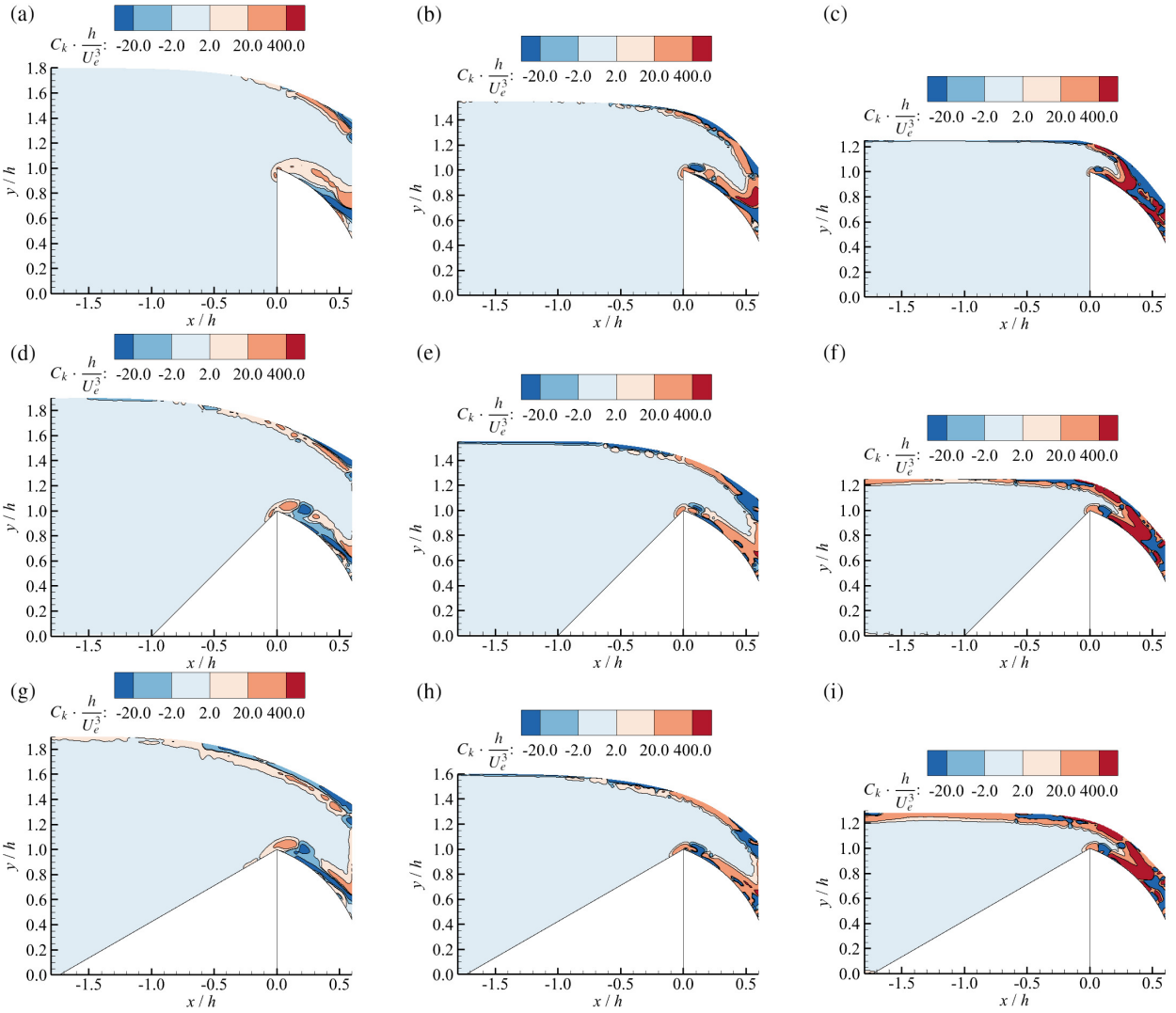

Figure 4.12. Contour plots of the normalized C_k: (a) $\theta = 90°$, $D_c/h = 0.7$; (b) $\theta = 90°$, $D_c/h = 0.4$; (c) $\theta = 90°$, $D_c/h = 0.2$; (d) $\theta = 45°$, $D_c/h = 0.7$; (e) $\theta = 45°$, $D_c/h = 0.4$; (f) $\theta = 45°$, $D_c/h = 0.2$; (g) $\theta = 30°$, $D_c/h = 0.7$; (h) $\theta = 30°$, $D_c/h = 0.4$; (i) $\theta = 30°$, $D_c/h = 0.2$.

4.4.2. Production term

Contours of the normalized production term, $P_k h/U_e^3$, are provided in Figure 4.13, where P_k is given by the following equation:

$$P_k = -\overline{u'u'}\frac{\partial U}{\partial x} - \overline{u'v'}\frac{\partial U}{\partial y} - \overline{u'v'}\frac{\partial V}{\partial x} - \overline{v'v'}\frac{\partial V}{\partial y} \tag{4.5}$$

Elevated regions of production are observed in the vicinity of the upstream face of the 90° standard spillway due to the instabilities of the separated shear layer and the recirculation bubble. Evidently, the magnitudes of the normalized production over the spillway increase as the water depth decreases. Decreasing the upstream face inclination leads to lower levels of turbulence near the crest of the spillway due to the suppression of the flow separation. The increase in the production magnitudes at the heel of the 45° and 30° modified spillways compared to the 90° standard spillway is attributed to streamline curvature and is clearly higher for the 45° modified spillway.

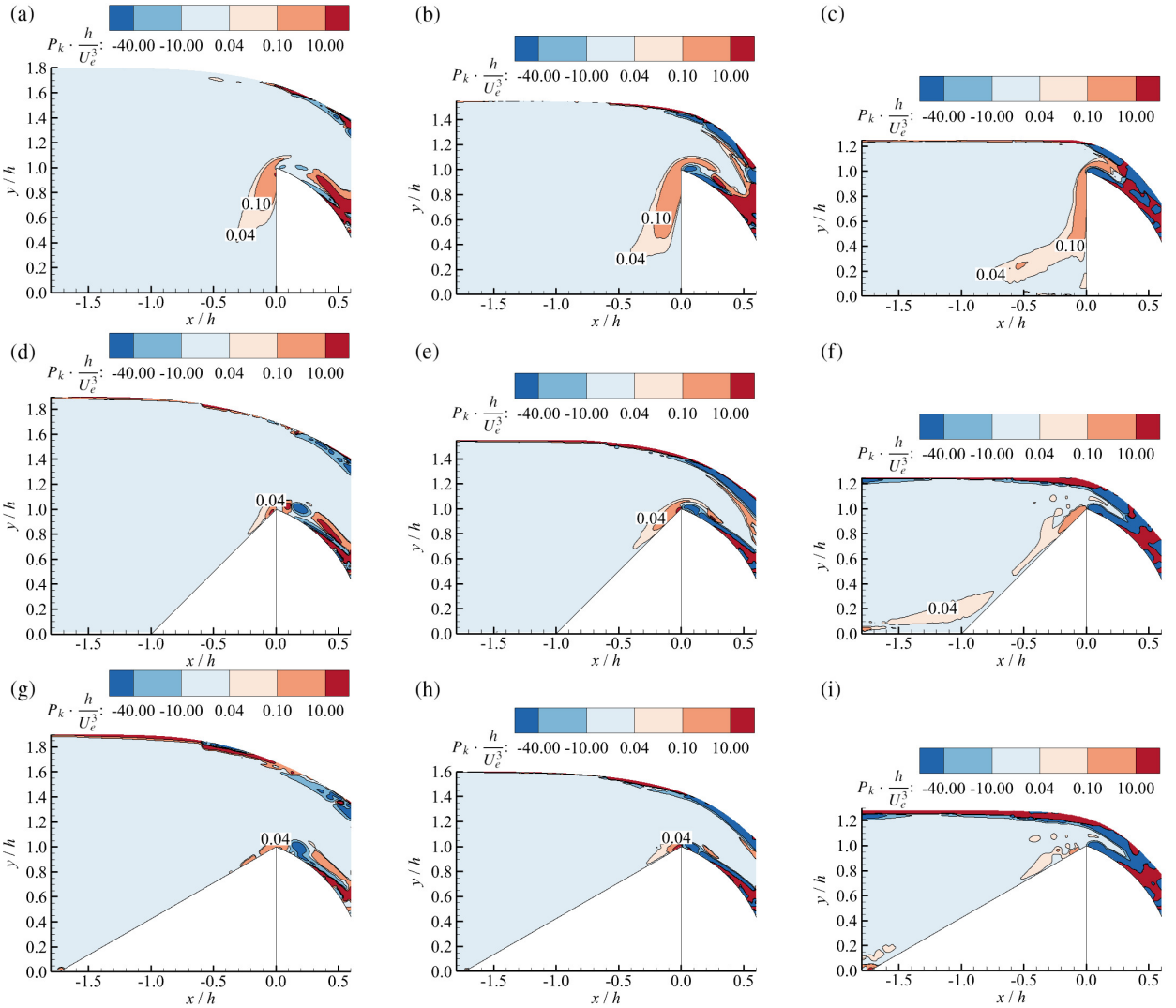

Figure 4.13. Contour plots of the normalized P_k: (a) $\theta = 90°$, $D_c/h = 0.7$; (b) $\theta = 90°$, $D_c/h = 0.4$; (c) $\theta = 90°$, $D_c/h = 0.2$; (d) $\theta = 45°$, $D_c/h = 0.7$; (e) $\theta = 45°$, $D_c/h = 0.4$; (f) $\theta = 45°$, $D_c/h = 0.2$; (g) $\theta = 30°$, $D_c/h = 0.7$; (h) $\theta = 30°$, $D_c/h = 0.4$; (i) $\theta = 30°$, $D_c/h = 0.2$.

4.4.3. Dissipation term

The distribution of the dissipation term is presented in Figure 4.14. The dissipation rate was obtained using the following relation:

$$\epsilon = \nu \left[2\overline{\left(\frac{\partial u'}{\partial x}\right)^2} + \overline{\left(\frac{\partial u'}{\partial y}\right)^2} + \overline{\left(\frac{\partial v'}{\partial x}\right)^2} + 2\overline{\left(\frac{\partial v'}{\partial y}\right)^2} + 2\overline{\left(\frac{\partial u'}{\partial x}\right)\left(\frac{\partial v'}{\partial y}\right)} + 2\overline{\left(\frac{\partial v'}{\partial x}\right)\left(\frac{\partial u'}{\partial y}\right)} \right] \tag{4.6}$$

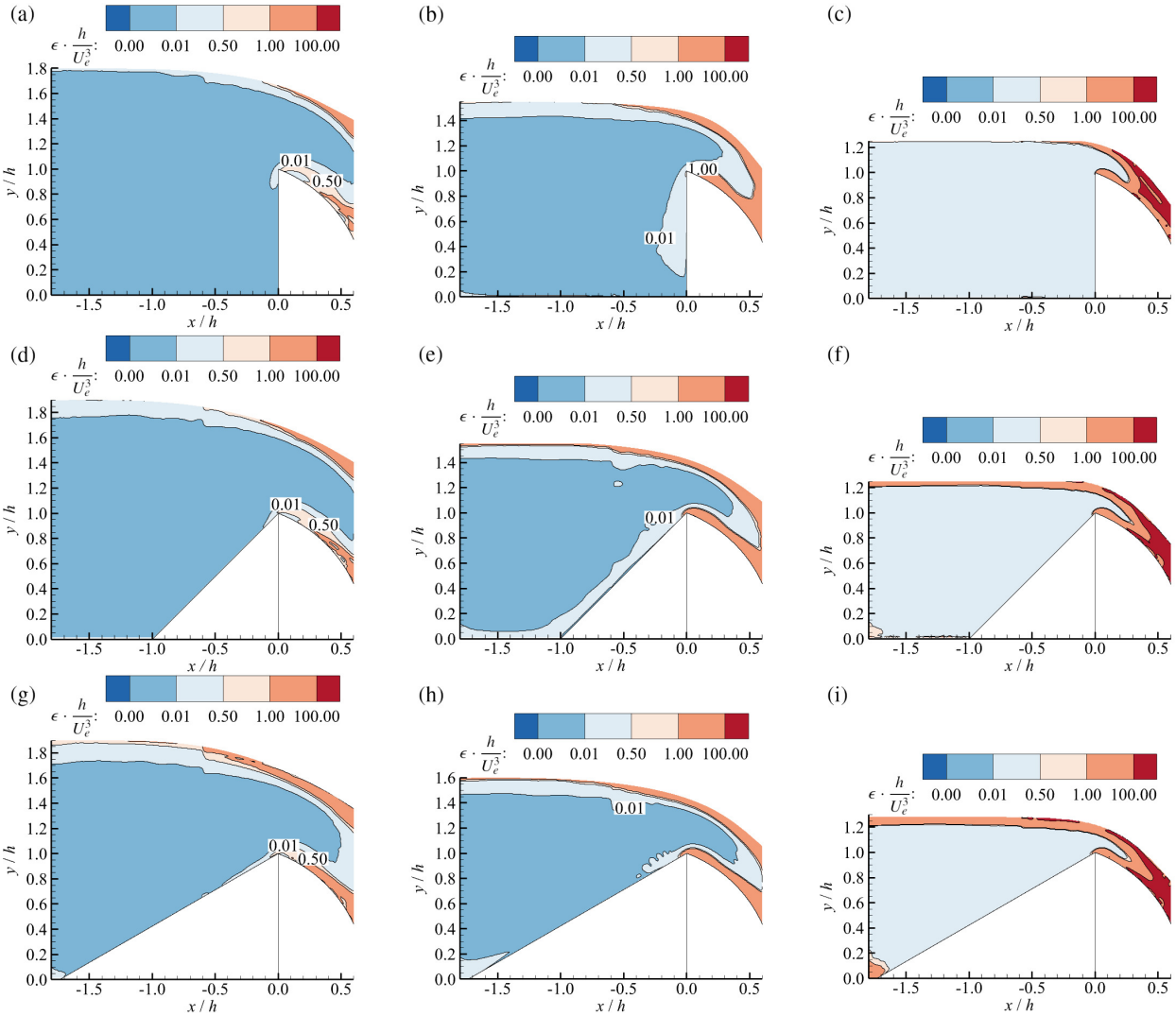

Figure 4.14. Contour plots of the normalized dissipation: (a) $\theta = 90°$, $D_c/h = 0.7$; (b) $\theta = 90°$, $D_c/h = 0.4$; (c) $\theta = 90°$, $D_c/h = 0.2$; (d) $\theta = 45°$, $D_c/h = 0.7$; (e) $\theta = 45°$, $D_c/h = 0.4$; (f) $\theta = 45°$, $D_c/h = 0.2$; (g) $\theta = 30°$, $D_c/h = 0.7$; (h) $\theta = 30°$, $D_c/h = 0.4$; (i) $\theta = 30°$, $D_c/h = 0.2$.

Due to the turbulent cascade phenomenon, the large eddies break into eddies of progressively smaller scales as the flow passes over the spillway, causing the dissipation rate to gradually increase in the stream-wise direction. Over the spillway, the normalized dissipation rate increases as the water depth decreases and is almost independent of the upstream face inclination. Upstream of the spillway, the dissipation rate is relatively higher in the vicinity of the upstream face and the crest.

4.4.4. Diffusion term

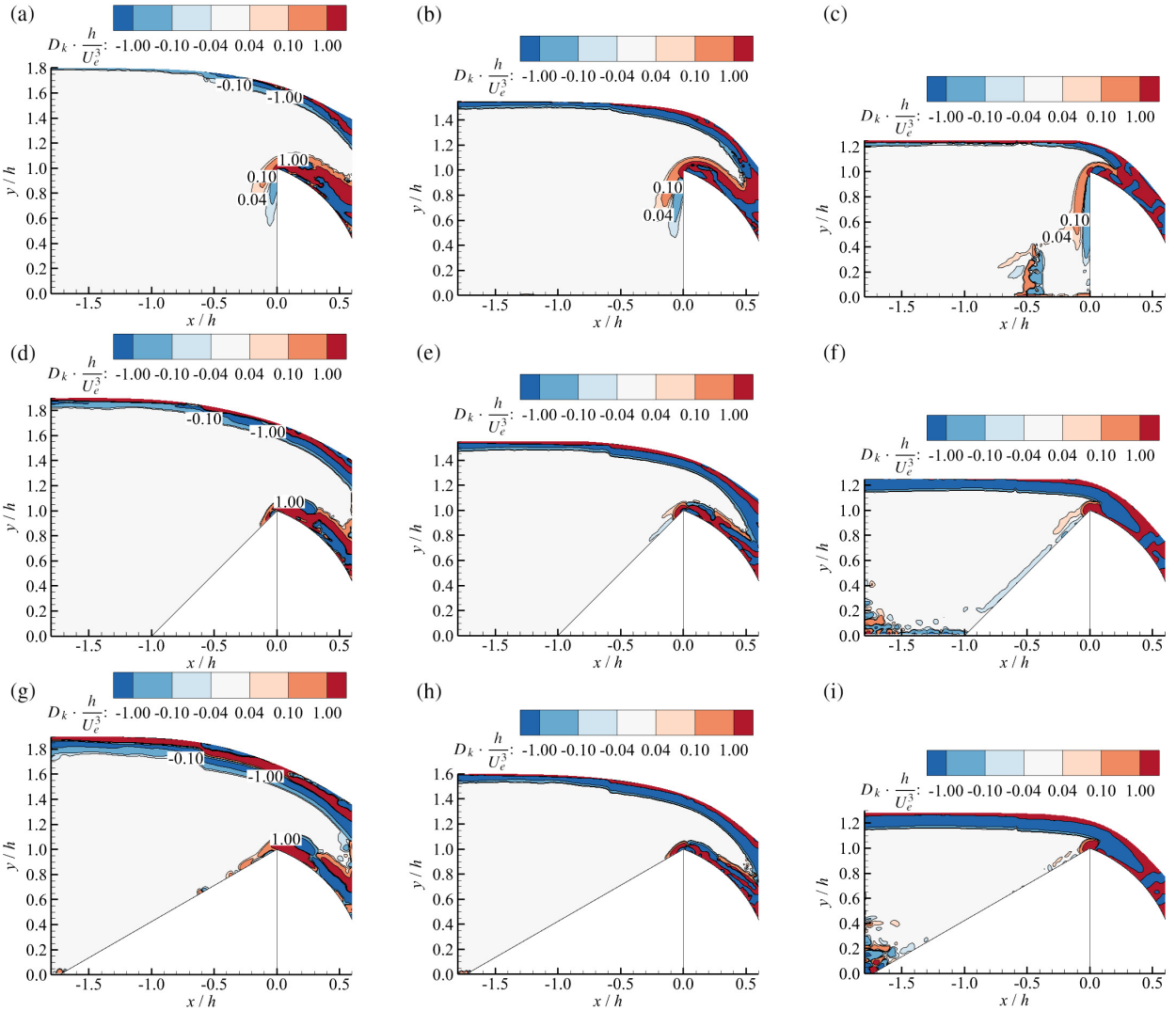

Figure 4.15. Contour plots of the normalized D_k: (a) $\theta = 90°$, $D_c/h = 0.7$; (b) $\theta = 90°$, $D_c/h = 0.4$; (c) $\theta = 90°$, $D_c/h = 0.2$; (d) $\theta = 45°$, $D_c/h = 0.7$; (e) $\theta = 45°$, $D_c/h = 0.4$; (f) $\theta = 45°$, $D_c/h = 0.2$; (g) $\theta = 30°$, $D_c/h = 0.7$; (h) $\theta = 30°$, $D_c/h = 0.4$; (i) $\theta = 30°$, $D_c/h = 0.2$.

Figure 4.15 shows the contours of the normalized diffusion term, $D_k h/U_e^3$. Here, D_k denotes the sum of the molecular diffusion and turbulence diffusion terms, and is as follows:

$$D_k = -\frac{1}{2}\left(\frac{\partial\overline{u'u'u'}}{\partial x} + \frac{\partial\overline{u'v'v'}}{\partial x} + \frac{\partial\overline{u'u'v'}}{\partial y} + \frac{\partial\overline{v'v'v'}}{\partial y}\right) + \nu\left(\frac{\partial^2 k}{\partial x^2} + \frac{\partial^2 k}{\partial y^2}\right) \tag{4.7}$$

The experimental results show that the molecular diffusion is at least two orders of magnitudes smaller than the turbulence transport. Evidently, the normalized values over the spillway increase as the water depth decreases, while the diffusion levels upstream of the spillway decrease as the upstream face inclination decreases due to the suppression of the separation.

4.5. Two-point correlations

Two-point correlations of the velocity fluctuations are used to investigate the effects of the water depth and upstream face inclination on the size and orientation of the large-scale eddies within the flow field. The two-point correlation functions are given by:

$$R_{u_i'u_j'}(x_0 + \Delta x, y_0 + \Delta y) = \frac{\overline{u_i'(x_0, y_0) \cdot u_j'(x_0 + \Delta x, y_0 + \Delta y)}}{\sqrt{\overline{u_i'u_i'}(x_0, y_0)} \cdot \sqrt{\overline{u_j'u_j'}(x_0 + \Delta x, y_0 + \Delta y)}} \tag{4.8}$$

For each test case, the two-point correlations were examined at three different locations upstream of the spillway, as summarized in Table 4.1. These locations were selected to characterize the streamwise evolution of the eddies as they approach the spillway.

Table 4.1. Summary of parameters for two-point correlations.

θ	90°			45°			30°		
x_0/h	−1.0	−0.5	−0.2	−1.0	−0.5	−0.2	−1.5	−1.0	−0.5
y_0/h	0.5	0.5	0.5	0.2	0.7	1.0	0.3	0.6	0.9

Contour plots of the two-point autocorrelations of the stream-wise velocity fluctuations, $R_{u'u'}$, for the 90° standard spillway are shown in Figure 4.16. It can be seen that the size of the turbulence structures increases as the flow approaches the spillway and decreases as the water depth decreases. In addition, the topology of the autocorrelation function is very similar for $D_c/h = 0.7$ and $D_c/h = 0.4$ test cases, whereas, for $D_c/h = 0.2$ test case, the structures are significantly different due to the presence of the recirculation bubble near the heel of the spillway.

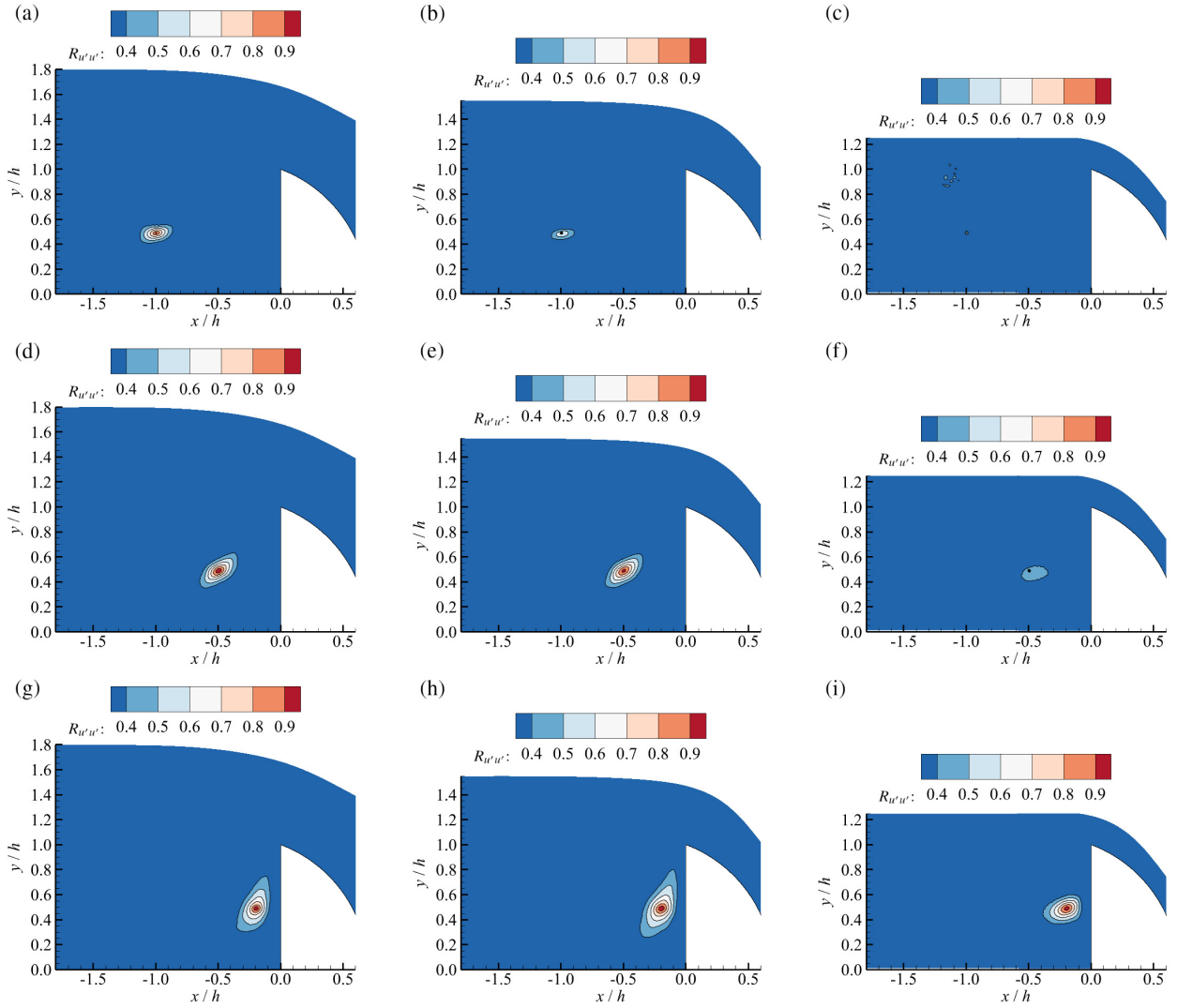

Figure 4.16. Contour plots of $R_{u'u'}$ for the standard 90° spillway at selected locations: (a), (d), and (g) $D_c/h = 0.7$; (b), (e), and (h) $D_c/h = 0.4$; (c), (f), and (i) $D_c/h = 0.2$;

Contour plots of the two-point autocorrelations of the stream-wise velocity fluctuations, $R_{u'u'}$, for the 45° modified spillway are shown in Figure 4.17. Evidently, the size of the turbulence structures decreases as the water depth decreases. Nonetheless, unlike the 90° standard spillway, the size of the turbulence structures decreases as the flow approaches the spillway, which is attributed to flow instabilities near the heel of the spillway. It is also interesting to note that the turbulent structures are aligned along the inclined upstream face of the spillway, irrespective of the water depth.

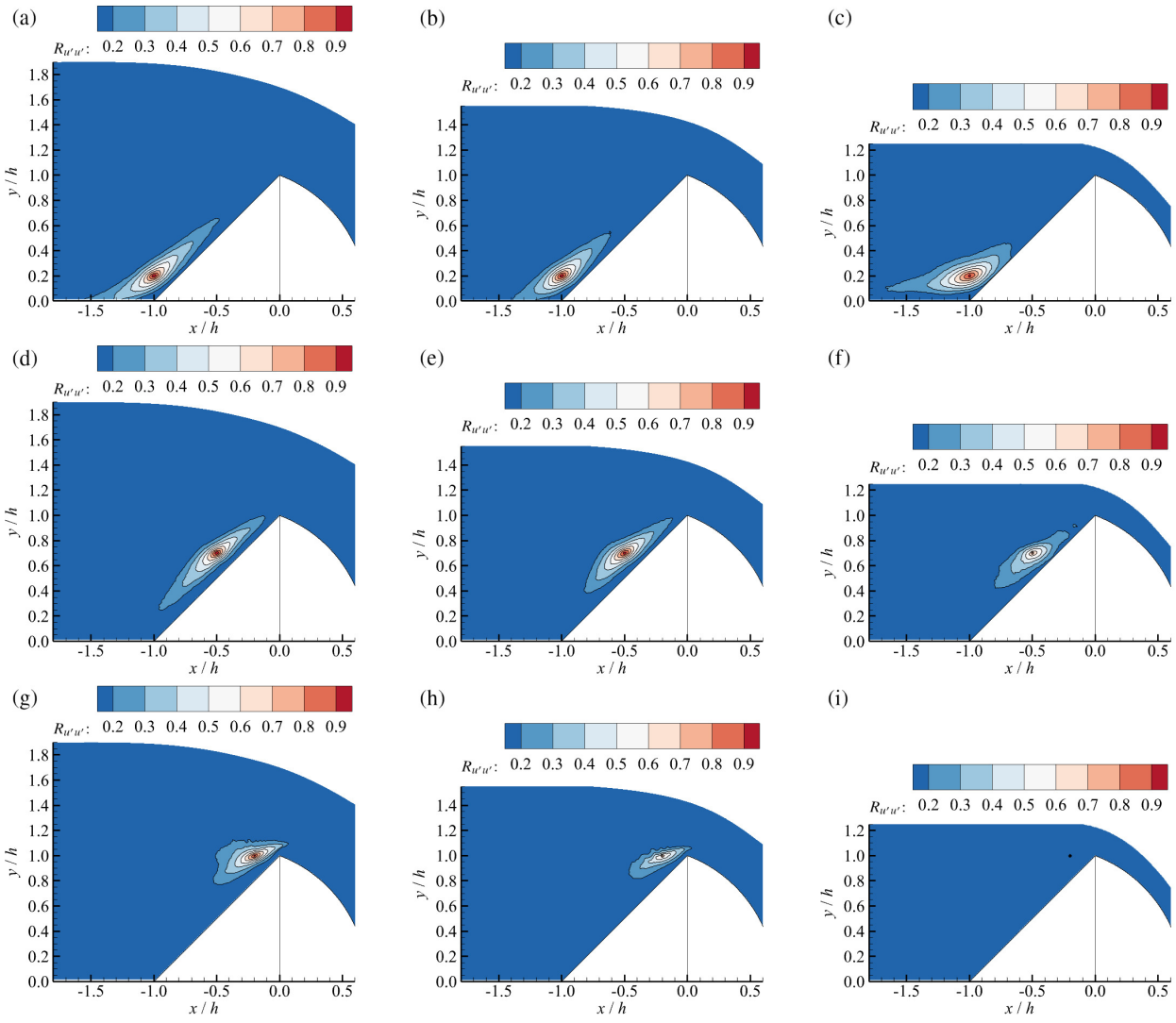

Figure 4.17. Contour plots of $R_{u'u'}$ for the standard 90° spillway at selected locations: (a), (d), and (g) $D_c/h = 0.7$; (b), (e), and (h) $D_c/h = 0.4$; (c), (f), and (i) $D_c/h = 0.2$;

Similar observations are noted for the contour plots of the two-point autocorrelations of the stream-wise velocity fluctuations, $R_{u'u'}$, for the 30° modified spillway, as shown in Figure 4.18. Comparing Figures 4.16, 4.17, and 4.18, it can be concluded that the size of the turbulent structures along the upstream face of the spillway decreases as the upstream face inclination decreases.

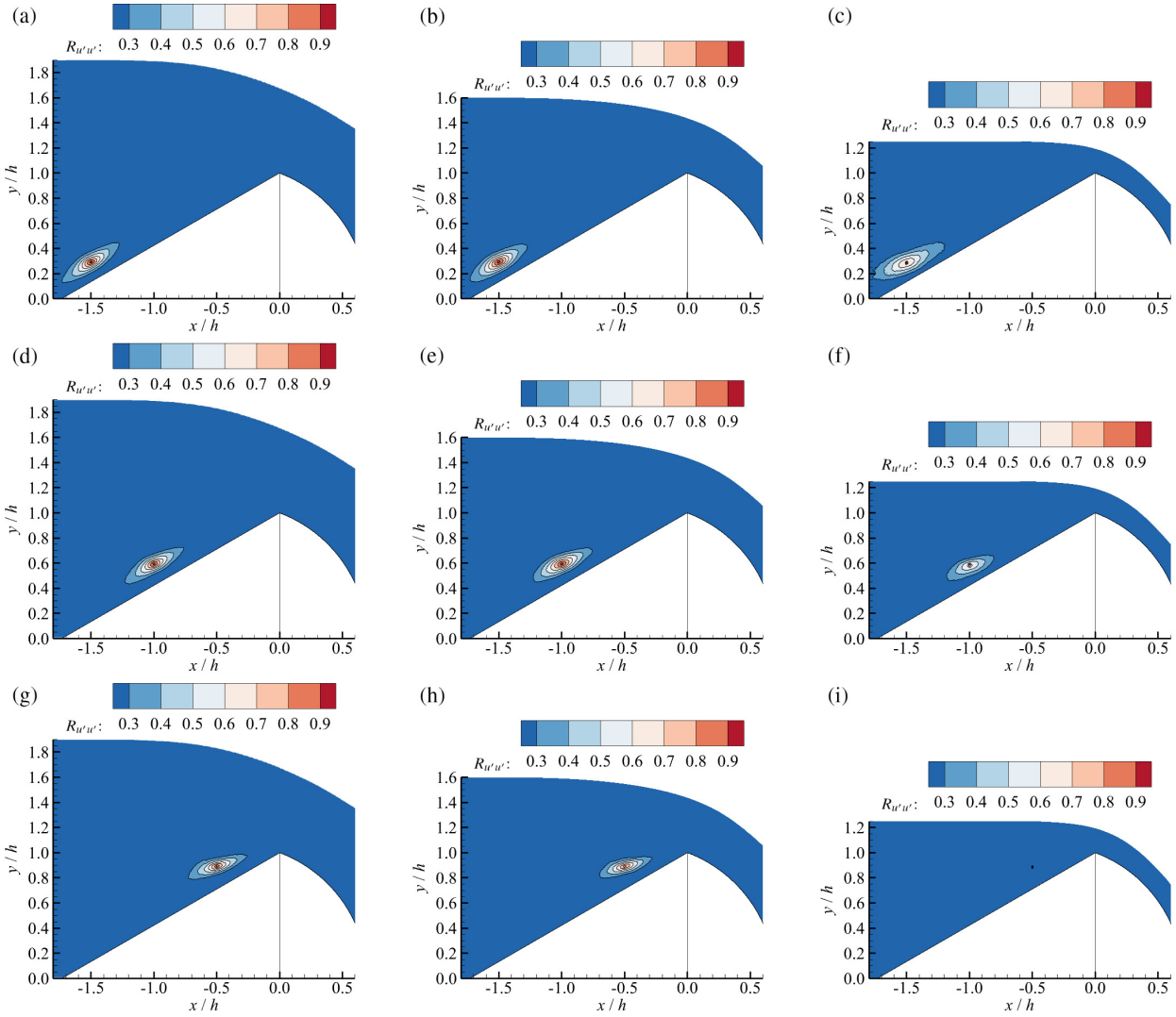

Figure 4.18. Contour plots of $R_{u'u'}$ for the standard 90° spillway at selected locations: (a), (d), and (g) $D_c/h = 0.7$; (b), (e), and (h) $D_c/h = 0.4$; (c), (f), and (i) $D_c/h = 0.2$;

4.6. Frequency spectra

Frequency spectral density of the stream-wise velocity fluctuations are used to evaluate the periodicity of the eddies within the flow field. The periodicity of an eddy is expressed in terms of the Strouhal number, which is a dimensionless parameter used to characterize the frequency of eddy motions, and is defined as $St = fh/U_e$, where f is the eddy frequency. Spectra analysis were performed for two test cases and at three different locations, as shown in Table 4.2.

Table 4.2. Summary of parameters for frequency spectra analysis.

θ	D_c/h	x_0/h	y_0/h	Description
90°	0.7	0.1407	1.0840	Maximum of U
		0.0660	1.0773	Maximum of $\overline{u'u'}$
		−0.2000	0.5000	Upstream location
	0.4	0.1167	1.0980	Maximum of U
		0.0567	1.0813	Maximum of $\overline{u'u'}$
		−0.2000	0.5000	Upstream location

The effects of the water depth on the spectral density profiles are examined in Figures 4.20, 4.21, and 4.19. For each plot, the profiles are compared to the well-known $-5/3$ slope in order to determine the inertial subrange and the dominant low- and high-frequency. The dominant low and high frequencies of the eddies are indicated by the vertical dash lines that correspond to the respective Strouhal number. A summary of dominant low- and high-frequency Strouhal numbers is also provided in Table 4.3.

From Figure 4.19, it is clear that at the upstream location, the profiles are independent of the water depth, except in the low-frequency region. On the other hand, Figures 4.20 and 4.21 indicate that over the spillway, the variations in spectral density due to changes in water depth are significant. For instance, at the location of the maximum of the mean stream-wise velocity, the spectral density

decreases as the water depth decreases, whereas at the location of the maximum of the stream-wise Reynolds stress, the spectral density increases as the water depth decreases. Furthermore, the inertial subrange at the upstream location is significantly wider compared to the locations over the spillway.

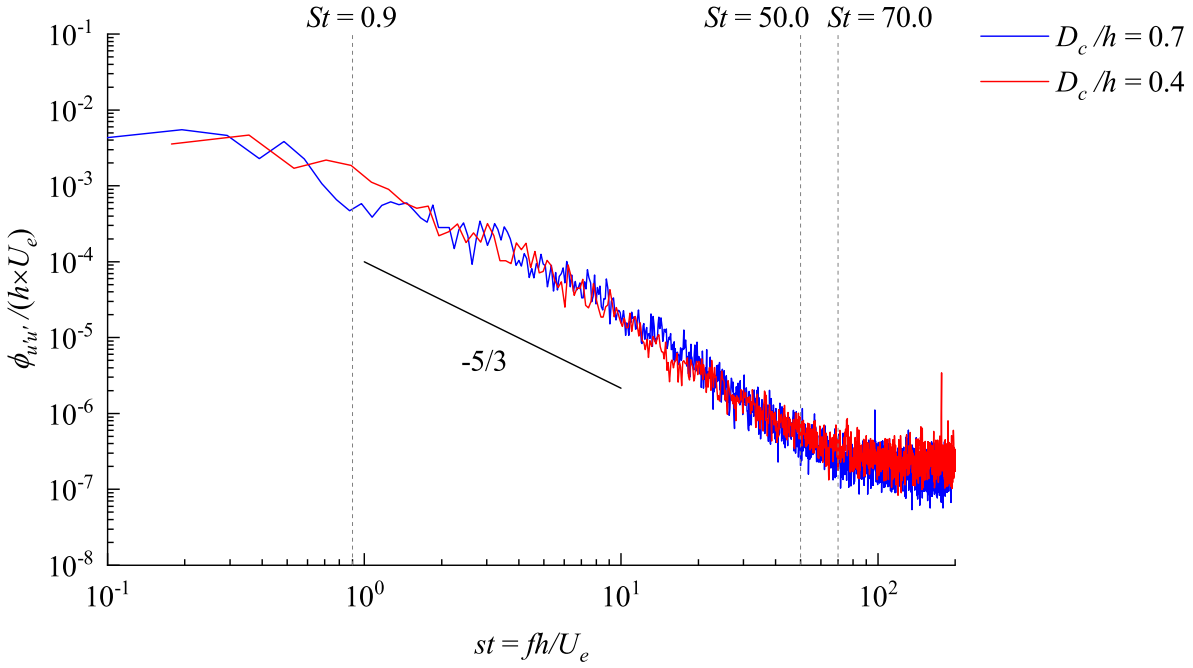

Figure 4.19. Frequency spectra density of the stream-wise fluctuating velocity, $\phi_{u'u'}$, at the selected upstream location for the 90° standard spillway.

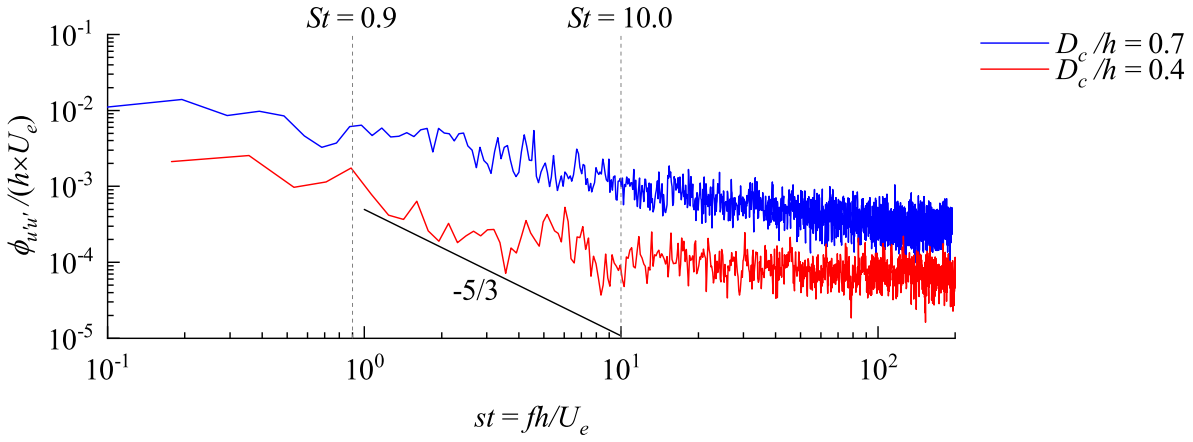

Figure 4.20. Frequency spectra density of the stream-wise fluctuating velocity, $\phi_{u'u'}$, at the location of maximum of U for the 90° standard spillway.

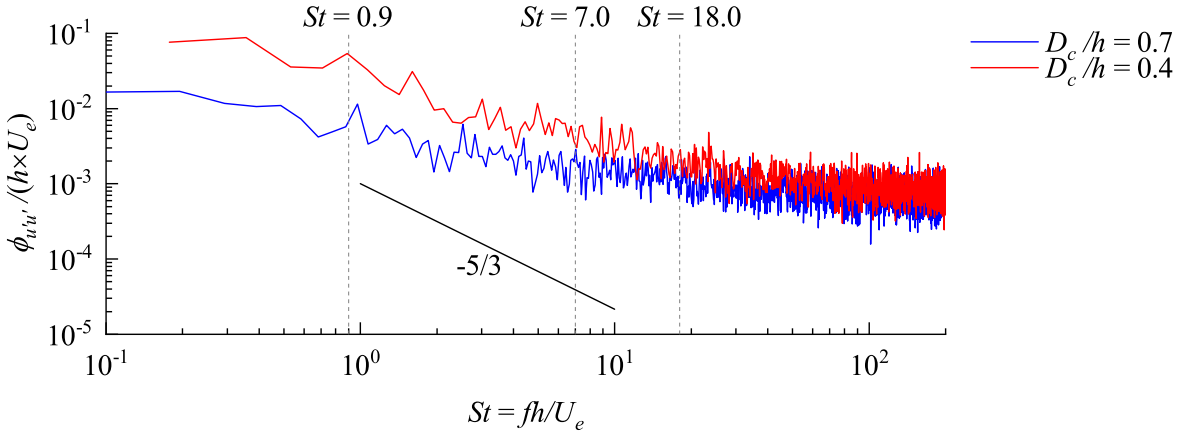

Figure 4.21. Frequency spectra density of the stream-wise fluctuating velocity, $\phi_{u'u'}$, at the location of maximum of $\overline{u'u'}$ for the 90° standard spillway.

From Table 4.3, it can be concluded that the inertial subrange becomes more distinct and occupies a wider range as the water depth decreases. Furthermore, the dominant low- and high-frequency motions do not vary significantly with water depth at the selected locations.

Table 4.3. Summary of dominant Strouhal numbers, St, at the selected locations.

D_c/h	x_0/h	y_0/h	Low	High
	0.1407	1.0840	0.9	10.0
0.7	0.0660	1.0773	0.9	7.0
	−0.2000	0.5000	0.5	50.0
	0.1167	1.0980	0.9	10.0
0.4	0.0567	1.0813	0.9	18.0
	−0.2000	0.5000	0.5	70.0

4.7. Characterization of a water jet over a convex surface

In this section of the thesis, the behavior of the flow over the curved downstream segment of the spillway is analyzed. The goal is to find semi-experimental expressions to represent the distribution of the mean velocities.

4.7.1. A description of the flow

The flow over the circular downstream section of the spillway and the stream-wise velocity profile are sketched in Figure 4.22. The employed coordinate systems are the same as those described in Figure 3.2(b).

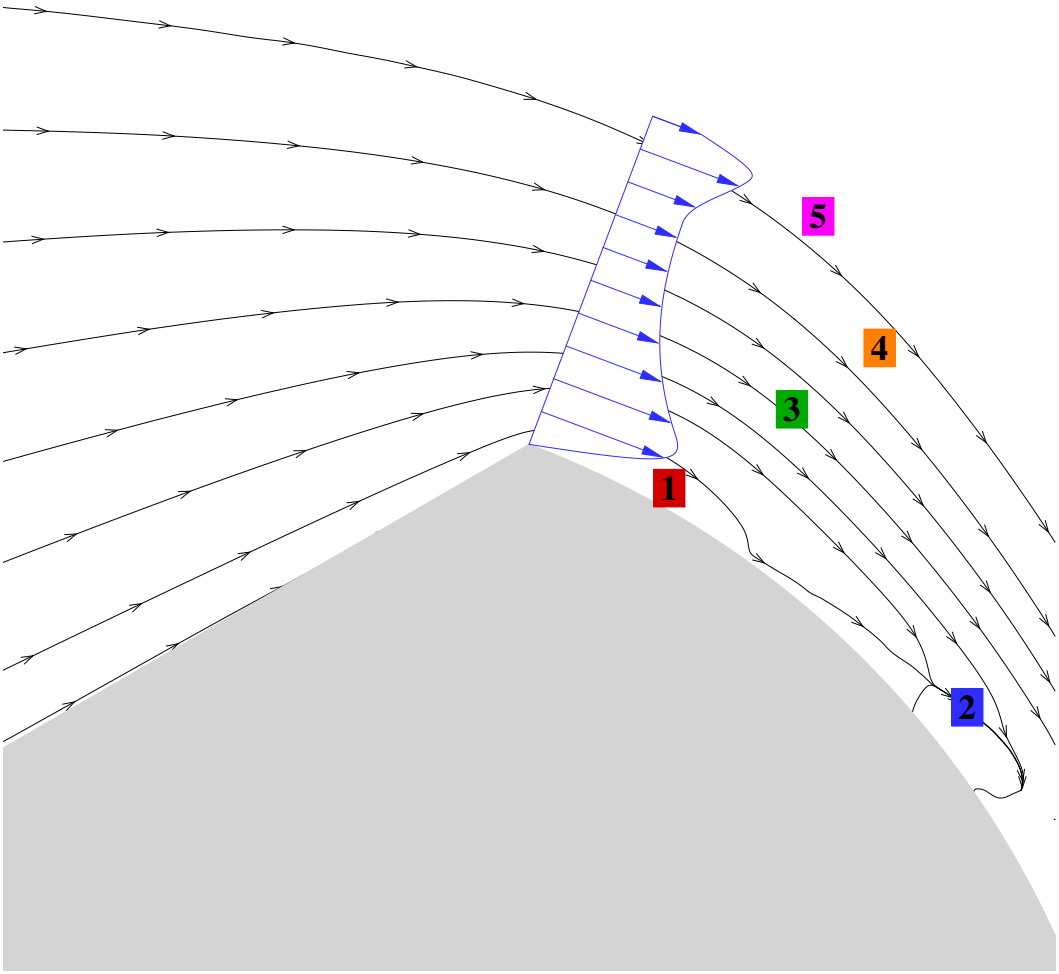

Figure 4.22. A sketch showing the flow over the spillway and regions of interest.

The restriction of the flow cross-sectional area upstream of the spillway produces a stream-wise velocity profile, U_α, that does not increase continuously to its free-stream value but rather increases to a maximum value before decreasing to its minimum close to the free surface. This kind of flow behavior is typically observed when high momentum fluid is injected into a boundary layer using a jet or a nozzle and is often referred to as the wall-jet boundary layer. The oncoming flow is separated due to the sharp leading edge and the inclined surface of the spillway at the crest, forming a recirculation bubble, denoted as region 1. The flow is reattached somewhere over the spillway surface, where a turbulent wall jet develops over the convex surface of the spillway, which is designated as region 2. At a far enough distance from the spillway surface, in region 3, the flow is unaffected by the wall and is irrotational. The flow is also restricted by the free surface, and consequently, a highly turbulent region develops along the free surface, that is, region 5. The flow in region 4 is free from the effects of the free surface and is in rigid-body rotation. It should be noted that, after developing sufficiently in the circumferential direction, regions 2 and 5 merge together, forming a jet of water over the convex surface of the spillway.

In the present study, we confine our attention to regions 3 and 4, where the flow may be considered homogeneous in the span-wise direction. The span-wise homogeneity was validated using the PIV data and the continuity equation:

$$\frac{\partial W}{\partial z} = -\frac{\partial U}{\partial x} - \frac{\partial V}{\partial y} \tag{4.9}$$

The analysis are mainly performed for the 30° modified spillway at a water depth of $D_c/h = 0.4$ since this test case provides the maximum field of view for examining regions 3 and 4. For other test cases, the analysis are repeated only when a significant difference is observed. To visualize the stream-wise evolutions, one-dimensional profiles are evaluated at eleven successive locations, starting at $s/h = 0.00$ and ending at $s/h = 0.50$ with an increment of $0.05h$, while the range of the normal axis is limited to $n/h = 0.4$.

4.7.2. Coordinate transformation

Since the PIV measurements were conducted using a Cartesian coordinate system, there is the need to transform the measured mean velocities through the following set of equations:

$$U_\alpha = U\cos(\alpha) - V\sin(\alpha) \tag{4.10}$$

$$V_r = U\sin(\alpha) + V\cos(\alpha) \tag{4.11}$$

4.7.3. Mean span-wise vorticity

The stream-wise evolution of the normalized mean span-wise vorticity, $\Omega_z \cdot h/U_e$, is presented in Figure 4.23. As the profiles evolve in the stream-wise direction, the thickness of the irrotational region decreases, whereas the rigid-body rotation region becomes wider. Furthermore, although the mean span-wise vorticity is constant in the radial direction in region 4, it still varies in the circumferential direction, that is, $\Omega_z = \Omega_z(\alpha)$.

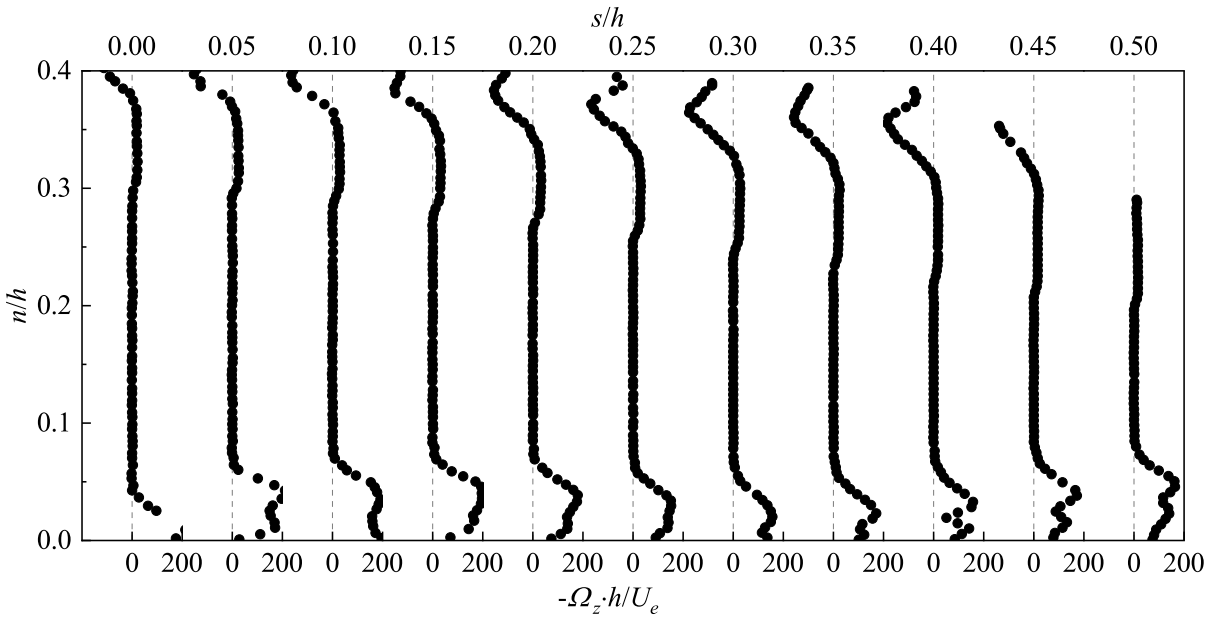

Figure 4.23. Stream-wise evolution of the normalized mean span-wise vorticity profiles over the 30° modified spillway at $D_c/h = 0.4$.

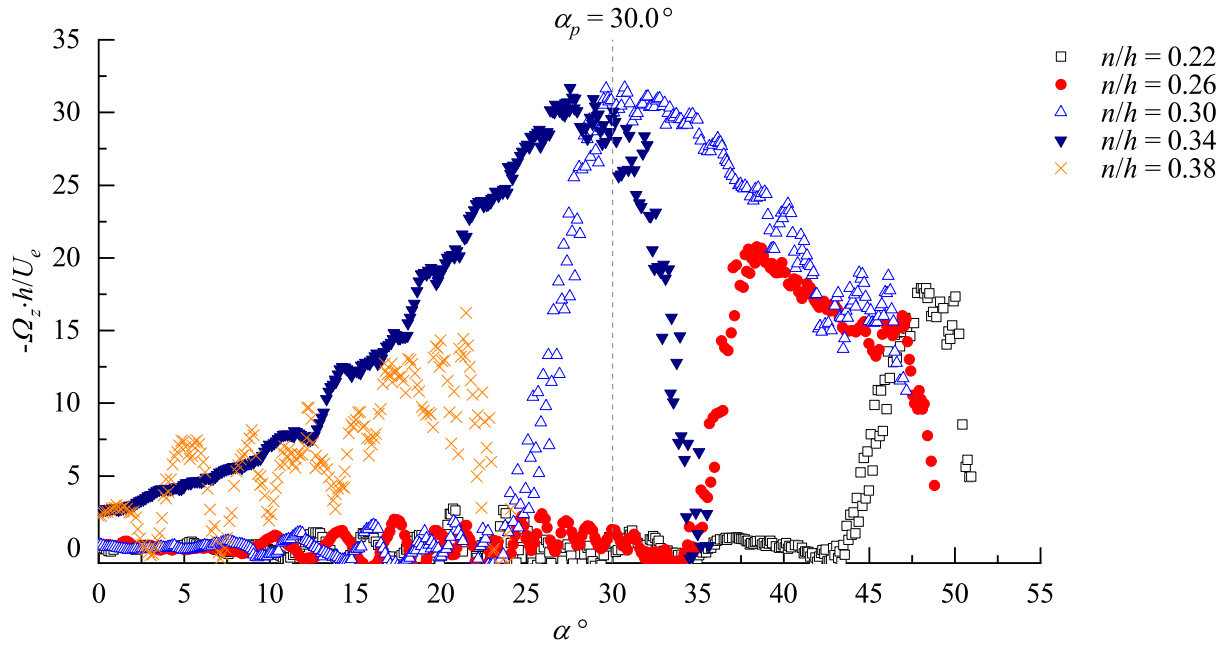

Figure 4.24. Plot of the normalized mean span-wise vorticity against the circumferential position for several polar lines over the 30° modified spillway at $D_c/h = 0.4$.

Figure 4.24 shows the plot of the normalized mean span-wise vorticity, for several polar lines over the 30° modified spillway at $D_c/h = 0.4$. It should be noted that polar lines span multiple regions and only a segment of them is located in region 4. These segments are collected and attached together, as presented in Figure 4.25. From Figures 4.24 and 4.25, it can be seen that the mean span-wise vorticity increases before reaching its peak at $\alpha \approx 30°$ and then gradually decreases as the flow leaves the spillway. The mean span-wise vorticity is apparently symmetric, and consequently, a wave function of the following form was fitted to the experimental results:

$$\Omega_z = \Omega_0 + a \sin\left(\pi \frac{\alpha - \alpha_p}{w} + \frac{\pi}{2}\right) \tag{4.12}$$

The fit curve is shown in figure 4.25 to allow the comparison with the experimental data. The employed fitting method was Levenberg-Marquardt, where a coefficient of determination, R^2, of 0.980 was reached, indicating a good agreement between the experimental and the predicted values.

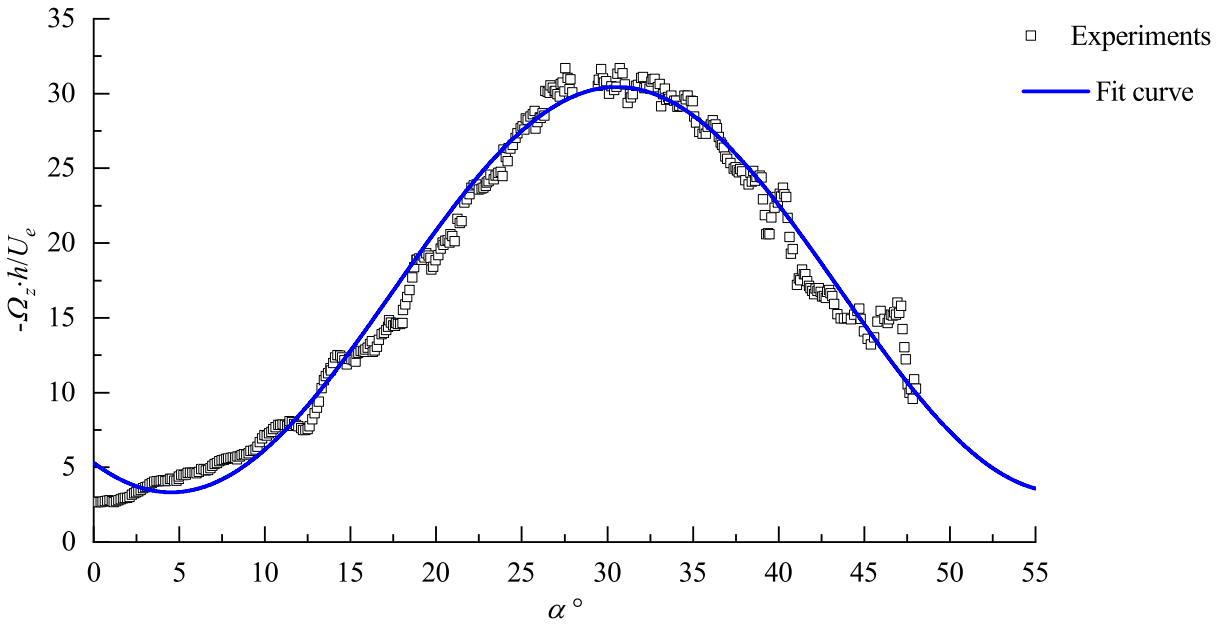

Figure 4.25. Comparison of the experimental data with the fitted sine function for the normalized mean span-wise vorticity over the 30° modified spillway at $D_c/h = 0.4$.

4.7.4. Angular momentum and the mean velocities

Consider a hypothetical flow for which the angular momentum is invariant in the radial direction, in other words, $rU_\alpha = L(\alpha)$. If such a flow were to be homogeneous in the span-wise direction and irrotational, by the vorticity and continuity equations, we have:

$$\Omega_z = 0 \Rightarrow \frac{\partial rU_\alpha}{\partial r} = \frac{\partial V_r}{\partial \alpha} \tag{4.13}$$

$$\frac{\partial W}{\partial z} = 0 \Rightarrow \frac{\partial U_\alpha}{\partial \alpha} + \frac{\partial rV_r}{\partial r} = 0 \tag{4.14}$$

Now, since $rU_\alpha = L(\alpha)$, we have:

$$\frac{\partial rV_r}{\partial r} = -\frac{\partial U_\alpha}{\partial \alpha} = -\frac{L'}{r} \Rightarrow rV_r = -L' \ln r + f(\alpha)$$

$$\frac{\partial V_r}{\partial \alpha} = \frac{\partial rU_\alpha}{\partial r} = 0 \Rightarrow f' = L'' \ln(r) \tag{4.15}$$

For (4.15) to hold for all values of r and α, the right-hand side cannot be a function of r, and consequently, $L'' = 0$. From $f' = L'' \ln(r)$, it immediately follows that $f' = 0$. Hence, it is concluded that for such a flow the angular momentum must vary linearly in the circumferential direction, in other words:

$$L = A\alpha + B \tag{4.16}$$

$$f = C \tag{4.17}$$

$$U_\alpha = \frac{L(\alpha)}{r} = \frac{A\alpha + B}{r} \tag{4.18}$$

$$V_r = \frac{-A\ln(r) + C}{r} \tag{4.19}$$

Next, let us examine whether any of the previously mentioned assumptions apply to the flow over the spillway. The stream-wise evolution of the normalized angular momentum, $L/(h \cdot U_e)$, is shown in Figure 4.26.

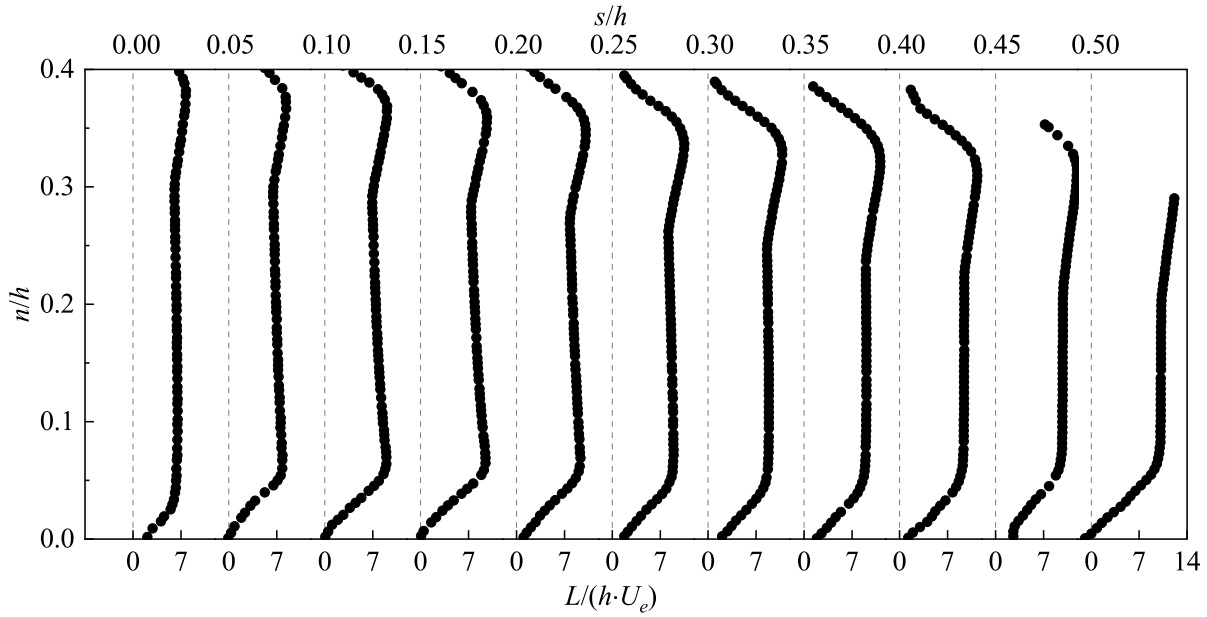

Figure 4.26. Stream-wise evolution of the normalized angular momentum profiles over the 30° modified spillway at $D_c/h = 0.4$.

From Figure 4.26, it is evident that in the vicinity of the recirculation zone, the angular

momentum varies significantly in the normal direction, and consequently, equations (4.16)-(4.19) are not valid. Away from the recirculation zone, however, angular momentum is invariant with respect to the distance from the wall. As a result, the constants A, B, and C in equations (4.16)-(4.19), may be obtained by fitting a line to the experimental data.

Figures 4.27 and 4.28 presents the variations of the angular momentum and the radial velocity in the circumferential direction for several polar lines. From Figure 4.27, it can be seen that the angular momentum is a constant for all polar lines at the crest. The profiles diverge as the flow evolves over the recirculation zone before converging to the same value near the reattachment point. After the wall jet is reattached over the the spillway, the profiles almost collapse on top of one another and vary linearly in the circumferential direction. Figure 4.28 further confirms the previous assumptions as $\partial V_r/\partial\alpha$, although not exactly zero, is significantly small over the linear range of the angular momentum.

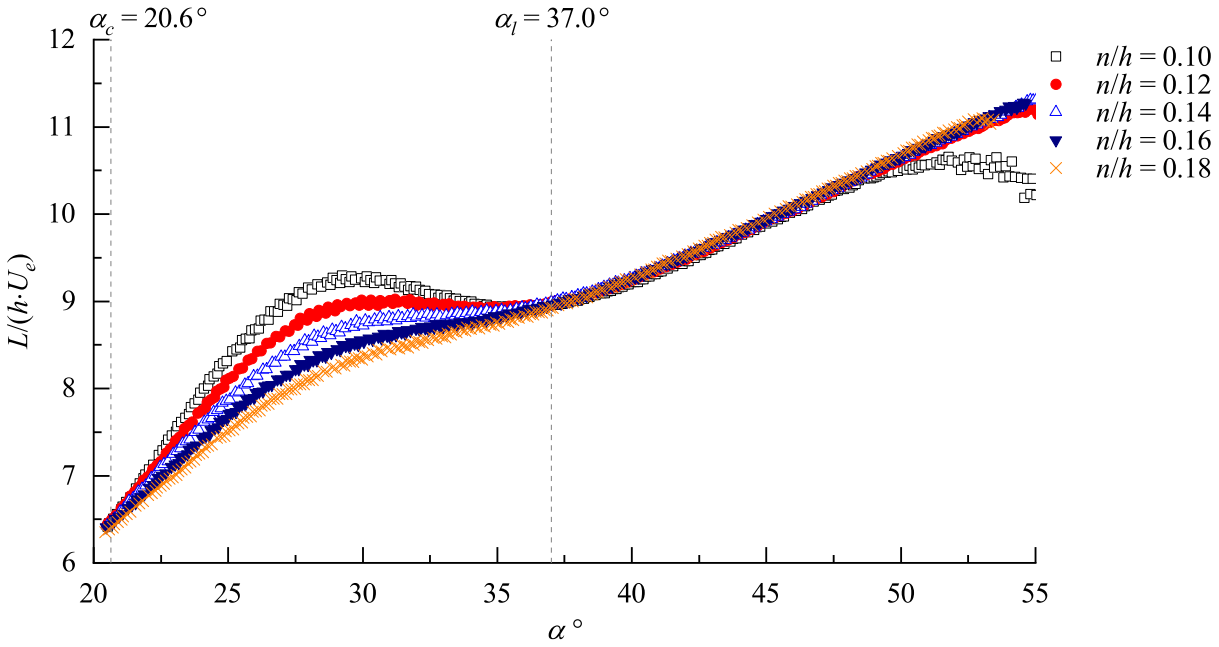

Figure 4.27. Plot of the normalized angular momentum against the circumferential position for several polar lines over the 30° modified spillway at $D_c/h = 0.4$.

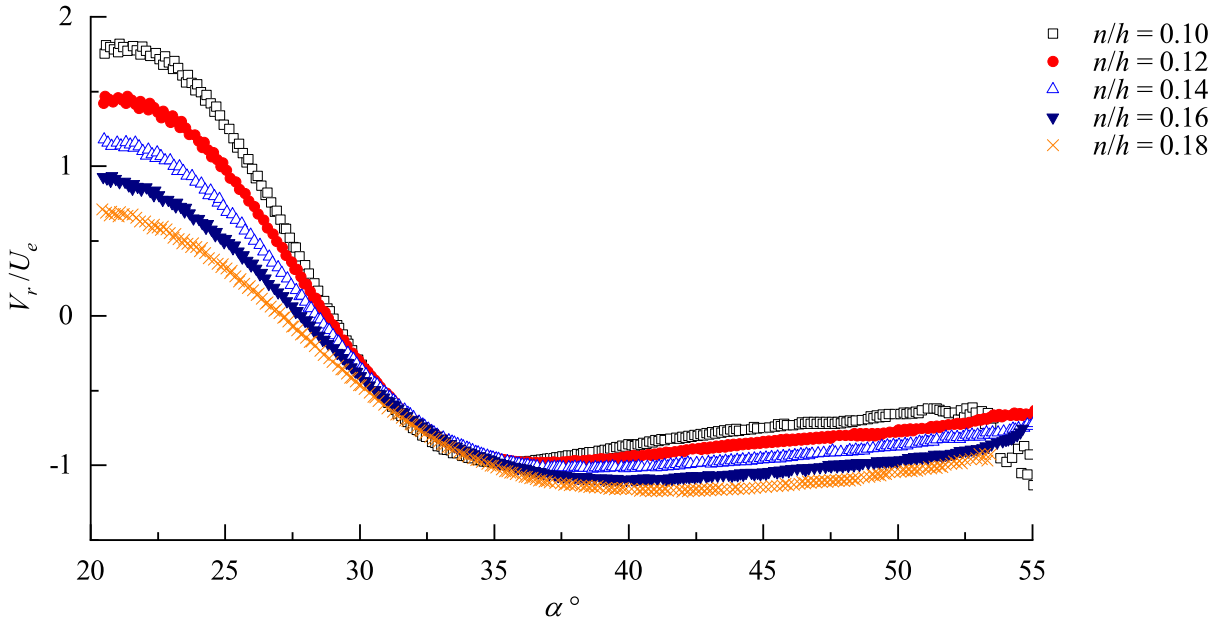

Figure 4.28. Plot of the normalized mean radial velocity against the circumferential position for several polar lines over the 30° modified spillway at $D_c/h = 0.4$.

Self-similarity is an important concept in the study of turbulent flows. Here, we present experimental evidence to demonstrate that the angular momentum in the vicinity of the recirculation zone may be expressed as the summation of a linear function and a self-similar function. Let us denote the quantities at the first and second intersection points of the angular momentum, as shown in Figure 4.28, by 'c' and 'l' subscripts, respectively. Hence, we obtain the line connecting the two intersection points, $g(\alpha)$, as follows:

$$g(\alpha) = \left(\frac{\alpha - \alpha_c}{\alpha_l - \alpha_c}\right)(L_l - L_c) + L_c \tag{4.20}$$

We define the residue function, $f(r, \alpha)$, as the subtraction of $g(\alpha)$ from the angular momentum, $L(r, \alpha)$:

$$f(r, \alpha) = L(r, \alpha) - g(\alpha) \tag{4.21}$$

The variations of the residue function, $f(r, \alpha)$, for several polar lines is provided in Figure 4.29.

Figure 4.29(b) shows the plot of the $f(r,\alpha)/f_{max}(r)$, where $f_{max}(r)$ is the maximum residue for $\alpha_c < \alpha < \alpha_l$.

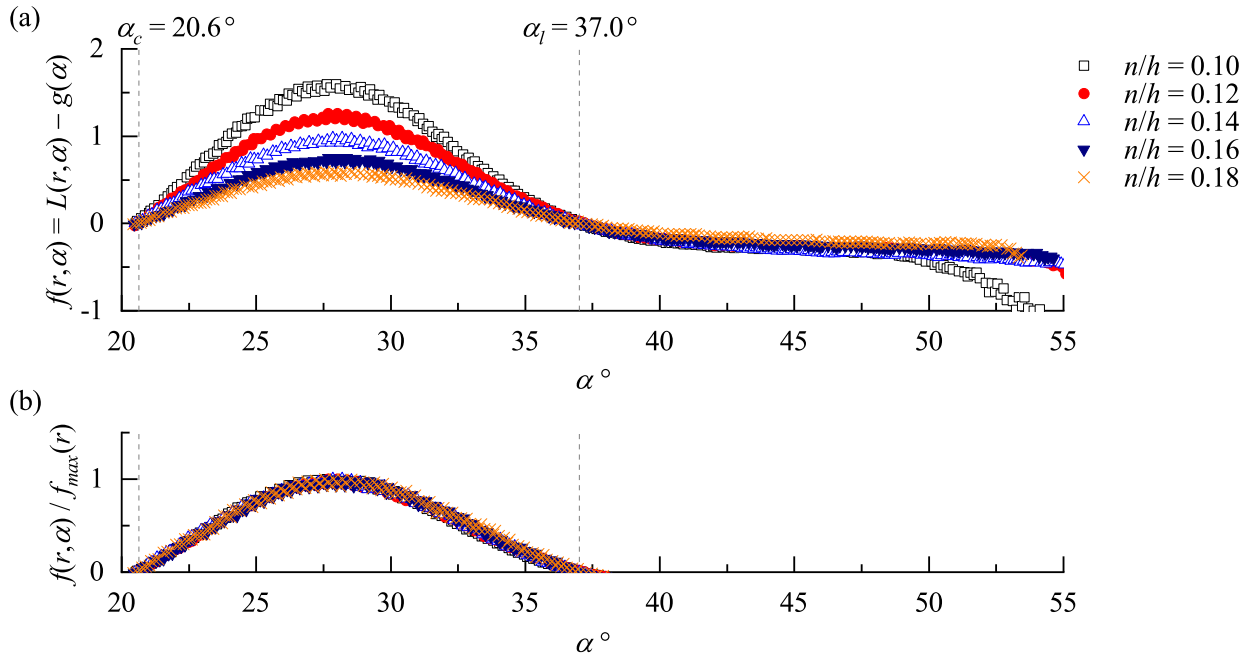

Figure 4.29. Similarity analysis of the angular momentum over the 30° modified spillway at $D_c/h = 0.4$.

The following important conclusions immediately follow from Figure 4.29:

1. The peak location of the residue function is not significantly affected by the normal distance from the wall.
2. Plots of $f(r,\alpha)/f_{max}(r)$ for the various polar lines almost collapse on the same curve, meaning that $f(r,\alpha)/f_{max}(r)$ is only a function of α.

Hence, the angular momentum in the vicinity of the recirculation bubble may be expressed by the following equation:

$$L(r,\alpha) = A\alpha + B + \zeta(r)\cdot h(\alpha) \tag{4.22}$$

$$A = \frac{L_l - L_c}{\alpha_l - \alpha_c} \qquad B = \frac{\alpha_l L_c - \alpha_c L_l}{\alpha_l - \alpha_c}$$

In equation (4.22), $\zeta(r)$ is a scale function and $h(\alpha)$ is the self-similar angular momentum residue, which are obtained experimentally. We remark that equation (4.22) is valid for all test cases, irrespective of the water depth over the crest or the upstream face inclination. Now if we solve equations (4.13), (4.14), and (4.22), we conclude:

$$\begin{aligned} V_r &= \zeta'(r) \int h(\alpha) d\alpha + q(r) \\ \frac{dr q(r)}{dr} + \frac{A}{r} &= -\left(h'(\alpha) \frac{\zeta(r)}{r} + \int h(\alpha) d\alpha \frac{dr\zeta'(r)}{dr} \right) \end{aligned} \tag{4.23}$$

The left-hand side of equation (4.23) only depends on r. Hence, the right-hand side cannot be a function of α, and consequently, the following equation must hold:

$$\begin{aligned} \left(\frac{w}{\pi}\right)^2 \frac{dh(\alpha)}{d\alpha} + \int h(\alpha) d\alpha &= C \\ \left(\frac{w}{\pi}\right)^2 h'' + h &= 0 \end{aligned} \tag{4.24}$$

When w^2 is a real number, the solution to equation (4.24) is the following oscillating function:

$$h(\alpha) = a \sin\left(\pi \frac{\alpha - \alpha_0}{w}\right) \tag{4.25}$$

The plot of predicted values by equation (4.25) and the experimental values is shown in Figure 4.30. Levenberg-Marquardt iteration algorithm was used and the coefficient of determination, R^2, was 0.985, indicating a good agreement between the fitted and experimental values.

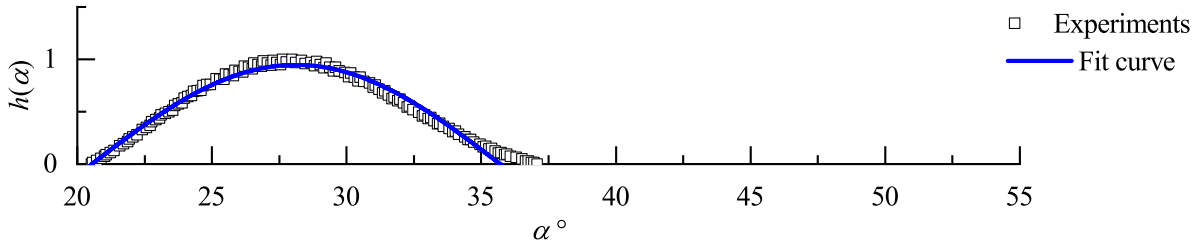

Figure 4.30. Comparison of the experimental data with the predicted values for the self-similar angular momentum residue, $h(\alpha)$, over the 30° modified spillway at $D_c/h = 0.4$.

Next, by substituting (4.24) in (4.23), we obtain the following Cauchy-Euler ODE for the scale function, $\zeta(r)$:

$$r^2\zeta'' + r\zeta' - \left(\frac{\pi}{w}\right)^2\zeta = 0 \tag{4.26}$$

Now, solving (4.26), the scale function, $\zeta(r)$, is as follows:

$$\zeta(r) = b\left(r^{\frac{-1+\sqrt{1+\frac{4\pi^2}{w^2}}}{2}}\right) + c\left(r^{\frac{-1-\sqrt{1+\frac{4\pi^2}{w^2}}}{2}}\right) \tag{4.27}$$

Equation (4.18), should be used with caution since for certain test cases, including all of $D_c/h = 0.6$ test cases and all $\theta = 90°$ test cases, the angular momentum profiles do not collapse on the same line even after the reattachment of the flow. We choose $D_c/h = 0.4$ and $\theta = 90°$ test case as a representative of all of these test conditions. Figure 4.31 shows the plot of the angular momentum, for several polar lines over the 90° standard spillway at $D_c/h = 0.4$.

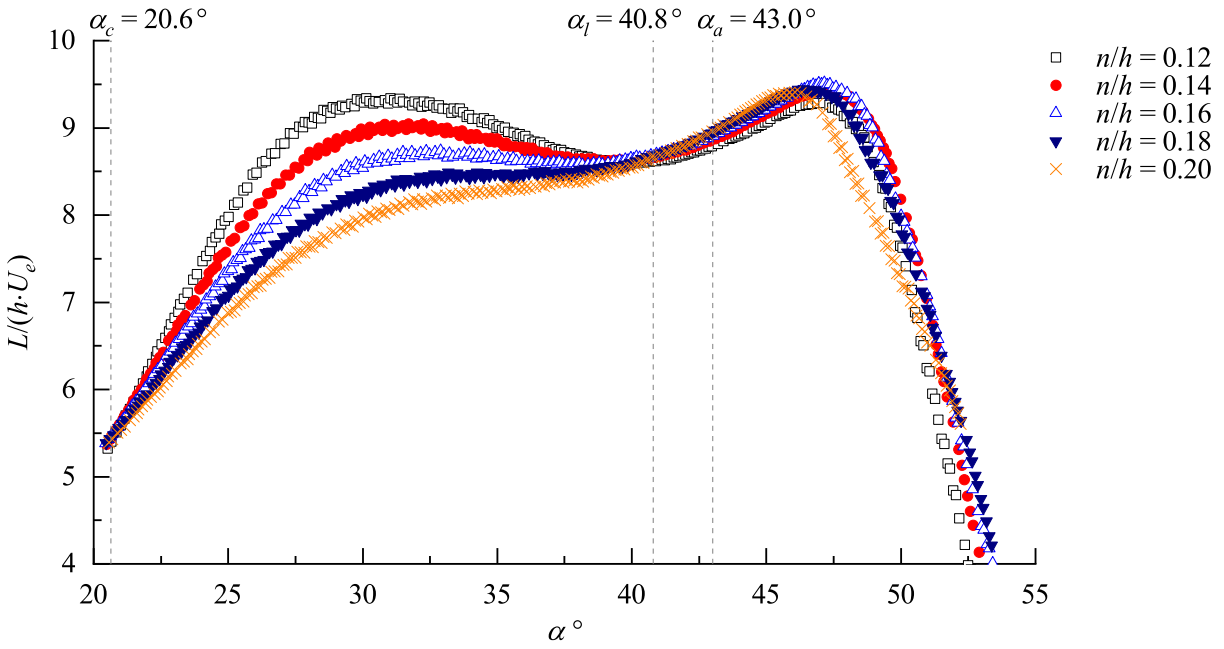

Figure 4.31. Plot of the normalized angular momentum against the circumferential position for several polar lines over the 90° standard spillway at $D_c/h = 0.4$.

Figure 4.31 confirms our latest statement. Still, the angular momentum varies linearly, that is:

$$\frac{\partial U_\alpha}{\partial \alpha} = f(r) \tag{4.28}$$

Now, solving equations (4.13), (4.14), and (4.28) altogether, we have:

$$\begin{aligned}
\frac{\partial U_\alpha}{\partial \alpha} = f(r) &\Rightarrow U_\alpha = f(r)\alpha + h(r) \\
\frac{\partial r V_r}{\partial r} = -\frac{\partial U_\alpha}{\partial \alpha} &\Rightarrow rV = -\int f(r)dr + g(\alpha) \\
\frac{\partial r U_\alpha}{\partial r} = \frac{\partial V_r}{\partial \alpha} &\Rightarrow \frac{dr f(r)}{dr}\alpha - \frac{dg(\alpha)}{r d\alpha} = -\frac{dr h(r)}{dr}
\end{aligned} \tag{4.29}$$

For equation (4.29) to be true for all values of r and α, the left-hand side cannot be a function of α, meaning that both sides must depend on r only. To satisfy this condition, $g(\alpha)$ must be of the following form:

$$g(\alpha) = \frac{D}{2}\alpha^2 + E\alpha + C \tag{4.30}$$

From equation (4.29), it then immediately follows that:

$$\alpha\left(\frac{dr f(r)}{dr} - \frac{D}{r}\right) + \left(\frac{dr h(r)}{dr} - \frac{E}{r}\right) = 0 \tag{4.31}$$

Now, since both terms within the parentheses must be zero, we obtain:

$$f = \frac{D\ln r + A}{r} \tag{4.32}$$

$$h = \frac{E\ln r + B}{r} \tag{4.33}$$

$$L = A\alpha + B + \ln r(D\alpha + E) \tag{4.34}$$

$$U_\alpha = \frac{A\alpha + B}{r} + \frac{\ln r}{r}(D\alpha + E) \tag{4.35}$$

$$V_r = \frac{-A\ln r + C}{r} + \frac{D}{2}\left(\frac{\alpha^2 - \ln^2 r}{r}\right) + E\frac{\alpha}{r} \tag{4.36}$$

In equations (4.32)-(4.36), A, B, C, D, and E are experimental constants. Comparing equation

(4.34) with equation (4.16), it is evident that the new term $\ln r(D\alpha + E)$ is added to the angular momentum. Equations (4.34), (4.35), and (4.36) can be used for all test cases regardless of the water depth and upstream face inclination. For the test cases, where D and E are negligible, equation (4.34) is simply reduced to the former equation (4.16). Alternatively, one may set only D to zero, which allows V_r to vary linearly in the circumferential direction. There is also an interesting analogy between equation (4.34) and equation (4.22), that is, $L - (A\alpha + B)$ is the product of a scale function of r and a self-similar function of α.

5. Conclusions and Recommendations for Future Work

5.1. Summary and conclusions

The effects of upstream face inclination and water depth on flow characteristics upstream and over a sharp-crested spillway model were experimentally examined using a planar particle image velocimetry system. Three upstream face inclinations, including $\theta = 90°$, $45°$,and $30°$, were investigated. To obtain a variety of hydraulic conditions, each upstream face inclination was tested for three water depths, namely, $D_c/h = 0.7$, 0.4, and 0.2. The results were discussed in terms of both contours and one-dimensional profiles of time-averaged quantities, such as the mean velocities, mean streamlines, mean accelerations, mean span-wise vorticity, Reynolds stresses, turbulent kinetic energy, budget terms of the TKE equation, and two-point correlations.

Contours of the normalized mean velocities revealed that both the mean stream-wise velocity and the mean vertical velocity increase significantly as the flow approaches the spillway. The former was due to the reduction in flow cross-sectional area, while the latter was attributed to the upward deflection of the flow. For the $90°$ standard spillway, the oncoming flow was separated from the channel floor while for the $45°$ and $30°$ modified spillways, the induced favorable pressure gradient completely suppressed the flow separation.

The mean streamlines showed the presence of a recirculation bubble near the heel of the $90°$ standard spillway at the lowest water depth, $D_c/h = 0.2$. It was concluded that the size of the recirculation bubble decreases as the water depth increases. It is recommended to operate spillways at high enough water depths to prevent the formation of any recirculation zones that may trap fish and compromise the downstream passage efficiency. It was also observed that the oncoming flow impinges on the upstream face of the $90°$ standard spillway, causing large normal velocities relative to the upstream face of the spillway, increasing the risk of injury and the mortality rate. For the $45°$ and $30°$ modified spillways, on the other hand, the corresponding normal velocities were smaller, providing a safer environment for the downstream migration of fish.

Contours of the normalized mean stream-wise and vertical accelerations indicated a more

uniform distribution of acceleration along the upstream face of the 45° and 30° modified spillways compared to the 90° standard spillway, which suggests a more suitable hydraulic condition for downstream migrants, especially rheophilic species, which in several cases have demonstrated avoidance behavior to rapidly accelerating flows.

Contours of the normalized Reynolds stresses and turbulent kinetic energy showed higher turbulence levels along the upstream face of the 90° standard spillway compared to the 45° and 30° modified spillways, which were a consequence of flow separation and instabilities. It was concluded that decreasing the upstream face inclination may improve the downstream migration of fish by allowing fish to exploit the water column near the spillway and rest before swimming through high velocity and high accelerating flows.

Budget terms of the turbulent kinetic energy equation demonstrated high values of convection over the spillway, where the velocities were rather larger. For all test cases, elevated regions of production and diffusion were observed close to the crest of the spillway, which was attributed to the perturbations caused by the sharp crest or the separated shear layer in case of the 90° standard spillway. In addition, production levels were relatively higher near the heel of the of the 45° and 30° modified spillways. It was observed that molecular diffusion is at least two orders of magnitude smaller than the turbulence transport. The dissipation rate was significant in particular regions and may not be ignored.

Contours of the two-point correlations were analyzed to understand the effects of the water depth and upstream face inclination on the size and orientation of the large-scale eddies. For all test cases, at the selected locations, the size of the eddies decreases as the water depth decreases. For the 90° standard spillway, the size of the turbulence structures increased in the stream-wise direction, whereas for the 45° and 30° modified spillways, the size of the structures decreased as the flow approached the spillway. It was also observed that the size of the turbulent structures along the upstream face of the spillway decreases as the upstream face inclination decreases. For the 45° and 30° modified spillways, the structures were stretched along the upstream face of the spillway

irrespective of water depth, whereas for the 90° standard spillway, the topology of the structures were dependent on the water depth.

Profiles of the frequency spectra density at selected locations upstream and over the crest of the spillways were plotted to analyze the effects of the water depth on the periodicity of the eddies and examine the dominant low- and high-frequency motions. At the upstream location, the inertial subrange was relatively wider and followed the $-5/3$ line well. The profiles upstream of the spillway were independent of the water depth, except in the low-frequency region. Over the spillway, on the other hand, the profiles were dependent on the water depth. The dominant low and high frequencies did not vary significantly with water depth at the selected locations. Nonetheless, the inertial subrange was wider and more distinct at the lower water depths.

Over the spillway the flow was separated by the crest and a recirculation bubble was observed near the crest, whose size decreases as the water depth decreases. The separated flow reattached over the spillway and a wall-jet boundary layer evolved over the convex surface of the spillway. The angular momentum was examined along the surface of the spillway and semi-experimental relations were obtained to characterize the mean flow in the vicinity of the recirculation zone. The flow in the vicinity of the free surface was also investigated where it was concluded that the mean span-wise vorticity only varies in the stream-wise direction, that is, the flow was in rigid-body rotation.

5.2. Recommendations for future works

In this section, recommendations are suggested for future research toward a better understanding of the hydraulic conditions of spillways. It is apparent from previous discussions that although concerted research efforts have been made over the past decades to provide a better understanding of the hydraulic environment generated by spillways, still the available knowledge on the relationship between a variety of hydraulic characteristics, such as accelerations and Reynolds stresses, and the downstream passage of fish is very limited since time-resolved whole-field measurements were not feasible up until recently and it was impossible for researchers to derive all of the flow characteristics

required to fully understand the complex turbulence field induced by spillways. The present study provided valuable information on the distribution of the stream-wise and vertical velocities, stream-wise and vertical accelerations, and three out of the six components of the Reynolds stress tensor. However, the turbulent kinetic energy could not be measured due to lack of span-wise velocity measurements, which is a limitation of the two-component planar PIV. Future investigations may take advantage of one of the most advanced flow measurement technologies, the stereoscopic PIV, to measure all three velocity components, which will provide the complete Reynolds stress tensor, all triple velocity correlations, and evaluation of the TKE without any approximation.

While experimental fluids mechanics remains a powerful tool in the study of complex turbulent flows imposed by spillways, the design of optimal spillways by means of physical experiments alone is challenging due to the high cost and time required to setup and perform measurements for a large number of model configurations. Computational fluid dynamics (CFD) techniques based on the Reynolds averaged Navier Stokes (RANS) equations, on the other hand, are relatively less expensive and less time consuming. With this type of numerical technique, complex three-dimensional flows may be explored more easily and quickly than is possible in physical experiments. However, turbulence closure numerical models are required to explicitly account for the effects of all turbulence scales on the mean flow. Furthermore, it is impossible to formulate a universal turbulence model that could predicts all turbulent flows with sufficient accuracy. This complicates the design of spillway systems using RANS modeling. A reasonable approach for future works is to use the measurements provided in this research to select appropriate turbulence numerical models and refine the model constants, that is, the benchmark experimental datasets can be used to validate the numerical results.

References

Albayrak, I., Boes, R. M., Kriewitz-Byun, C. R., Peter, A., and Tullis, B. P. (2020). Fish guidance structures: hydraulic performance and fish guidance efficiencies. *Journal of Ecohydraulics*, 5(2):113–131.

Amaral, S. D., Quaresma, A. L., Branco, P., Romão, F., Katopodis, C., Ferreira, M. T., Pinheiro, A. N., and Santos, J. M. (2019). Assessment of retrofitted ramped weirs to improve passage of potamodromous fish. *Water*, 11(12):2441.

Amaral, S. V. (2003). *The use of angled bar racks and louvers for guiding fish at FERC-Licensed projects. FERC Fish Passage Workshop*. Alden Research Laboratory, Inc.

Arnekleiv, J. V., Kraabøl, M., and Museth, J. (2007). Efforts to aid downstream migrating brown trout (salmo trutta l.) kelts and smolts passing a hydroelectric dam and a spillway. In *Developments in Fish Telemetry*, pages 5–15. Springer.

Bates, D. W. and Jewett Jr, S. G. (1961). Louver efficiency in deflecting downstream migrant steelhead. *Transactions of the American Fisheries Society*, 90(3):336–337.

Bates, D. W. and Vinsonhaler, R. (1957). Use of louvers for guiding fish. *Transactions of the American Fisheries Society*, 86(1):38–57.

Bell, M. and DeLacy, A. (1972). A compendium on the survival of fish passing through spillways and conduits. fisheries engineering research program. *US Army Engineers Division, North Pacific Corps of Engineers, Portland Oregon*.

Bendat, J. S. and Piersol, A. G. (2011). *Random data: analysis and measurement procedures*. John Wiley & Sons.

Brett, J. R. and Alderdice, D. F. (1958). *Research on guiding young salmon at two British Columbia field stations.* Fisheries Research Board of Canada.

Brett, J. R. and MacKinnon, D. (1953). Preliminary experiments using lights and bubbles to deflect migrating young spring salmon. *Journal of the Fisheries Board of Canada*, 10(8):548–559.

Brown, R. S., Colotelo, A. H., Pflugrath, B. D., Boys, C. A., Baumgartner, L. J., Deng, Z. D., Silva, L. G., Brauner, C. J., Mallen-Cooper, M., Phonekhampeng, O., Thorncraft, G., and Singhanouvong, D. (2014). Understanding barotrauma in fish passing hydro structures: a global strategy for sustainable development of water resources. *Fisheries*, 39(3):108–122.

Burner, C. J. and Moore, H. L. (1953). Attempts to guide small fish with underwater sound. Technical report, Special Scientific Report.

Čada, G. F. (2001). The development of advanced hydroelectric turbines to improve fish passage survival. *Fisheries*, 26(9):14–23.

Calles, O., Karlsson, S., Vezza, P., Comoglio, C., and Tielman, J. (2013). Success of a low-sloping rack for improving downstream passage of silver eels at a hydroelectric plant. *Freshwater Biology*, 58(10):2168–2179.

Castro-Santos, T., Cotel, A., and Webb, P. W. (2009). Fishway evaluations for better bioengineering: an integrative approach. *American Fisheries Society Symposium*, 69:557–575.

Cote, A. J. and Webb, P. W. (2015). Living in a turbulent world-a new conceptual framework for the interactions of fish and eddies. *Integrative and Comparative Biology*, 55(4):662–672.

Coutant, C. C. (2001). Integrated, multi-sensory, behavioral guidance systems for fish diversions. *American Fisheries Society Symposium*, pages 105–113, Bethesda, MD.

Coutant, C. C. and Whitney, R. R. (2000). Fish behavior in relation to passage through hydropower turbines: a review. *Transactions of the American Fisheries Society*, 129(2):351–380.

Denil, G. (1909). Les échelles à poissons et leur application aux barrage de meuse et d'ourthe. *Annales des Travaux Publics de Belgique, Bruxelles, Belgique*.

Denil, G. (1938). La mécanique du poisson de rivière. *Annales des Travaux Publics de Belgique, Bruxelles, Belgique*.

Duguay, J., Foster, B., Lacey, J., and Castro-Santos, T. (2018). Sediment infilling benefits rainbow trout passage in a baffled channel. *Ecological Engineering*, 125:38–49.

DWA (2005). *Fish Protection Technologies and Downstream Fishways. Dimensioning, Design, Effectiveness Inspection*. German Association for Water, Wastewater and Waste (DWA) Hennef.

Euston, E. T., Royer, D. D., and Simons, C. L. (1998). American eels and hydro plants: clues to eel passage. *Hydro Review*, 1998:94–103.

Ferguson, J., Poe, T., and Carlson, T. (1998). Surface-oriented bypass systems for juvenile salmonids on the columbia river, USA. In Jungwirth, M., Schmutz, S., and Weiss, S., editors, *Migration and Fish Bypasses*, pages 281–299. Fishing News Books.

Ferguson, J. W., Matthews, G. M., McComas, R. L., Absolon, R. F., Brege, D. A., Gessel, M. H., and Gilbreath, L. G. (2005). *Passage of adult and juvenile salmonids through federal Columbia River power system dams*. NOAA Technical Memorandums.

Ferguson, J. W., Sandford, B. P., Reagan, R. E., Gilbreath, L. G., Meyer, E. B., Ledgerwood, R. D., and Adams, N. S. (2007). Bypass system modification at bonneville dam on the columbia river improved the survival of juvenile salmon. *Transactions of the American Fisheries Society*, 136(6):1487–1510.

Fields, P. E. (1957). Guiding migrant salmon. *The Scientific Monthly*, 85(1):10–22.

Finnemore, E. J. and Franzini, J. B. (2002). *Fluid mechanics with engineering applications*. McGraw-Hill.

García, A., Jorde, K., Habit, E., Caamaño, D., and Parra, O. (2011). Downstream environmental effects of dam operations: changes in habitat quality for native fish species. *River Research and Applications*, 27(3):312–327.

Hadderingh, R. H. and Bakker, H. (1998). Fish mortality due to passage through hydroelectric power stations on the meuse and vecht rivers. In *Fish migration and fish bypasses.*, pages 315–328.

Hadderingh, R. H., Van Der Stoep, J. W., and Hagraken, J. M. (1992). Deflecting eels from water inlets of power stations with light. *Irish Fish. Invest*, 36:37–41.

Haro, A., Odeh, M., Noreika, J., and Castro-Santos, T. (1998). Effect of water acceleration on downstream migratory behavior and passage of atlantic salmon smolts and juvenile american shad at surface bypasses. *Transactions of the American Fisheries Society*, 127(1):118–127.

Johnson, G. E. and Dauble, D. D. (2006). Surface flow outlets to protect juvenile salmonids passing through hydropower dams. *Reviews in Fisheries Science*, 14(3):213–244.

Katopodis, C. (1992). *Introduction to fishway design*. Freshwater Institute, Central and Arctic Region, Department of Fisheries and Oceans.

Katopodis, C. (2005). Developing a toolkit for fish passage, ecological flow management and fish habitat works. *Journal of Hydraulic Research*, 43(5):451–467.

Katopodis, C. and Aadland, L. (2006). Effective dam removal and river channel restoration approaches. *International Journal of River Basin Management*, 4(3):153–168.

Katopodis, C. and Gervais, R. (2016). *Fish swimming performance database and analyses*. Canadian Science Advisory Secretariat (CSAS).

Katopodis, C., Lemke, D., and Ghamry, H. K. (2011). Ecohydraulic studies on bar racks (trashracks). *Report for Manitoba Hydro and Fisheries and Oceans Canada (DFO)*, 3.

Katopodis, C., Rajaratnam, N., Wu, S., and Tovell, D. (1997). Denil fishways of varying geometry. *Journal of Hydraulic Engineering*, 123(7):624–631.

Katopodis, C. and Williams, J. G. (2012). The development of fish passage research in a historical context. *Ecological Engineering*, 48:8–18.

Lacey, R. J., Neary, V. S., Liao, J. C., Enders, E. C., and Tritico, H. M. (2012). The ipos framework: linking fish swimming performance in altered flows from laboratory experiments to rivers. *River Research and Applications*, 28(4):429–443.

Larinier, M. (1992). Les passes à ralentisseurs. *Bulletin Français de la Pêche et de la Pisciculture*, (326-327):73–94.

Larinier, M. (2008). Fish passage experience at small-scale hydro-electric power plants in france. *Hydrobiologia*, 609(1):97–108.

Larinier, M. and Travade, F. (2002). Downstream migration: problems and facilities. *Bulletin Français de la Pêche et de la Pisciculture*, (364):181–207.

Li, M., Shi, X., Jin, Z., Ke, S., Lin, C., An, R., Li, J., and Katopodis, C. (2021). Behaviour and ability of a cyprinid (schizopygopsis younghusbandi) to cope with accelerating flows when migrating downstream. *River Research and Applications*, 37(8):1168–1179.

Lupandin, A. (2005). Effect of flow turbulence on swimming speed of fish. *Biology Bulletin*, 32(5):461–466.

Mitchell, C. P. (1995). Fish passage problems in New Zealand. In *Proceedings of the International Symposium on Fishways.*, pages 33–41.

Monan, G. E., Pugh, J. R., and Smith, J. R. (1967). Efficiency of a combined electrode and louver array in guiding juvenile steelhead trout (salmo gairdneri). *Transactions of the American Fisheries Society*, 96(4):422–423.

Montén, E. (1985). *Fish and turbines: fish injuries during passage through power station turbines*. Norstedts Tryckeri.

Pugh, J. R., Monan, G. E., and Smith, J. R. (1970). Effect of water velocity on the fish guiding efficiency of an electrical guiding system. *Fishery Bulletin*, 68(2):307–324.

Richkus, W. A. and Dixon, D. A. (2002). *Review of research and technologies on passage and protection of downstream migrating catadromous eels at hydroelectric facilities*. Biology, management, and protection of catadromous eels.

Ruggles, C. P. (1980). *A review of the downstream migration of Atlantic salmon*. Department of Fisheries and Oceans Canada.

Ruggles, C. P. and Murray, D. G. (1983). *A review of fish response to spillways*. Freshwater and Anadromous Division, Resource Branch, Dept. of Fisheries and Oceans.

Ruggles, C. P. and Ryan, P. (1964). An investigation of louvers as a method of guiding juvenile pacific salmon. *The Canadian Fish Culturist*, 33:1–68.

Samimy, M. and Lele, S. K. (1991). Motion of particles with inertia in a compressible free shear layer. *Physics of Fluids A: Fluid Dynamics*, 3(8):1915–1923.

Santos, J. M., Silva, A., Katopodis, C., Pinheiro, P., Pinheiro, A., Bochechas, J., and Ferreira, M. T. (2012). Ecohydraulics of pool-type fishways: getting past the barriers. *Ecological Engineering*, 48:38–50.

Savage, B. M. and Johnson, M. C. (2001). Flow over ogee spillway: Physical and numerical model case study. *Journal of hydraulic engineering*, 127(8):640–649.

Schwevers, U. and Adam, B. (2020). *Fish protection technologies and fish ways for downstream migration*. Springer.

Sciacchitano, A. and Wieneke, B. (2016). Piv uncertainty propagation. *Measurement Science and Technology*, 27(8):084006.

Scruton, D., McKinley, R., Kouwen, N., Eddy, W., and Booth, R. (2003). Improvement and optimization of fish guidance efficiency (fge) at a behavioural fish protection system for downstream migrating atlantic salmon (salmo salar) smolts. *River Research and Applications*, 19(5-6):605–617.

Shahabi, M., Ghomeshi, M., Ahadiyan, J., Mohammadian, T., and Katopodis, C. (2021). Do fishways stress fish? assessment of physiological and hydraulic parameters of rainbow trout navigating a novel w-weir fishway. *Ecological Engineering*, 169:106330.

Silva, A., Santos, J., Ferreira, M., Pinheiro, A., and Katopodis, C. (2012a). Passage efficiency of offset and straight orifices for upstream movements of iberian barbel in a pool-type fishway. *River Research and Applications*, 28(5):529–542.

Silva, A. T., Bærum, K. M., Hedger, R. D., Baktoft, H., Fjeldstad, H.-P., Gjelland, K. Ø., Økland, F., and Forseth, T. (2020). The effects of hydrodynamics on the three-dimensional downstream migratory movement of atlantic salmon. *Science of the Total Environment*, 705:135773.

Silva, A. T., Katopodis, C., Santos, J. M., Ferreira, M. T., and Pinheiro, A. N. (2012b). Cyprinid swimming behaviour in response to turbulent flow. *Ecological Engineering*, 44:314–328.

Silva, A. T., Katopodis, C., Tachie, M. F., Santos, J. M., and Ferreira, M. T. (2015). Downstream swimming behaviour of catadromous and potamodromous fish over spillways. *River Research and Applications*, 32(5):935–945.

Silva, A. T., Santos, J. M., Ferreira, M. T., Pinheiro, A. N., and Katopodis, C. (2011). Effects of water velocity and turbulence on the behaviour of iberian barbel (*Luciobarbus bocagei*, steindachner 1864) in an experimental pool-type fishway. *River Research and Applications*, 27(3):360–373.

Sonny, D., Knudsen, F. R., Enger, P. S., Kvernstuen, T., and Sand, O. (2006). Reactions of cyprinids to infrasound in a lake and at the cooling water inlet of a nuclear power plant. *Journal of Fish Biology*, 69(3):735–748.

Tarrade, L., Texier, A., David, L., and Larinier, M. (2008). Topologies and measurements of turbulent flow in vertical slot fishways. *Hydrobiologia*, 609(1):177–188.

Travade, F., Larinier, M., Subra, S., Gomes, P., and De-Oliveira, E. (2010). Behaviour and passage of european silver eels (anguilla anguilla) at a small hydropower plant during their downstream migration. *Knowledge and Management of Aquatic Ecosystems*, (398):01.

Tritico, H. M. and Cotel, A. J. (2010). The effects of turbulent eddies on the stability and critical swimming speed of creek chub (semotilus atromaculatus). *Journal of experimental biology*, 213(13):2284–2293.

Tsikata, J. M., Katopodis, C., and Tachie, M. F. (2009a). Experimental study of turbulent flow near model trashracks. *Journal of Hydraulic Research*, 47(2):275–280.

Tsikata, J. M., Tachie, M. F., and Katopodis, C. (2009b). Particle image velocimetry study of flow near trashrack models. *Journal of Hydraulic Engineering*, 135(8):671–684.

United States Army Corps of Engineers (USACE) (1988). *Hydraulic design criteria*. Mississippi, USA.

United States Bureau of Reclamation (1987). *Design of small dams*. US Department of the Interior, Bureau of Reclamation.

Vanderwalker, J. G. (1970). Responses of fingerling coho and chinook salmon to modified flows in a simulated turbine intake. *Transactions of the American Fisheries Society*, 99(3):532–539.

Verbiest, H., Breukelaar, A., Ovidio, M., Philippart, J.-C., and Belpaire, C. (2012). Escapement success and patterns of downstream migration of female silver eel anguilla anguilla in the river meuse. *Ecology of Freshwater Fish*, 21(3):395–403.

Verreault, G. and Dumont, P. (2003). An estimation of american eel escapement from the upper st. lawrence river and lake ontario in 1996 and 1997. In *American Fisheries Society Symposium*, volume 2003, pages 243–251.

Wilkes, M. A., Mckenzie, M., and Webb, J. A. (2018). Fish passage design for sustainable hydropower in the temperate southern hemisphere: an evidence review. *Reviews in Fish Biology and Fisheries*, 28(1):117–135.

Williams, J. G., Armstrong, G., Katopodis, C., Larinier, M., and Travade, F. (2012). Thinking like a fish: a key ingredient for development of effective fish passage facilities at river obstructions. *River Research and Applications*, 28(4):407–417.

Zhong, Y. and Power, G. (1996). Environmental impacts of hydroelectric projects on fish resources in china. *Regulated Rivers: Research & Management*, 12(1):81–98.

Appendix

One-dimensional profiles of the mean velocities, Reynolds stresses, and turbulent kinetic energy are presented in this section. While contours of these statistics were presented in the thesis, one-dimensional profiles are better suited for characterising the flow upstream of the spillways.

The profiles at six successive stream-wise locations, $x/h = -1.75, -1.25, -0.75, -0.50, -0.25$ and -0.05, were staggered relative to one another to better visualize the stream-wise evolution of the flow characteristics. The profiles for different upstream face slopes were then superimposed on top of each other to show the effects of the upstream face slope. For each test case, the range of the vertical axis is limited to $1 + D_c/h$. Moreover, since the upstream face of the 45° and 30° modified spillway stretches from $x/h = 0$ to $x/h = -\cot(\theta)$. In this region, the profiles start at $y/h = 1 + \tan(\theta) \times x/h$ instead of zero.

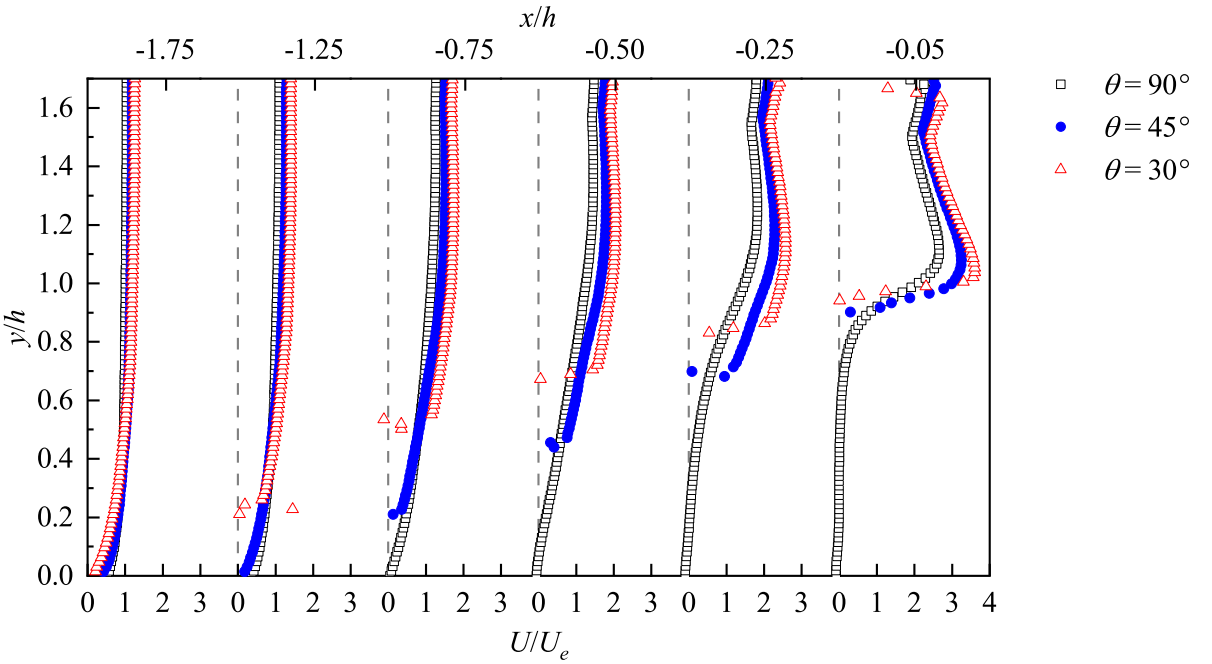

Figure A.1. Stream-wise evolution of the normalized mean stream-wise velocity profiles for different upstream face inclinations at $D_c/h = 0.7$.

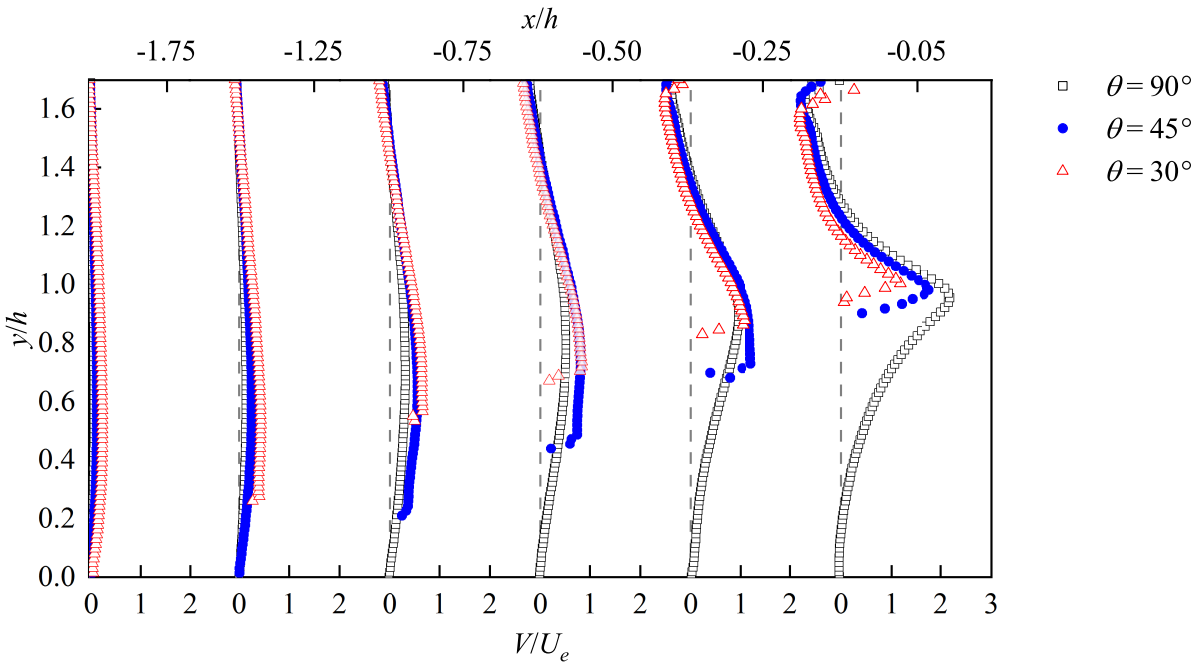

Figure A.2. Stream-wise evolution of the normalized mean vertical velocity profiles for different upstream face inclinations at $D_c/h = 0.7$.

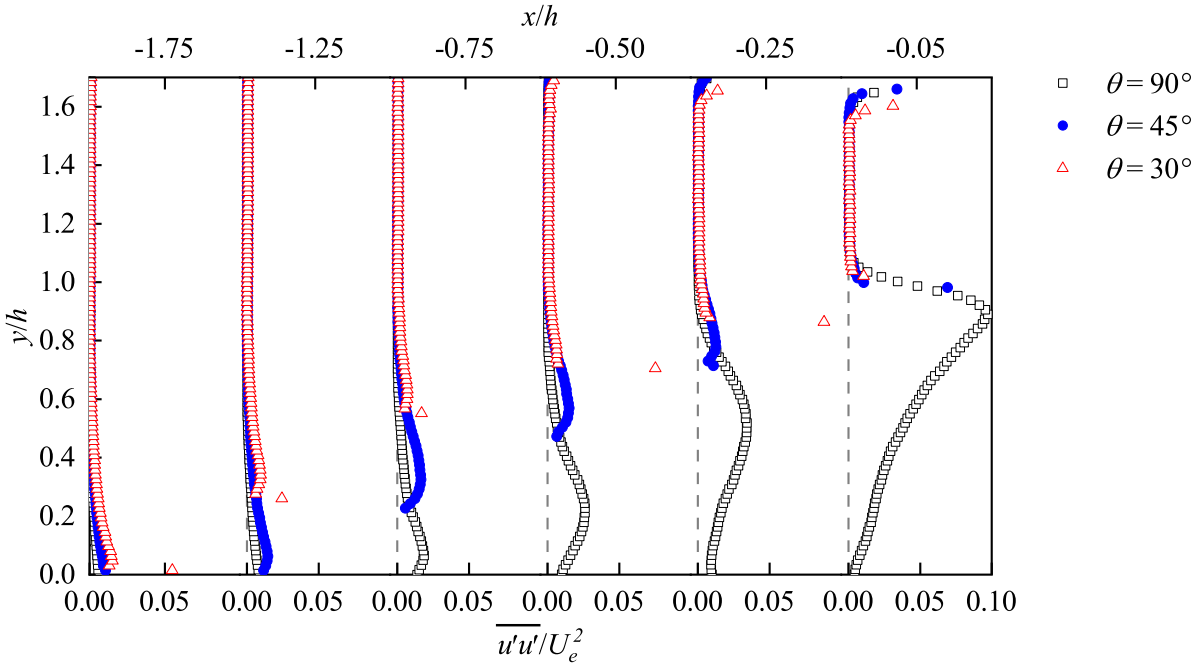

Figure A.3. Stream-wise evolution of the normalized stream-wise Reynolds normal stress profiles for different upstream face inclinations at $D_c/h = 0.7$.

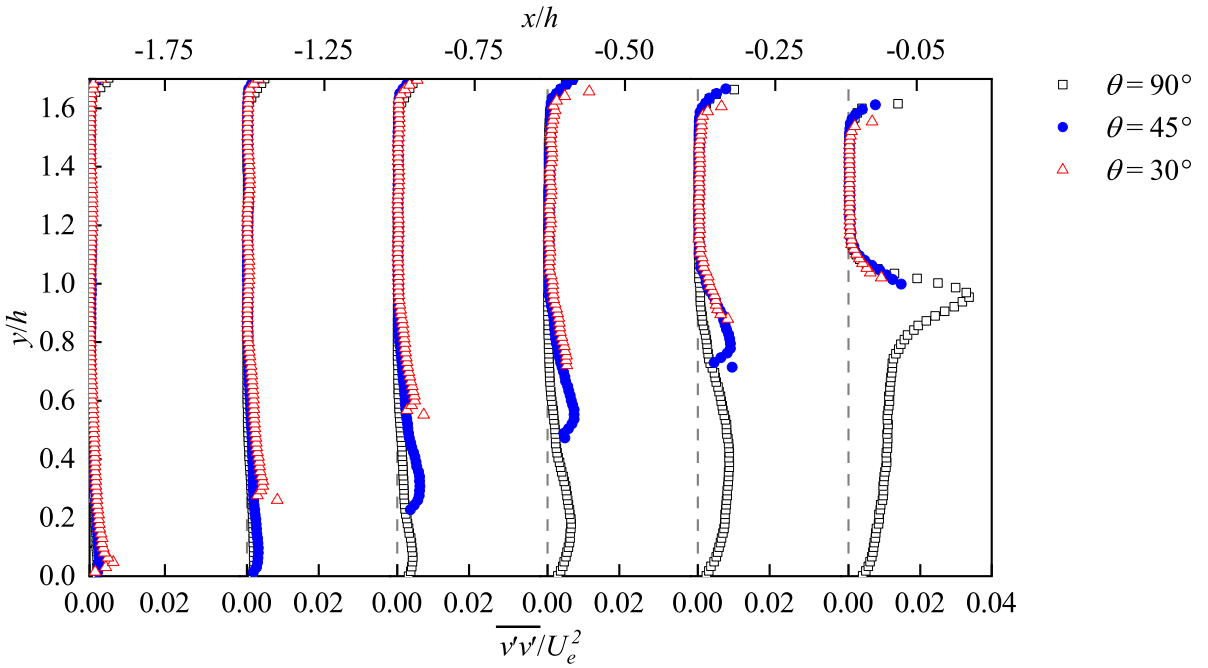

Figure A.4. Stream-wise evolution of the normalized vertical Reynolds normal stress profiles for different upstream face inclinations at $D_c/h = 0.7$.

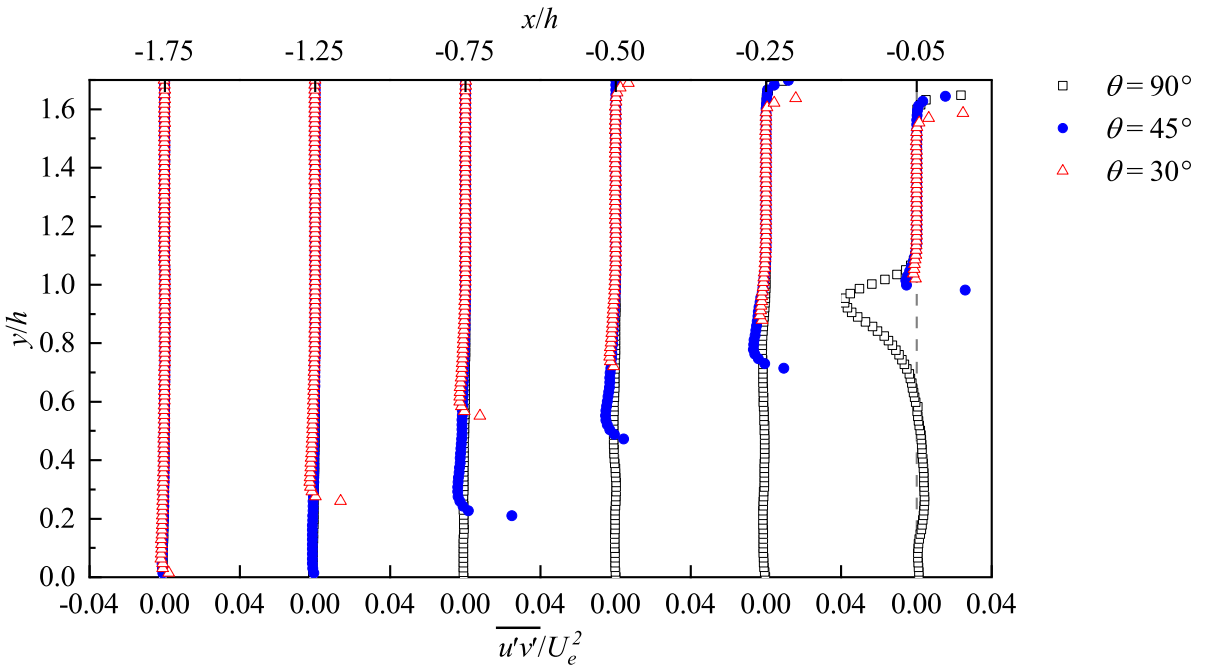

Figure A.5. Stream-wise evolution of the normalized Reynolds shear stress profiles for different upstream face inclinations at $D_c/h = 0.7$.

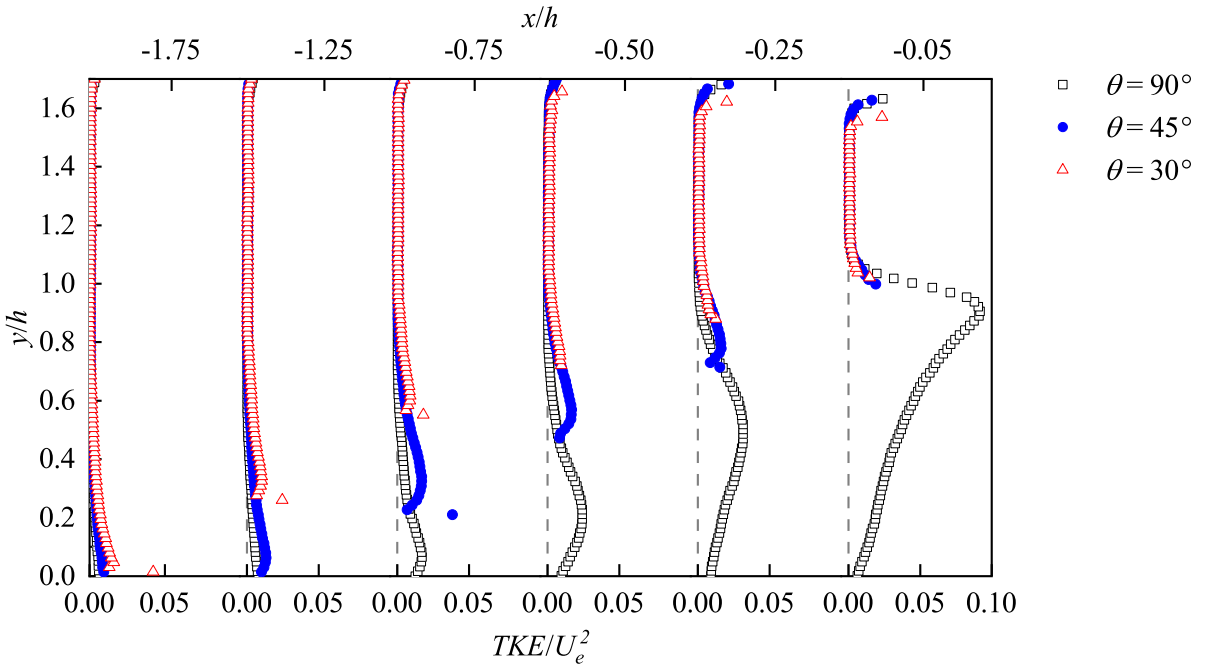

Figure A.6. Stream-wise evolution of the normalized TKE profiles for different upstream face inclinations at $D_c/h = 0.7$.

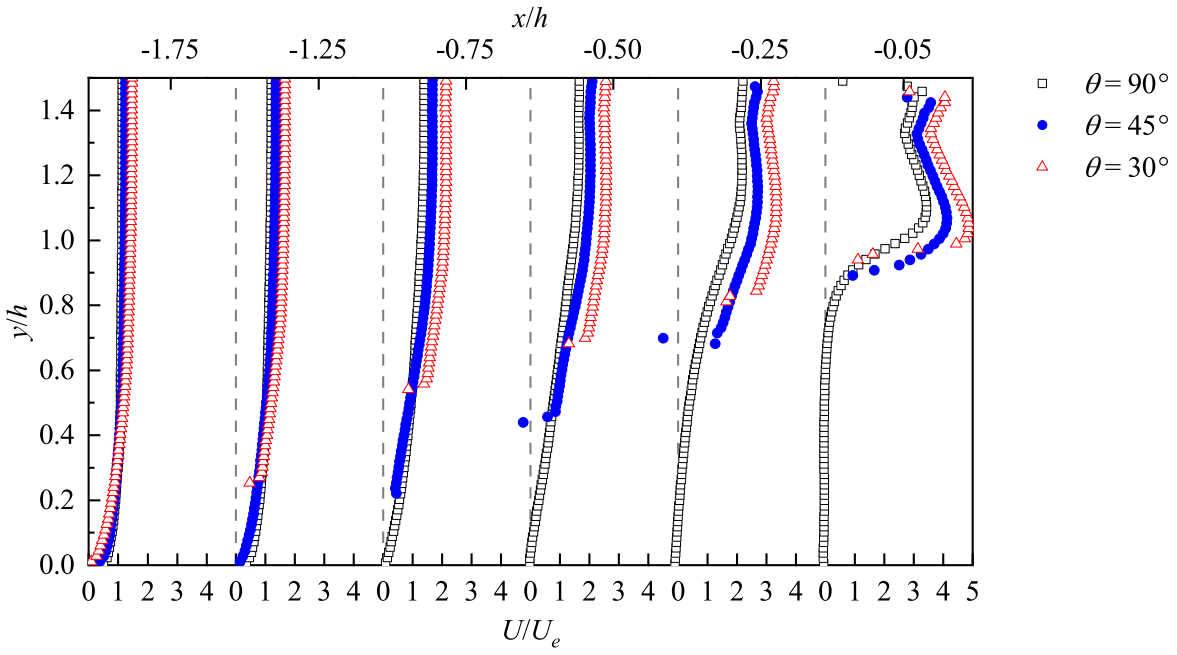

Figure A.7. Stream-wise evolution of the normalized mean stream-wise velocity profiles for different upstream face inclinations at $D_c/h = 0.4$.

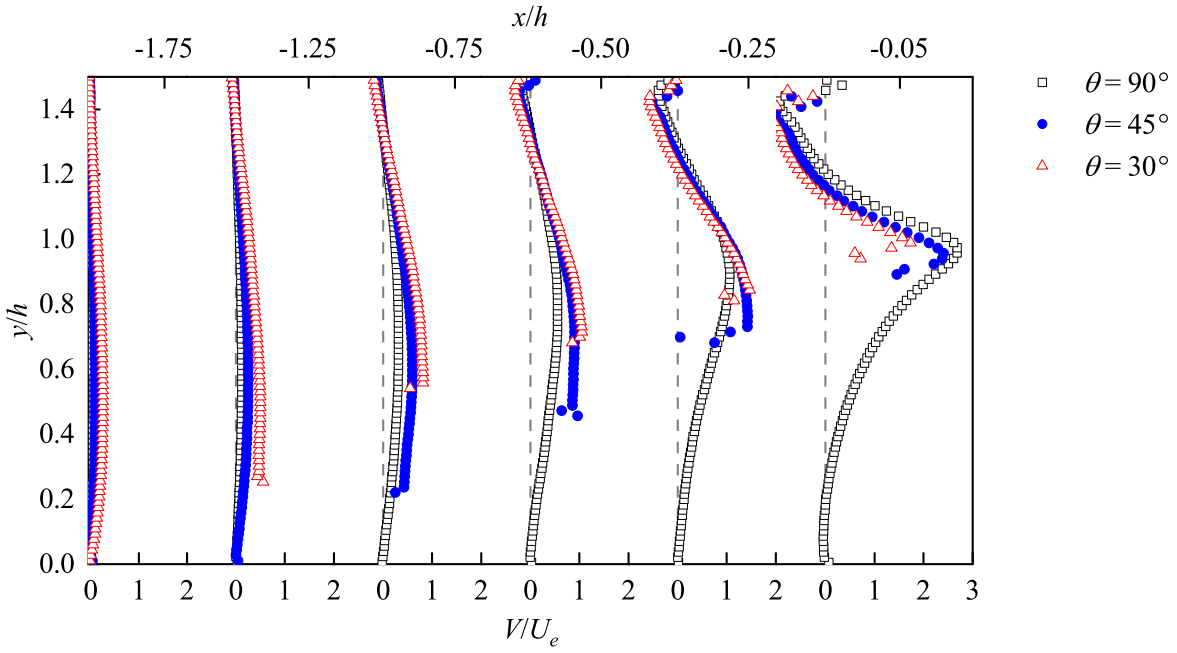

Figure A.8. Stream-wise evolution of the normalized mean vertical velocity profiles for different upstream face inclinations at $D_c/h = 0.4$.

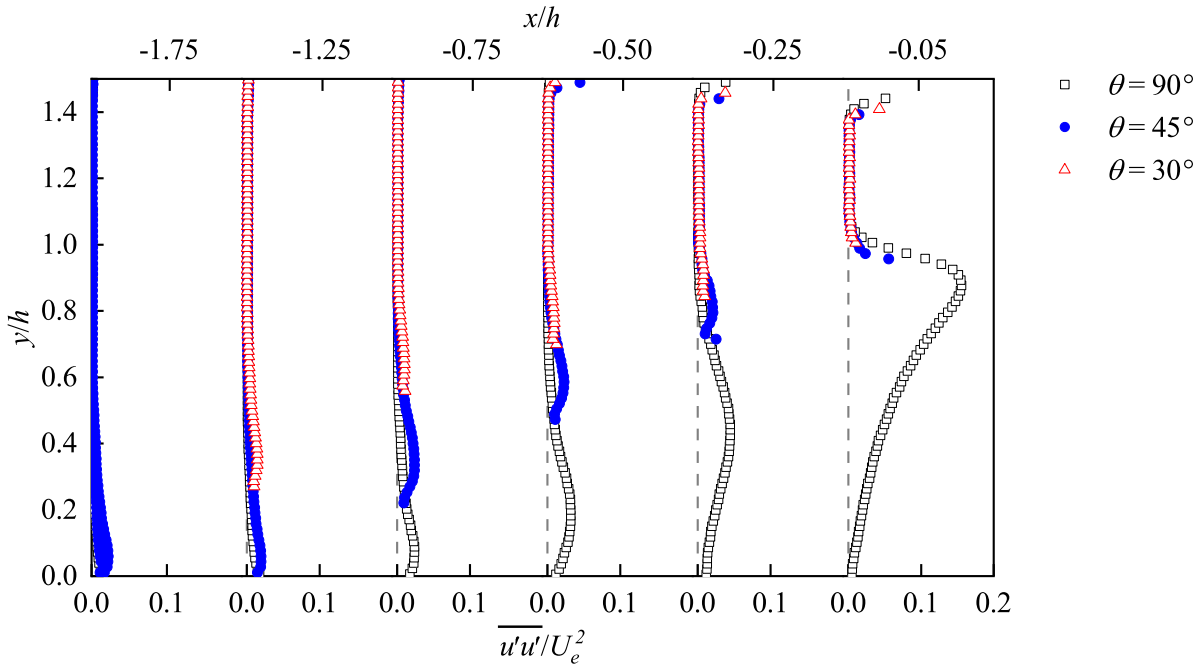

Figure A.9. Stream-wise evolution of the normalized stream-wise Reynolds normal stress profiles for different upstream face inclinations at $D_c/h = 0.4$.

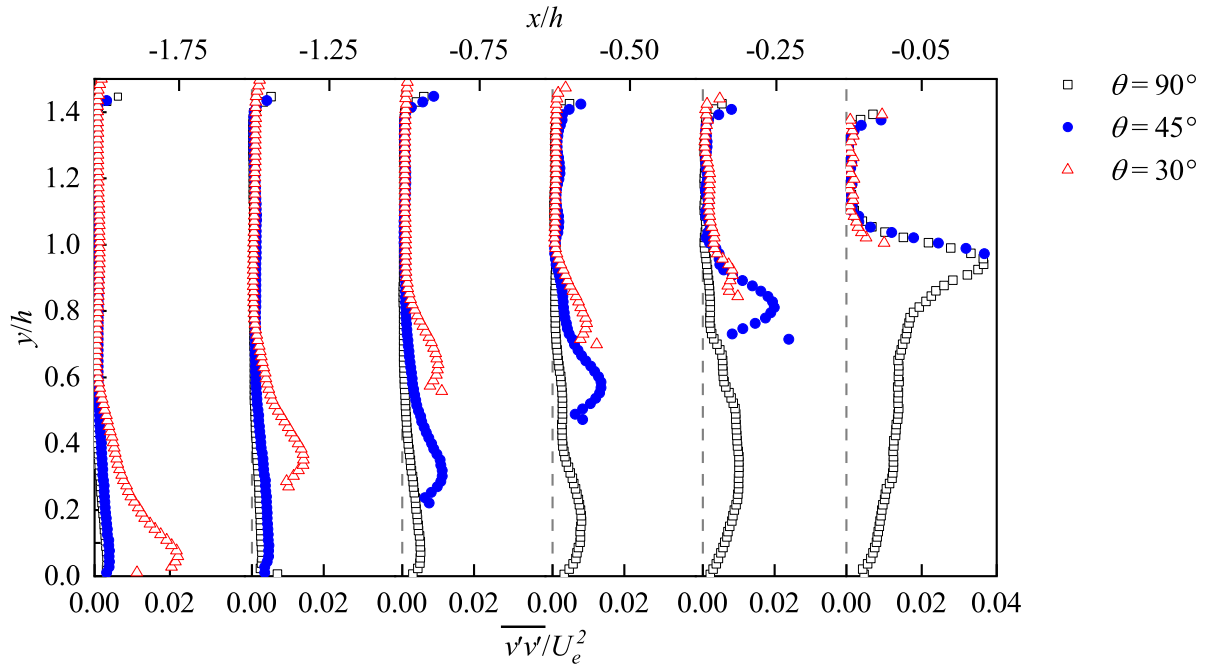

Figure A.10. Stream-wise evolution of the normalized vertical Reynolds normal stress profiles for different upstream face inclinations at $D_c/h = 0.4$.

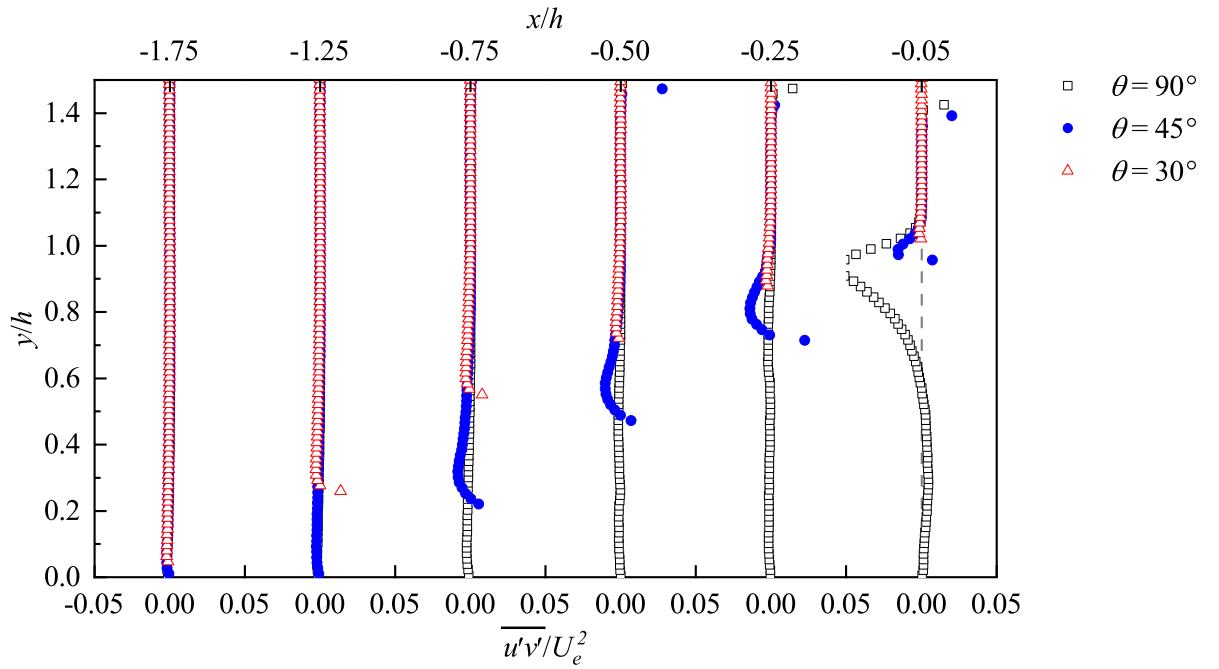

Figure A.11. Stream-wise evolution of the normalized Reynolds shear stress profiles for different upstream face inclinations at $D_c/h = 0.4$.

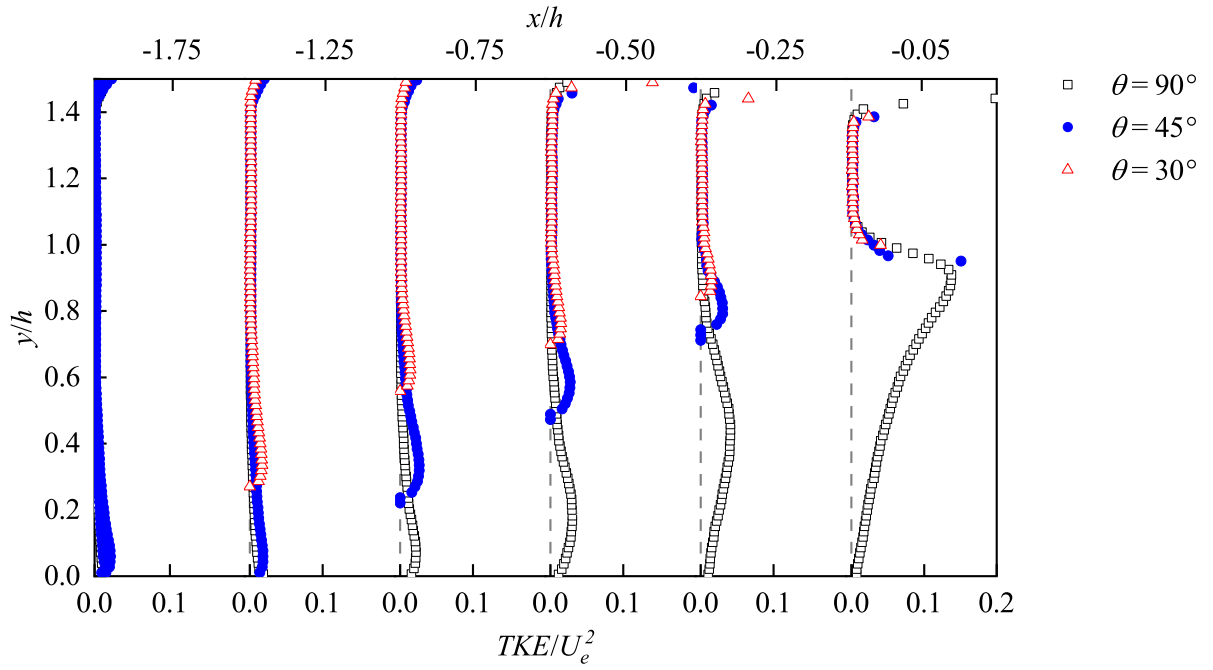

Figure A.12. Stream-wise evolution of the normalized TKE profiles for different upstream face inclinations at $D_c/h = 0.4$.

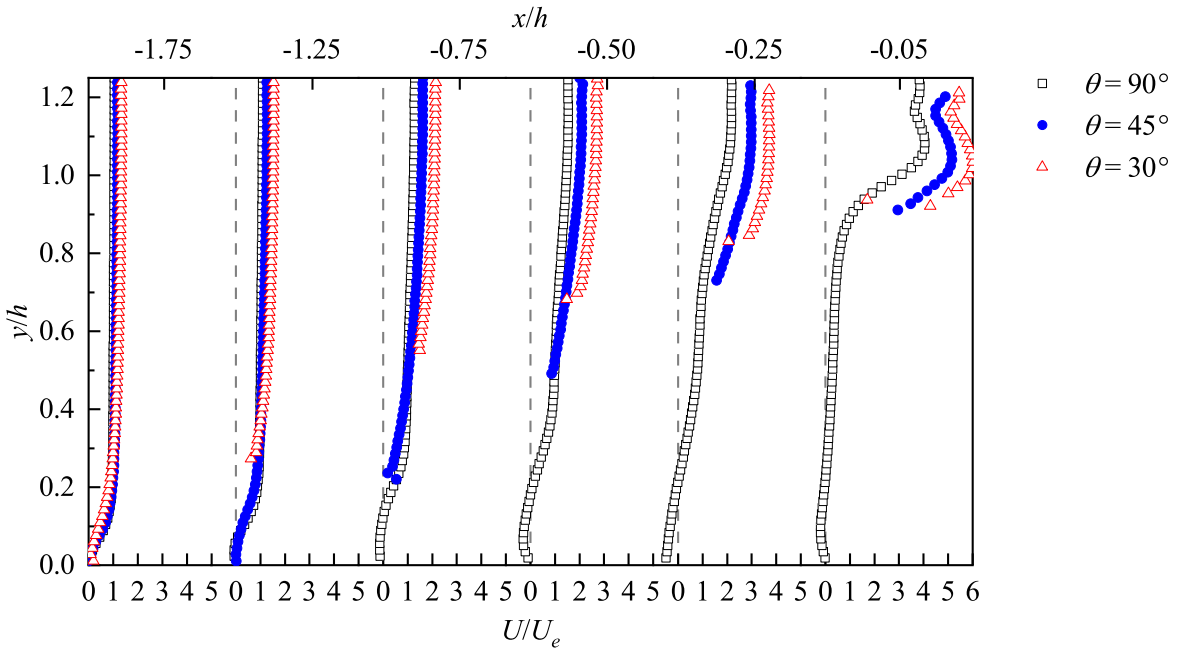

Figure A.13. Stream-wise evolution of the normalized mean stream-wise velocity profiles for different upstream face inclinations at $D_c/h = 0.2$.

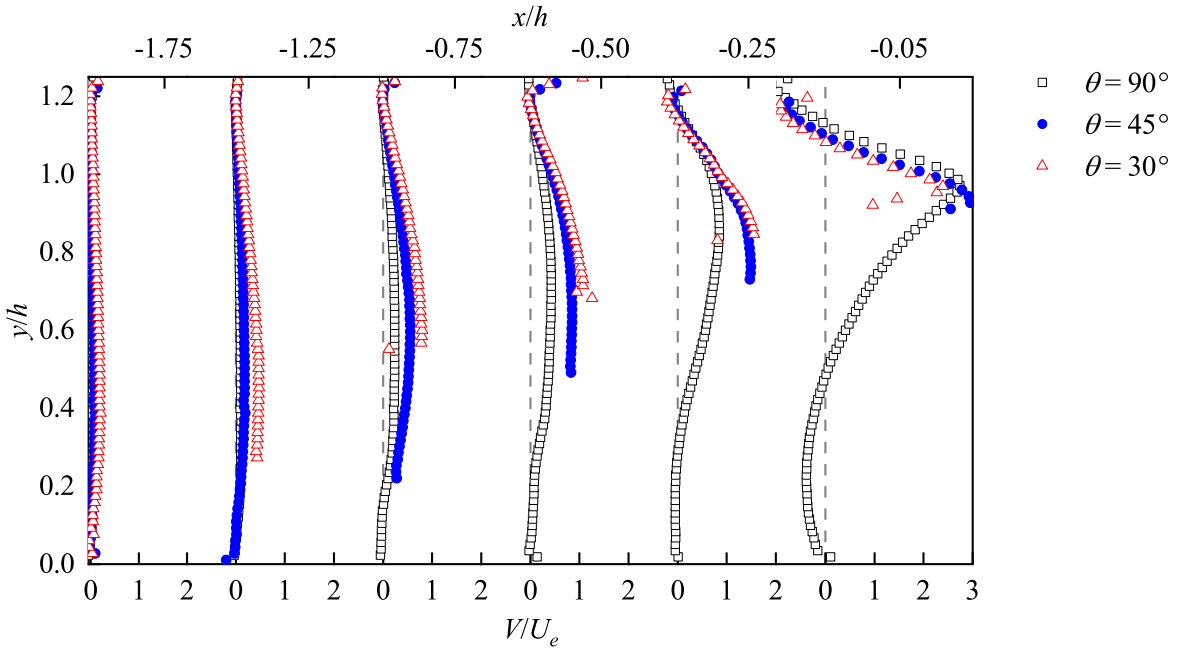

Figure A.14. Stream-wise evolution of the normalized mean vertical velocity profiles for different upstream face inclinations at $D_c/h = 0.2$.

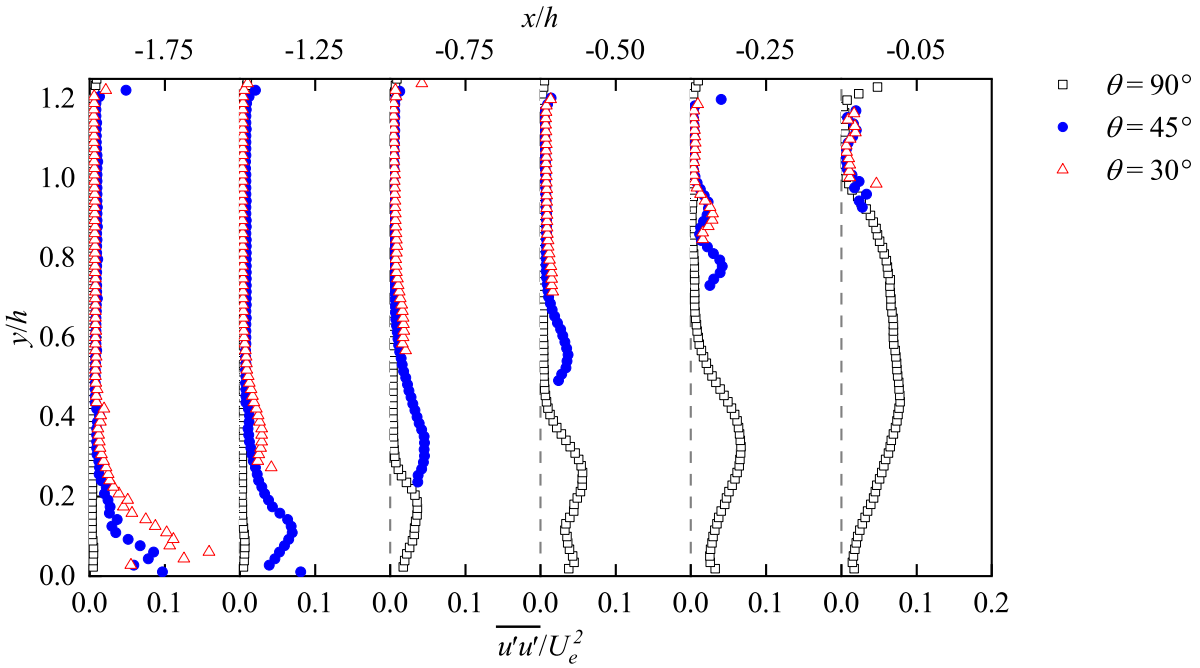

Figure A.15. Stream-wise evolution of the normalized stream-wise Reynolds normal stress profiles for different upstream face inclinations at $D_c/h = 0.2$.

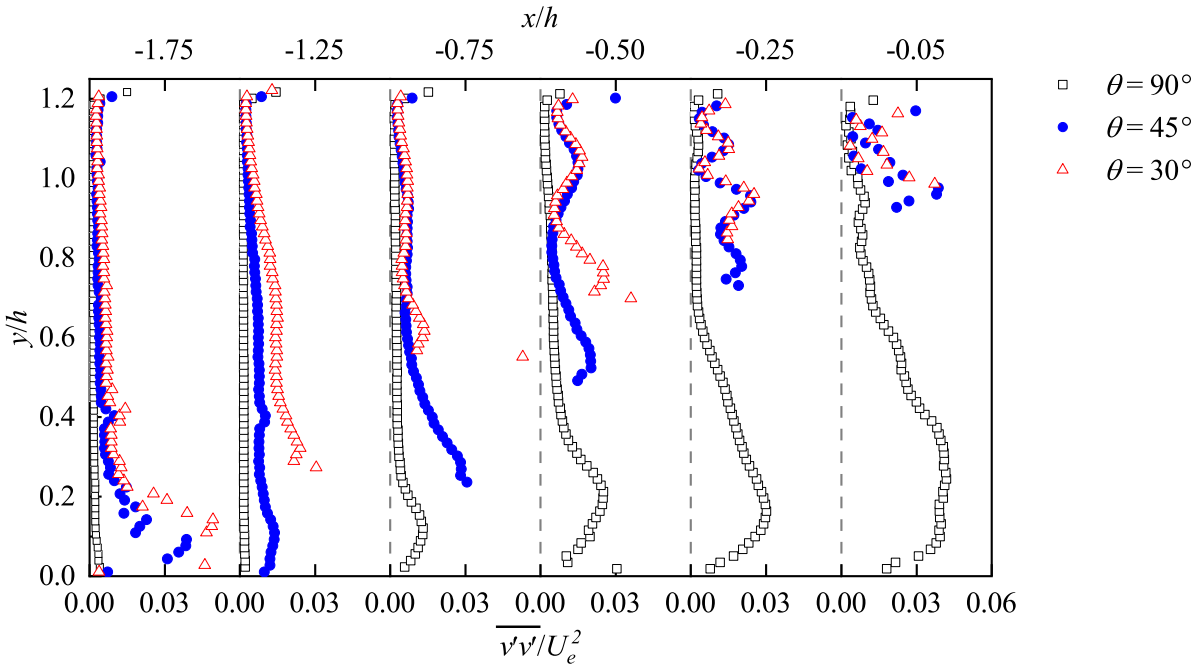

Figure A.16. Stream-wise evolution of the normalized vertical Reynolds normal stress profiles for different upstream face inclinations at $D_c/h = 0.2$.

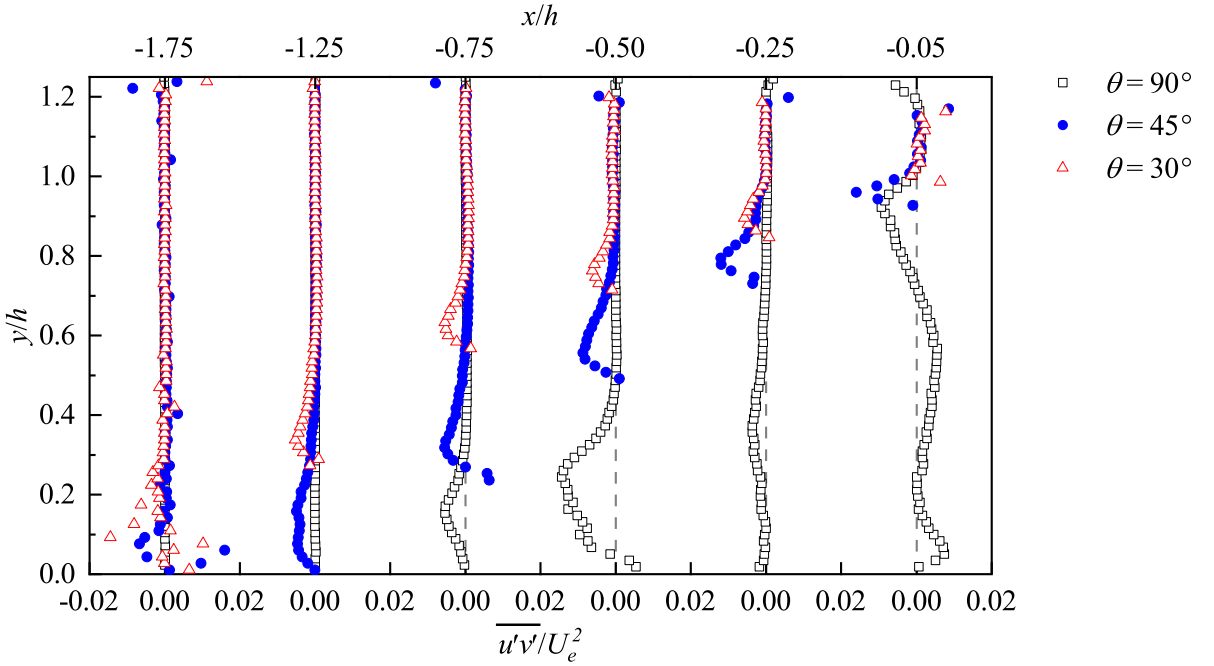

Figure A.17. Stream-wise evolution of the normalized Reynolds shear stress profiles for different upstream face inclinations at $D_c/h = 0.2$.

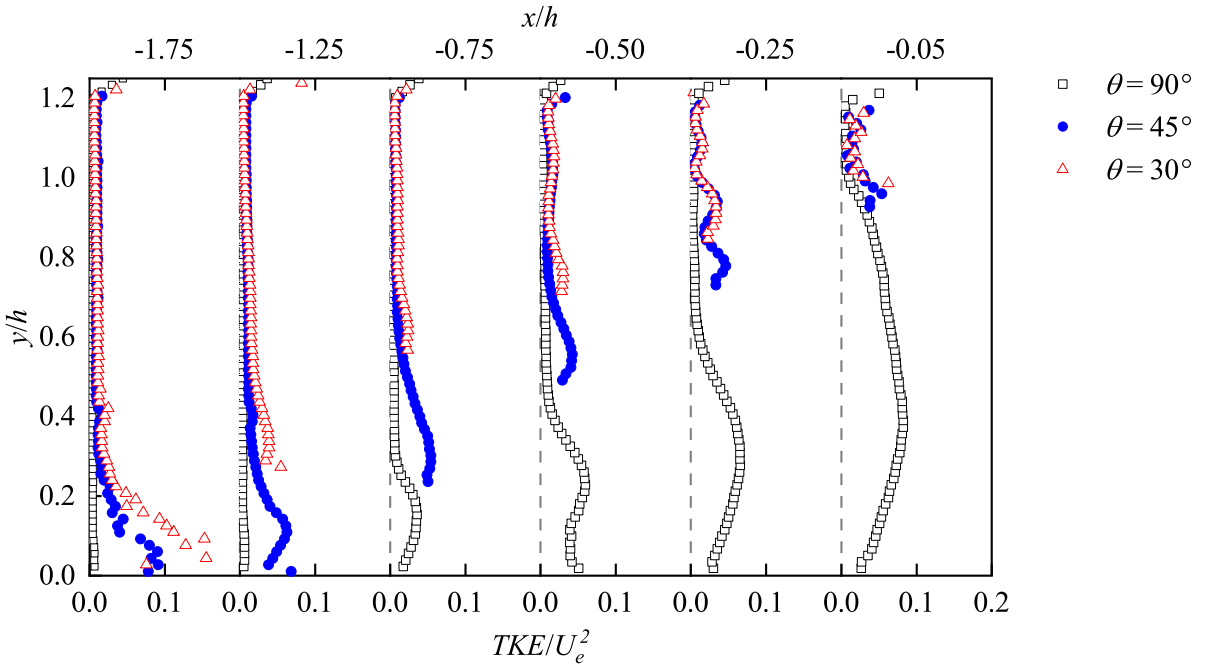

Figure A.18. Stream-wise evolution of the normalized TKE profiles for different upstream face inclinations at $D_c/h = 0.2$.